UNIVERSITÀ DEGLI STUDI DI PADOVA

Dipartimento di Fisica e Astronomia "Galileo Galilei"

Master Degree in Astrophysics and Cosmology

Final dissertation

Chemical abundances along the Main Sequence of Quasars

Thesis supervisor
Prof. Mauro D'Onofrio
Thesis co-supervisor
Dr. Paola Marziani

Candidate
Alberto Floris

Academic Year 2022/23

Abstract

This thesis aims to show a clear pattern of metal content in the central regions of Active Galactic Nuclei (AGNs) along the Quasar Main Sequence (MS). The Quasar MS, the well-established anti-correlation between the Full Width at Half Maximum (FWHM) of the Hβ emission line and the R_{FeII} quantity (the ratio between the intensity of the FeII line and the intensity of the Hβ emission), holds significant importance akin to the iconic Hertzsprung-Russell diagram in stellar studies. The identification of a metallicity trend holds pivotal implications for our comprehension of the inner workings of AGNs and ultimately of the galaxy formation process.

By meticulously analyzing the optical and UV spectra of 14 low-z AGNs, selected as representative specimens from various types along the Quasar MS, we derived diagnostic ratios from optical and UV emission feature in Quasar spectra obtained from ground- and space-based (HST FOS and COS) observations. These ratios were then compared with values obtained from `CLOUDY` photoionization simulations. Through this analysis, we aim to illustrate a method able to constrain the physical conditions within the Broad Line Region (BLR) of each active galaxy and to provide a robust estimation of the metallicity.

The metallicities derived from diagnostic ratios are solar or sub-solar for the Population B of Quasars, radiating at modest Eddtington ratio. In contrast, higher Eddington-ratio Population A sources display a noteworthy upward trajectory in metallicity. Within this class, metallicity values can surpass solar levels, even by a factor of 5 or more, in Super-Eddington candidates.

The initial and robust measurement of the metallicity trend along the Quasar MS substantially contributes to defining the characteristics of the nuclear environment, with implication on the star formation activity within it. It is a starting point to delineate the relevance of feedback effects for quasars in different accretion modes.

Contents

Chapter 1

Introduction

In this chapter, we present a comprehensive overview of the properties of Active Galactic Nuclei (AGNs) and introduce the Quasar Main Sequence (MS). Section 1.1 provides a brief historical account of AGNs and explores their fundamental properties. Section 1.2 describes the Unification model of AGNs. Section 1.3 delineates how the Eigenvector 1 parameter space defines the Quasar MS, together with the Quasar populations that characterize it. In Section 1.4 the Broad Line Region (BLR) of AGNs is described, explaining how the spectral lines employed in this study serve as valuable diagnostics of its properties. In Section 1.5 the scaling relations used to define the accretion parameters are defined. In Section 1.6 the accretion parameters are explored as additional tools to disentangle the intricate properties of AGNs. In Section 1.7 the motivations and the aims of this work are articulated.

1.1 Active Galactic Nuclei in the context of the general galaxy population

Galaxies are systems of stars, gas, dust and dark matter held together by gravity. The vast majority of galaxies, above a given mass, even the one in which we reside, the Milky Way, host a Supermassive Black Hole (SMBH) at their center (Kormendy & Richstone, 1995). SMBHs are compact objects that have an extremely large mass with respect to their spatial extension. The distinction between SMBHs and the stellar-mass nuclear aggregates lies primarily in their immense mass ($M > 10^6 M_\odot$) confined in a very small region.

The concept of black holes (BHs) as compact sources have been first predicted by the theory of general relativity. These objects have a gravitational potential so strong, and concentrated in a single point known as the "singularity", that even photons cannot escape. Their size is characterized by the so called *Schwarzschild radius*

$$R_s = \frac{2GM}{c^2}, \tag{1.1}$$

where G is Newton's gravitational constant, M is the mass of the black hole and c is the speed of light. SMBHs, situated at the center of galaxies, accrete matter from a

surrounding "accretion disk." This process results in the emission of an extraordinary amount of energy, often surpassing the combined luminosity of the entire galaxy (Rees, 1984). The high luminosity of these bright nuclei, exceeding that expected from stellar and associated processes, led to the classification of a broad category known as "Active Galactic Nuclei" (AGN).

Observational clues about AGNs date back to 1908, when Edward A. Fath detected prominent emission lines in what he described as a "spiral nebula", now identified as NGC 1068, at the Lick Observatory. In 1943, Carl K. Seyfert observed galaxies with high ionization potential emission lines (Seyfert, 1943), broadened with $\Delta v \approx 8500$ km s^{-1}. These galaxies, now known as "Seyfert Galaxies", a particular type of AGN, exhibited bright central regions resembling stellar nuclei in optical images.

Subsequently, the 3C (Edge et al., 1959) and 3CR (Bennett, 1962) catalogs were published and completed in the 1960s. In 1963 Maarten Schmidt was able to identify the 3C273 radio source with an optical counterpart, which exhibited strong and broadened emission lines at unusual wavelengths. Upon closer examination, the emission lines were identified as Balmer lines but with a redshift z=0.158, a value unheard of at the time (Schmidt, 1963). From that moment on it became clear that these celestial entities were not only highly luminous but also observable at great distances. Coined as quasi-stellar radio sources (QSOs) or simply Quasars, these sources became of extreme interest for astrophysics in the following decades.

In 1964, Edwin E. Salpeter and Yakov B. Zeldovich independently proposed that accretion onto SMBHs could explain the observed properties of Quasars (Salpeter, 1964). The existence of SMBHs was assumed primarily because they provided the most plausible explanation for the observed properties of most galaxies. Further evidence supporting the presence of SMBHs was obtained through techniques like reverberation mapping, revealing compact sources in the centers of most galaxies (Peterson & Wandel, 2000).

Definitive proof of SMBHs' existence came in 2019 with the release of the image of the SMBH at the center of M87, obtained by the Event Horizon Telescope (EHT) (Event Horizon Telescope Collaboration et al., 2019). Subsequently, the image of the Black Hole at the center of our galaxy, Sagittarius A* (Figure 1.1), was released in 2022 (Event Horizon Telescope Collaboration et al., 2022).

1.2 Unification model of AGNs

Presently, a wide array of sources, comprising Seyfert Galaxies, Blazars, Quasars, Radiogalaxies and their refined subcategories, collectively embody a diverse spectrum of AGN traits. Among them, some shine as the most radiant exemplars, while others manifest collimated jets of charged particles discernible at specific wavelengths. The unifying thread binding these sources is their powerful non-thermal emission originating from a compact central area within their host galaxy. One of the first classifications that can be applied in order to disentangle the differences of all AGNs, is the distinction among strong radio objects (Radio Loud - RL) and Radio Quiet (RQ) objects using the relationship:

$$\mathrm{R}_K = \frac{f_{\mathrm{Radio}}}{f_B} \tag{1.2}$$

first defined in Kellermann et al. (1989), where R_K is the radio-to-optical ratio of emission, f_{Radio} is the specific flux at a wavelength of $\lambda = 6$ cm (5 GHz) and f_B is the specific

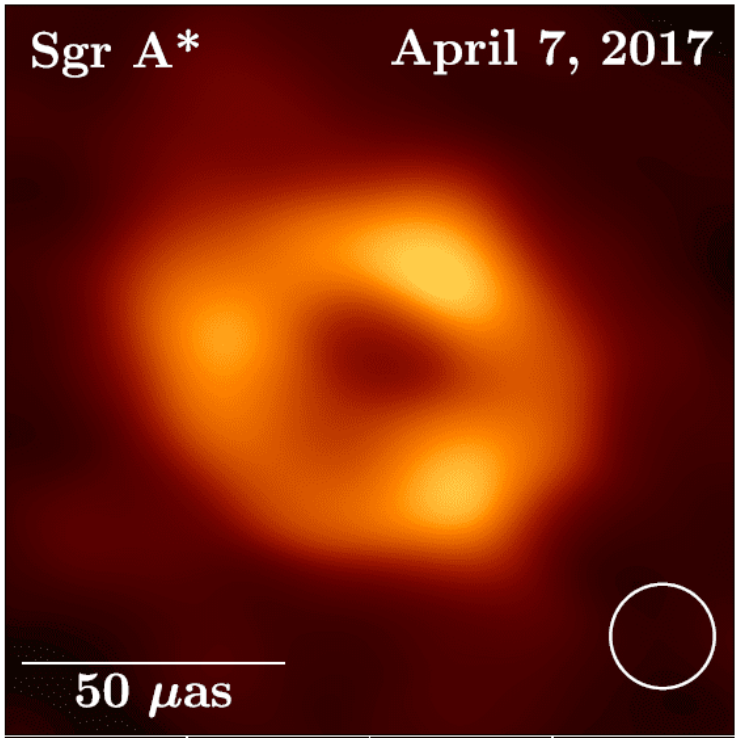

Figure 1.1: Representative image of Sagittarius A* obtained with the Event Horizon Telescope (EHT) from observations on 2017 April 7. Image taken from Event Horizon Telescope Collaboration et al. (2022).

flux at $\lambda = 4400$ Å (680 THz) in the B band. According to this relationship, a source is considered RQ when $R_K < 1$, and RL when $R_K > 10$. Objects with R_K between these two values are Radio Intermediate (RI), but for the purpose of this classification we will consider RQ and RL objects. It is crucial, for all intents and purposes, to underline the fact that RQ does not mean Radio Silent, an object that does not have a signature in the radio wavelength range. Indeed, the vast majority of RQ AGNs are able to exert some amount of radio signature. Among all AGNs, approximately 90% are RQ, while only about 10% are RL (Urry & Padovani, 1996).

With this initial subdivision in mind, the AGN unification model posits that the large diversity of AGN properties can be explained by a small number of physical parameters and elements. The unified AGN model comprises the following fundamental elements, as described in Netzer (2013):

1. **Supermassive Black Hole**: Positioned at the core of the galaxy, these black holes possess masses ranging from 10^6 - 10^{10} $M_\odot$. They represent the most compact objects that can exist for a given mass.

2. **Jets:** A pair of collimated plasma jets emerges from the galactic nucleus. In a typical scenario, these jets form two lobes of charged particles oriented perpendicular to the plane of the accretion disk and the torus. Their size can vary from a few kpc to Mpc.

3. **Accretion Disk**: This structure forms due to the gravitational potential of the black hole, causing gas to accumulate around it and settle into a rotating disk. Associated substructures, such as the corona, play a significant role in generating the hard X-ray continuum.

4. **Broad Line Region**: This region consists of dense (with densities approximately between 10^9 and 10^{13} particles per cubic centimeter), dust-free gas clouds located in close proximity to the black hole (0.01-1 pc). These clouds are partially ionized by emission from the accretion disk and orbit around it. The velocity of these clouds corresponds to the broadening observed in spectral lines originating in this region.

5. **Toroid**: An optically thick torus of gas and dust surrounds the accretion disk. It can have a smooth or clumpy structure and obscures the direct view of the AGN's central region. Its radius typically falls within the range of 0.1-10 pc.

6. **Narrow Line Region (NLR)**: This region comprises less dense clouds (with densities around 10^3 particles per cubic centimeter) that are farther from the black hole and extend approximately 100 pc. They exhibit a spherical or conical geometry above and below the torus. Most of the gas located in this region is also coupled with dust, in a region referred to as the "coronal line region".

7. **Maser disk**: A very thin disk, located where molecules can resist the strong ionization from the central region, from which molecular masers are emitted.

The simplest way to characterize the fact that radiation emanating from the central region of AGNs can suffer absorption, scattering and reflection on the way out depending on wavelength, is through the "unification by inclination" theory (Antonucci, 1993; Urry & Padovani, 1996). According to this theory, the differences among AGNs are predominantly governed by two parameters: the inclination of the torus relative to the line of sight (LOS) and the luminosity of the source.

The primary distinction arises from inclination, leading to the categorization of AGNs into Type-I and Type-II. This classification hinges on the object's inclination with respect to the LOS. The characteristics of each group are outlined below:

- **Type-I AGNs**: distinguished by the presence of broad ($\sim$ 1000 - 20000 km s^{-1}) permitted and semi-forbidden emission lines, along with strong high-ionization narrow emission lines, many of which are forbidden lines (Netzer, 2013). The existence of broad emission lines implies that our LOS is unobstructed, and we have a clear view of the central region, including the accretion disk. This will be further discussed in Section 1.4.

- **Type-II AGNs**: characterized by narrow ($\sim$ 300 - 1000 km s^{-1}) emission lines, the strongest of which are typically the Hydrogen lines of the Balmer and Lyman series and [OIII]λ5007 (Netzer, 2013). Unlike Type-I AGNs, Type-II AGNs lack broad emission lines. This suggests that our LOS is obstructed by the dusty torus, allowing us to observe only narrow and scattered emission lines.

Building upon these considerations, the main classes of AGNs are described below, following the example in Figure 1.2, which separates objects between RQ and RL. Beginning with RQ objects:

- **Seyfert Galaxies**: named after Carl Seyfert, who first studied them in 1943, noting the distinctive characteristics that set them apart from other galaxies. In optical

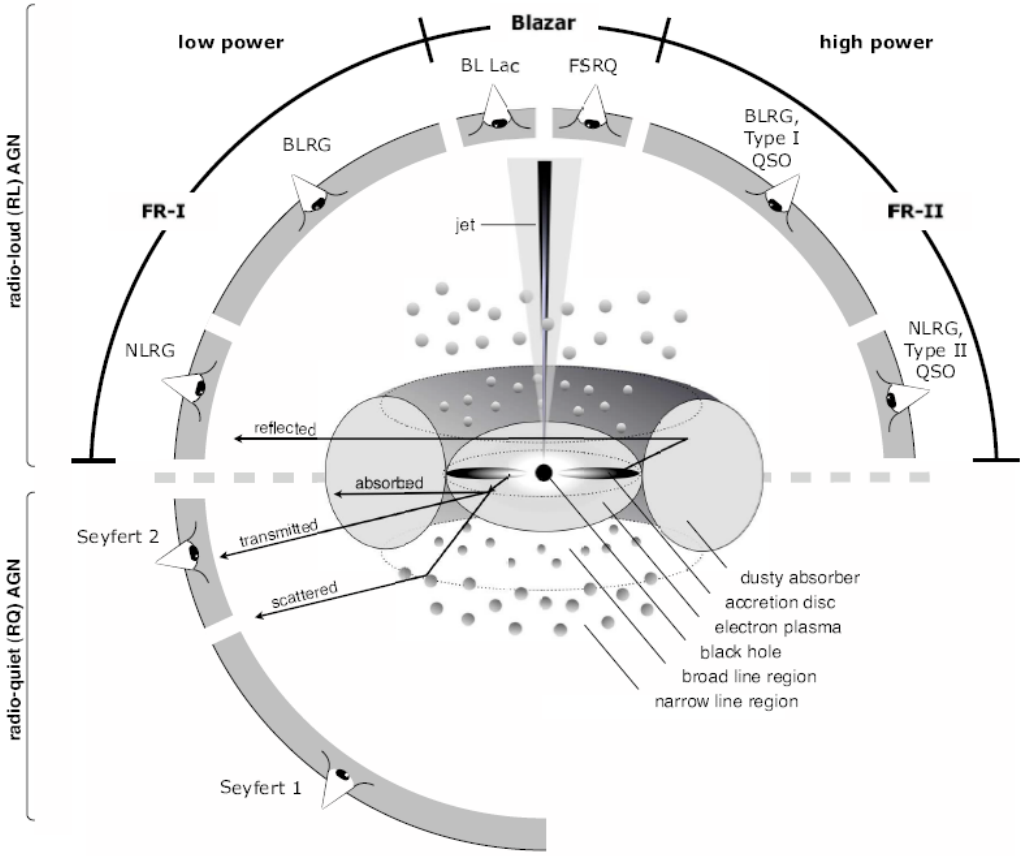

Figure 1.2: Schematic representation of AGNs in the unified model. This image describes how the type of object observed depends on the viewing angle and the luminosity of the source. Above are described RL AGNs, while at the bottom are RQ AGNs. Figure from Beckmann & Shrader (2012).

observations they are typically identified as galaxies with a bright, point-like nucleus with a spectrum characterized by prominent emission lines. Based on the presence of broad or only narrow emission lines, they are further categorized into Type-I and Type-II.

- **LINERs**: characterized by low ionization, narrow emission lines in their spectra. Typical strong emission lines are [NII]λ6584 and [SII]λ6731 and lines of the Balmer series (Netzer, 2013). LINERs are typically associated with lower levels of AGN activity and luminosity with respect to Quasars and Seyfert Galaxies.

- **Lineless AGNs**: characterized by non-existent or completely undetected emission lines. They are, however, recognized as AGNs by the presence of a central non-stellar source, and the variability of continuum emission. This variability, however, is not discernible in the optical wavelength range, but thanks to X-Ray or radio observations.

Concerning RL objects, the following subclasses are observed:

- **Radiogalaxies**: typically elliptical galaxies that host an active nucleus. Their main characteristic is a strong radio emission, accompanied by a relativistic jet. Depending on their spectral characteristics they can be divided into:
  - **Broad Line Radio Galaxies (BLRGs)** when they show broad lines;
  - **Narrow Line Radio Galaxies (NLRGs)** when they only show narrow lines.

  Fanaroff & Riley (1974) also proposed another classification depending on the radio morphology and luminosity:
  - **Fanaroff-Riley I (FR I)**: sources characterized by a concentration of luminosity near the nucleus, having a luminosity $L(178\text{MHz})$ measured at 178 MHz smaller than the one given by the following expression:

    $$L(178\text{MHz}) \lesssim 2 \times 10^{25}\ H_{100}^{-2}\ \text{W Hz}^{-1}\ \text{str}^{-1}, \tag{1.3}$$

    where H_{100} is the Hubble constant divided by a factor 100 (Kembhavi & Narlikar, 1999).
  - **Fanaroff-Riley II (FR II)**: sources characterized by a concentration of luminosity in the lobes of charged particles, decreasing towards the nucleus. They are typically more luminous, with a $L(178\text{MHz})$ greater than the one in equation 1.3.
- **Quasars**: sources that are typically point-like, as they cannot be optically resolved. They appear to have the highest luminosities among AGNs, as they can be detected up to extremely high redshift.
- **Blazars**: characterized by strong polarization of their emission and high variability, emitting across the entire electromagnetic spectrum. They also exhibit strong relativistic jets, directed along the observer's LOS. Depending on their spectroscopic properties they can be classified into:
  - **Flat Spectrum Radio Quasars (FSRQ)** showing strong broad and narrow emission lines;
  - **BL Lacertae Objects** characterized by high variability on timescales from minutes to years. They show a strongly polarized power law continuum without the presence of emission lines.

1.3 The Eigenvector 1 parameter space

Trying to disentangle the nature of the BLR and NLR in Quasars, Boroson & Green carried out a Principal Component Analysis (PCA) on numerous optical spectra of Quasars, predominantly within the optical wavelength range (Boroson & Green, 1992). Among the sets of parameters identified in the paper, the one that showed the most robust connection was the Eigenvector-1 parameter space (E1). The E1 describes the anti-correlation of the Full Width at Half Maximum (FWHM) of the Hβ emission with the quantity R_{FeII}:

$$\text{R}_{\text{FeII}} = \frac{I(\text{FeII}\lambda 4570)}{I(\text{H}\beta)}, \tag{1.4}$$

where $I(\mathrm{FeII}\lambda4570)$ is the intensity of the FeII (evaluated in the λ4434-λ4684 Å range) and $I(\mathrm{H}\beta)$ is the intensity of the Hβ emission. This correlation between parameters is very robust, meaning that it keeps coming out in both small and large samples of Quasars, and was thus used to define the "Main Sequence (MS) of Quasars" (Marziani et al., 2018). Its distinctive shape is depicted in Figure 1.3.

At first sight the connection between the parameters $\mathrm{R_{FeII}}$ and FWHM(Hβ) seems obscure. Indeed, FeII emission relative to Hβ can vary from undetectability to the rarest values of $\mathrm{R_{FeII}} \gtrsim 2$(Marziani et al., 2022). FeII emission extends from the UV to the infrared and can dominate the thermal balance of the BLR for low-ioniazition interactions (Marinello et al., 2016). The FWHM of Hβ is related to the velocity field in the virialized low-ionization region of the BLR, and to viewing angle effects. These two parameters therefore reflect the physical conditions in these regions, along with the orientation.

The analogy with the MS of stars is clear: both main sequences allow for the definition of spectral types. As a matter of fact, it has been shown that, with few exceptions, every Quasar occupies a well defined position in the E1 parameter space. Consequently, each quasar can be described as part of one of three larger populations: Population A, Population B and extreme Population A (xA) Quasars.

We will now describe the various populations in the following sections. These populations exhibit different properties, and as shown in Figure 1.3 Population A has a FWHM(Hβ)$\leq$ 4000 km s^{-1}, while Population B has a FWHM(Hβ)$>$ 4000 km s^{-1}. The distinction, although it sounds arbitrary and sudden, comes from the different structures of the BLR in these two populations. As a matter of fact, the BLR in Population A Quasars is described by a slim geometrically thick advection-dominated accretion disk, while Population B Quasars have a flat, geometrically thin, accretion disk (Marziani et al., 2018).

1.3.1 Population A Quasars

Population A Quasars, as we said in the previous sections, are relegated to the lower part of the MS, since they exhibit a FWHM(Hβ)$<$ 4000 km s^{-1}. This, however, is not the only distinctive property of this population. As a matter of fact, in the context of the 4D Eigenvector 1 (4DE1) optical plane, Population A Quasars are characterized by a wide range of values for the $\mathrm{R_{FeII}}$, allowing for the definition of four spectral types: from left to right in Figure 1.3 A1, A2, A3 and A4, with higher $\mathrm{R_{FeII}}$ the more we move towards the lower-right corner of the MS, encountering xA Quasars (discussed in Section 1.3.2). Population A Quasars are also rarely strong radio emitters with respect to Population B Quasars(Zamfir et al., 2008; Shen & Ho, 2014).

In their spectrum, Population A Quasars exhibit lorentzian profiles for the Broad Component (BC) of major low-ionization lines (LILs, in particular Hβ) and high-ionization lines (HILs, such as CIVλ1549). They also typically exhibit asymmetries in their line profiles favouring the blueshifted -outflow- component (BLUE), that are usually strong in HILs (Marziani et al., 2010).

1.3.2 xA Quasars

Extreme-accreting Quasars (xA) owe their name to the fact that they accrete matter at high rates, emitting the largest amount of radiation per unit of mass among all

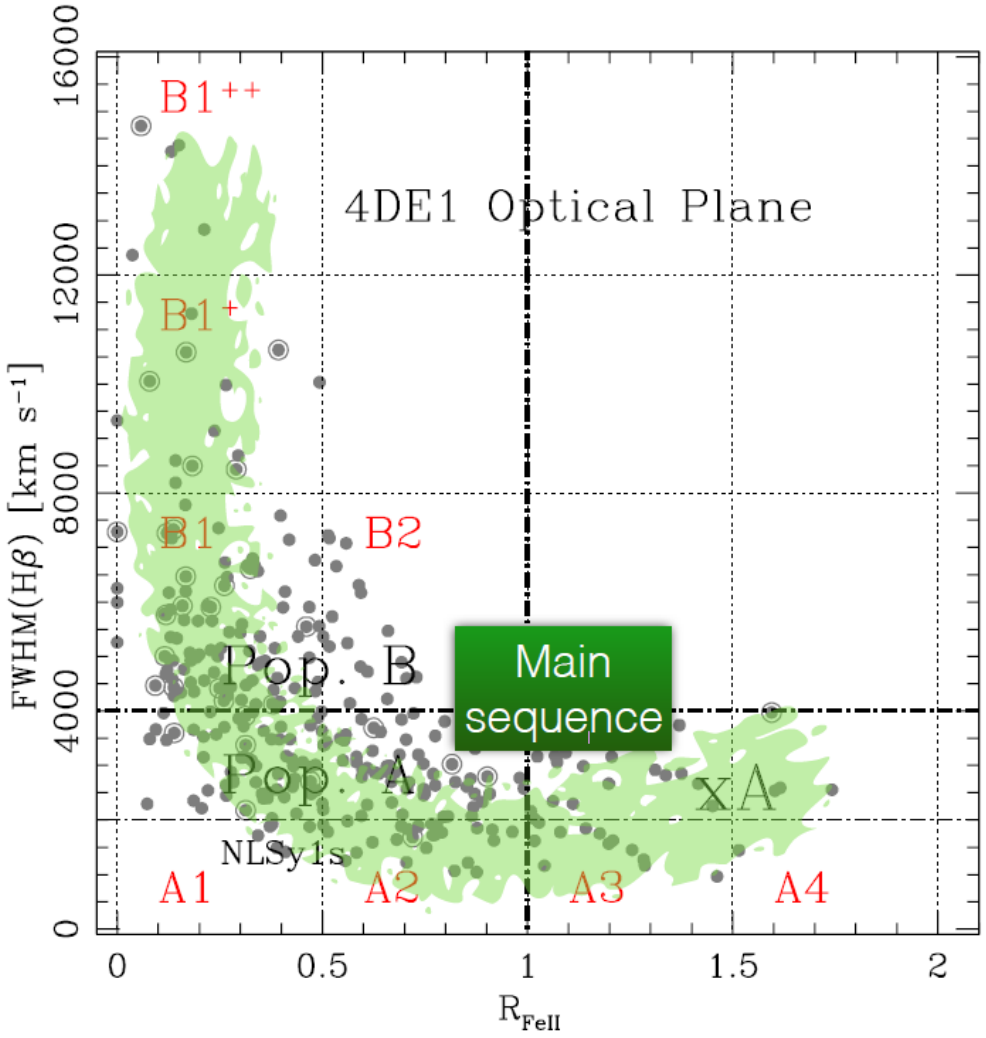

Figure 1.3: The 4DE1 optical plane, mainly FWHM(Hβ)vs. R_{FeII}. The green shaded area traces the distribution of a quasar sample from Zamfir et al. (2010), defining the Quasar MS. The thick horizontal dot-dashed line separates populations A and B; the thin identifies the limit of Narrow Line Seyfert 1 galaxies (NLSy1s). The vertical dot-dashed line marks the limit for extreme Population A (xA) sources. Figure from Marziani et al. (2018).

Quasars. Extreme Super-Eddington rates of emission are measured by the Eddington Ratio $L_{\rm bol}/L_{\rm Edd}$ (further discussed in Section 1.5).

They are found in the lower-right part of the MS. As we described before, they are a subclass of Population A Quasars with spectral types A3 and A4, exhibiting a FWHM(Hβ)$<$ 4000 km s^{-1} and $R_{FeII} > 1$. They share most properties of Population A Quasars, but are typically characterized by higher metallicities (Nagao et al., 2006; Śniegowska et al., 2021), and they are systematically found at higher redshift ($z \gtrsim 5$) (Bañados et al.,

2016), suggesting the possibility of being newborn objects with a population peak when the Universe was younger (Sulentic et al., 2000; Diamond-Stanic et al., 2009; Plotkin et al., 2015).

Qualitatively speaking, xA Quasars show very prominent AlIII lines and weak or absent CIII] lines. As we said before, FeII emission is the strongest among all Quasars of the MS. The BC of lines is modelled consistently with Population A Quasars with lorentzian profiles. However, there is evidence of systematic blueshifts in both LILs and HILs, more remarkably in the latter, suggesting different physical conditions in the regions responsible for the emission of the BC and BLUE (Marziani et al., 2022). Blueshifts typically become more pronounced the more on the right of the MS the object is.

1.3.3 Population B Quasars

Population B Quasars are relegated to the upper-left part of the MS, since they exhibit a FWHM(Hβ)$>$ 4000 km s^{-1} and $R_{FeII} < 1$. In the context of the 4DE1 optical plane, Population B Quasars are divided in several spectral types with increasing FWHM(Hβ) by a step of 4000 km s^{-1}, defining B1 (4000 $<$ FWHM(Hβ) $<$ 8000 km s^{-1}), B1^{+} (8000 $<$ FWHM(Hβ) $<$ 12000 km s^{-1}) and B1^{++} (12000 $<$ FWHM(Hβ) $<$ 16000 km s^{-1}). Spectral type B2 Quasars are found to have similar FWHM(Hβ) of B1 Quasars, but $0.5 < R_{FeII} < 1$. Among Population B Quasars a remarkable number is RL (Shen & Ho, 2014). Nevertheless, Population B Quasars show defining spectral characteristics that distinguish them from Population A Quasars. Firstly, the BC of lines is modelled with gaussian profiles. Secondly, Population B sources show a distinctive feature: a Very Broad Component (VBC) in the profile of their LILs that has a much larger FWHM and is significantly redshifted with respect to the rest-frame of the Quasar (Marziani et al., 2010).

1.3.4 Physical interpretation of the Eigenvector 1

In Marziani et al. (2001), the correlation of the parameters FWHM(Hβ) and R_{FeII} with key physical parameters defining the properties of the BLR in these objects was established. These parameters include:

1. **Inclination along the LOS**: evident from distinct line profiles, particularly in CIV and Hβ. Notably, when CIV is blueshifted more than Hβ, it signifies a high-ionization wind emitting CIV and an optically thick disk emitting Hβ. The altered profile indicates a change in the covering of the BC-emitting region of CIV, providing evidence for a different orientation of the two regions relative to the LOS.

2. **Eddington ratio** $L/L_{\rm Edd}$: this parameter influences the physical conditions of the BLR due to its strong correlation with the presence of a soft X-Ray excess and an inverse correlation with the ionization degree.

Furthermore, photoionization simulations using `CLOUDY`, as presented in Panda et al. (2019), reaffirm the correlation of an object's position in the FWHM(Hβ)-R_{FeII} as a function of inclination, with extreme conditions which could be observed only in case of almost face-on objects. The simulations, depicted in Figure 1.4, underscore the substantial impact of inclination on the measured properties positioning an object on the MS of Quasars.

It is important to note that physical parameters such as density, metallicity, and Eddington ratio effectively explain the distinction between Population B and Population A Quasars, as well as extreme accretors. Spectral types B and A1 are associated with relatively low density, metallicity, and Eddington ratio. At moderate R_{FeII} values, physical conditions align with moderate density ($n_H \sim 10^{11}$ cm^{-3}, Martínez-Aldama et al.,2015), intermediate Eddington ratio, and typical Quasar metallicity. In contrast, extreme accretors exhibit exceptional conditions, including high density, super-Eddington accretion values, and elevated metallicity.

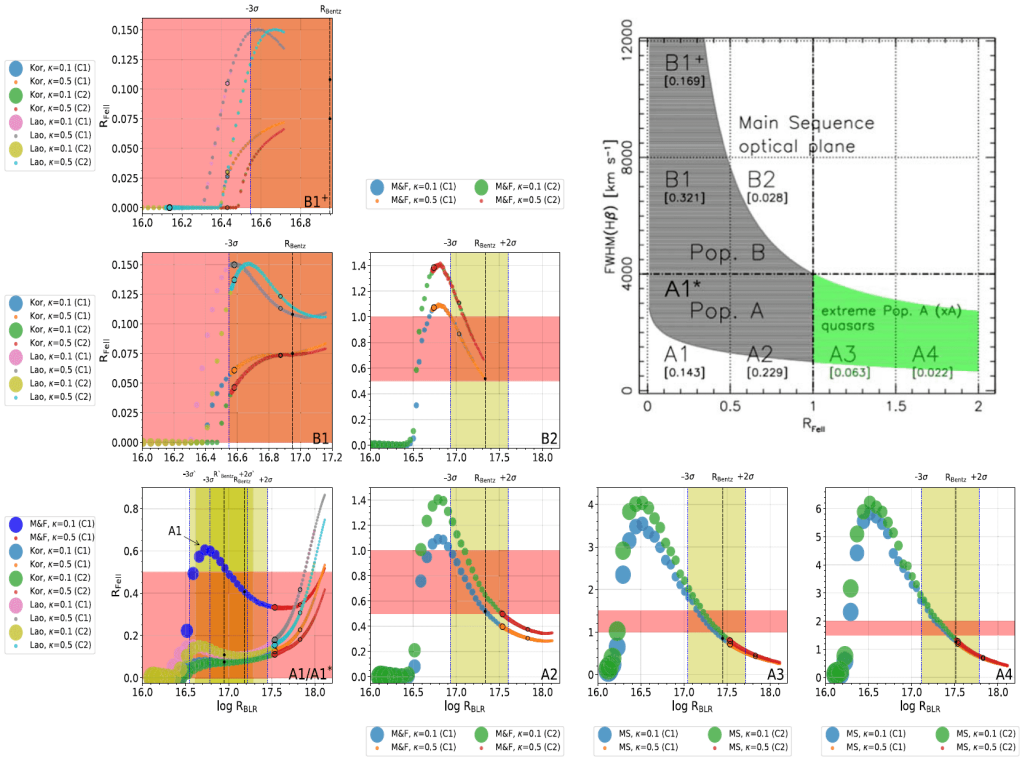

Figure 1.4: Sketch depicting the results of CLOUDY simulations performed for a constant-density single BLR cloud assuming $M_{BH} = 10^8\ M_\odot$. Simulations were performed for different physical conditions and using different SEDs adapted to the conditions found in each spectral type of the Quasar MS. The $\log R_{BLR}$ vs. R_{FeII} distribution is shown as a function of increasing viewing angle from 0° to 60°, with a greater angle the bigger the size of the marker. Open circles mark the values expected for $\theta = 30°$ and $\theta = 45°$. Red patches restrict the R_{FeII} values associated to the designed spectral type. Figure obtained from Panda et al. (2019), where the physical conditions associated to the simulations are also reported.

1.4 Physics and dynamics of the Broad Line Region

As discussed in Section 1.2, Type-I AGNs typically exhibit broad emission lines originating from a region with distinctive physical and dynamical properties, called the BLR. The intensity ratios of the broad emission lines serve as powerful tools for probing the physical

conditions within the BLR itself. The characteristics of the BLR, as outlined in Hamann & Ferland (1999), are as follows:

1. **Photoionization**: The BLR is photoionized. This is deduced from the response in the emission line intensities following variations in the continuum. Lag-times associated with these changes correspond to characteristic radii of the BLR (Peterson, 1993). Understanding the nature of the object is closely tied to the shape of the ionizing continuum.
2. **Spatial extent**: The BLR encompasses a range of distances from the black hole. Reverberation studies (discussed in Section 1.4.2) reveal different lag-times for different ions, with highly ionized species found closer to the central source.
3. **Density and ionization states**: The BLR exhibits a wide range of densities and ionization states, gradually changing inside-out.
4. **Column densities**: The BLR is characterized by large column densities, typically $N_{\rm H} \gtrsim 10^{23}$ cm^{-2}. However, the geometry of the emitting region is not yet well understood. Lines are known to form in different regions, and the various layers composing the BLR are believed to be inhomogeneous.
5. **Velocity of the gas**: Thermal velocities within clouds are believed to dominate the local line broadening and radiative transfer. The observed line widths in the spectra of AGNs are assumed to result entirely from the bulk motions of the gas. While micro-turbulence from local gas motion may play a role in the width of the lines in specific situations, it is generally not the case. However, it is important to note that it can facilitate resonance phenomena for line emission, especially in the case of FeII (Sarkar et al., 2021).

There is still much that is unknown about the line-forming regions in Quasars. The geometry and the spatial variations of physical parameters remain highly uncertain. Therefore, the typical strategy for studying the abundances of elements in the BLRs is to identify diagnostic line ratios with strong abundance sensitivities. For example, by comparing the line intensity of two atomic species that form in the same region, we can eliminate geometric effects from the computation of the abundance of each species. In the following discussion, we will explore how the typical lines found in the spectra of AGNs form, distinguishing between collisionally-excited lines and recombination lines (Hamann & Ferland, 1999).

Collisionally-excited lines form by the internal excitation of an ion following electron impact. Their emissivities, representing the energy released per unit volume and time, result from the statistical equilibrium of the energy levels, as described by the detailed balance equation from Hamann & Ferland (1999).

The line emissivity is calculated for two distinct cases (high and low density), with the threshold between them being defined by the critical density $n_{\rm crit}$:

$$n_{\rm crit} = \frac{\beta A_{\rm ul}}{q_{\rm ul}} \approx \frac{A_{\rm ul}}{\tau q_{\rm ul}}, \tag{1.5}$$

where $A_{\rm ul}$ is the spontaneous decay rate, β is the probability for line photons to escape the local region, $q_{\rm ul}$ is the downward collisional rate coefficient, and τ is the line-center optical depth. Specifically, $\tau \sim 1/\beta$ when $\tau \gg 1$. The critical density identifies the density where the upper level is equally likely to be de-excited by collisions as by radiative decays.

Typically, in the physical conditions that occur in the BLR, the gas is optically thin ($\tau < 1$) and the density is lower than the critical density, thus the collisional emissivity of the line ($\epsilon_{\rm coll}$) is described by the following equation:

$$\epsilon_{\rm coll} = n_{\rm l} n_{\rm e} q_{\rm lu} h\nu_0 \propto n_{\rm l} n_{\rm e} {\rm T}^{-1/2} \exp\left(-\frac{h\nu_0}{k{\rm T}}\right) \ [{\rm erg\ cm^{-3}\ s^{-1}}], \tag{1.6}$$

where $n_{\rm e}$ is the electron density and $q_{\rm lu}$ is the upward collisional rate coefficient.

The vast majority of lines that compose the UV spectrum, such as CIV, SiIV, OIV], CIII] and SiIII], are produced by collisional excitation.

Recombination lines, on the other hand, form by the capture of free electrons into excited states, followed by radiative decays to lower states. In the case in which every photon escapes freely and competing processes are unimportant, the emissivity is described by the equation:

$$\epsilon_{\rm rec} = n_{\rm i} n_{\rm e} \alpha_{\rm rad} h\nu_0 \propto n_{\rm i} n_{\rm e} {\rm T}^{-1}, \tag{1.7}$$

where $\alpha_{\rm rad}$ is the radiative recombination coefficient into the upper energy state, and $n_{\rm i}$ is the number density of parent ions (Osterbrock, 1989).

In the context of the BLR, the only lines produced by pure recombination are the HeII lines found at λ1640 Å and λ4686 Å.

1.4.1 Spectral Energy Distribution

Among all astrophysical objects, AGNs stand out due to their emissions spanning the widest range of energies, setting them apart from quiescent and star-forming galaxies.

Each component of an AGN is responsible for the emission within specific energy ranges:

1. **Synchrotron emission from the jet**: primarily responsible for the radio emissions of Quasars.
2. **Hot corona emission**: responsible for X-Ray and Gamma-ray emissions.
3. **Thermal emission from the accretion disk**: dominates the optical-UV range of energies.
4. **Dusty torus emission**: responsible for emissions in the submillimeter-infrared range.

In some cases, also a stellar contribution from the galactic disk might be noticeable.

The relative contributions of these components determine the classification of AGNs. For instance, RL objects are characterized by strong synchrotron and thermal emission, while RQ objects are characterized by weaker synchrotron and thermal emission, and they may also exhibit a significant stellar component.

The nature of each AGN is not only distinguished by the contribution of each component, but evidence suggests that it is also influenced by the accretion rate, displaying significant features associated with diverse processes (Panda & Marziani, 2023).

Various notable components of the Spectral Energy Distribution (SED) arise due to different radiation mechanisms and at varying distances:

1. **"Big Blue Bump"**: formed by optical and ultraviolet radiation produced via thermal emission from the accretion disk (Czerny & Elvis, 1987).
2. **Hard X-Ray emission**: well-fit by a power-law, and it is produced when UV photons from the disk undergo inverse Compton scattering by hot electrons in the hot corona close to the SMBH (Zdziarski et al., 1990).
3. **Soft-X excess**: characterized by emission from a Compton-thick corona connected to the innermost parts of the accretion disk (Petrucci et al., 2020).

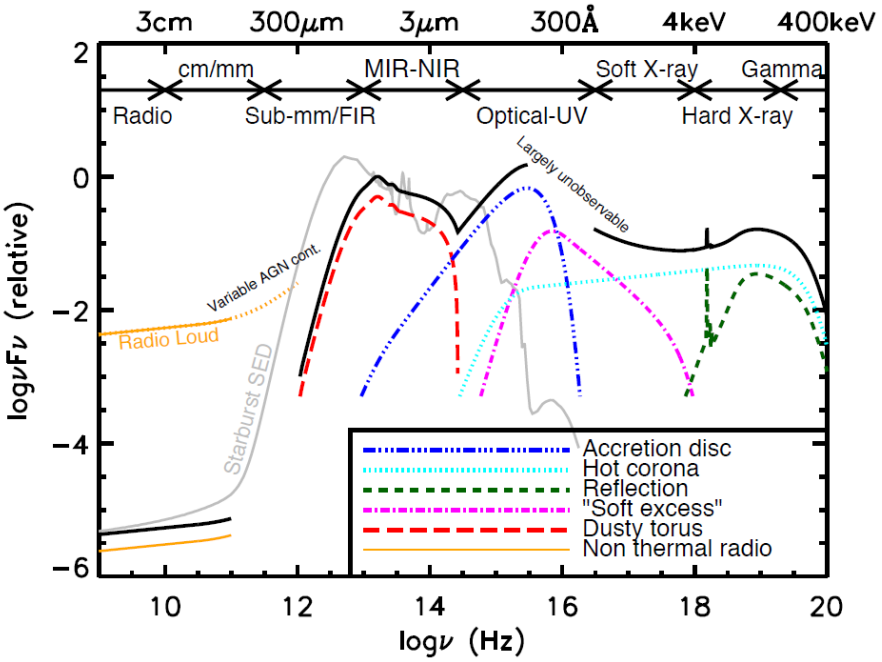

Figure 1.5: A schematic representation of an AGN SED, based on the observed SEDs of RQ Quasars. The black solid line represents the total SED, and the various coloured curves (with an arbitrary offset) represent the individual components described in the legend. Figure from Harrison (2014).

1.4.2 Reverberation mapping

Reverberation Mapping (RM) is a crucial tool for understanding the nature and structure of AGNs. It involves measuring the radius $r_{\rm BLR}$ of the BLR through the intrinsic variability of these objects. The variation in the intensity of UV and optical emission lines is observed in response to continuum changes. The emissivity-weighted distance of the BLR from the continuum source is provided by $\mathrm{r_{BLR}} = c\tau$, where c is the speed of light and τ is the time interval between two consecutive peaks of variations in the continuum and the lines.

To derive the mass of the SMBH, RM relies on several assumptions:

- The continuum emitting region is smaller than the line emitting region;
- Observable and ionizing continuum must be related;

- Light travel time must be longer than the recombination time and shorter than the dynamical timescale to ensure that the light travel time is dependent only on geometry;
- The line response must be linearly dependent on time;
- No dynamical effects of radiation.

However, several technical challenges also arise in RM:

- Data are typically unevenly sampled;
- Spectra taken involve different setups and conditions, leading to challenging normalization;
- The presence of a stellar contribution to the continuum of the object makes it difficult to isolate continuum variation (Bentz et al., 2009);
- Stratification of ionization might yield inconclusive results due the disjoint nature of the different components of an AGN.

In conclusion, the mass of the SMBH ($M_{\rm BH}$) can be estimated using the formula:

$$M_{\rm BH} = f\frac{r_{\rm BLR}\sigma_v^2}{G}, \tag{1.8}$$

where σ_v is the FWHM of the line considered for reverberation mapping (typically Hβ), G is the gravitational constant, and f is a dimensionless parameter dependent on the accretion rate and orientation. The parameter f assumes values $\approx 3/4$ in the case of an isotropic velocity field, $\approx$ 2-4 for Population A Quasars, and $f \approx 30$ for Blazars (Peterson & Wandel, 1999; Du et al., 2016; Punsly et al., 2018).

1.5 Estimation of accretion parameters

Accretion parameters, such as the BH mass and the Eddington Ratio, need to be estimated as they are crucial to properly classify AGNs and understand their properties. The BH mass is typically derived from reverberation mapping observations when available, however in this work we will estimate the SMBH mass using the scaling relation in Vestergaard & Peterson (2006):

$$M_{\rm BH} = \log\left(\left(\frac{\rm FWHM(H\beta)}{1000\ \rm km\ s^{-1}}\right)^2\left(\frac{L(5100\text{Å})}{10^{42}\ \rm erg\ s^{-1}}\right)^{0.5}\right) + (6.91 \pm 0.02), \tag{1.9}$$

where $L(5100\text{Å})$ is the luminosity of the object measured at the wavelength of 5100 Å. The BH mass obtained in this way is measured in solar masses ($M_\odot$).

Normally, as discussed in Shen & Liu (2012), the FWHM of lines such as MgII or CIV could in principle be used for the estimation of the black hole mass. However, as we did in this thesis, the adoption of Hβ as the principal virial estimator is the optimal choice, given its widespread availability for most Quasars.

The Eddington ratio can be estimated using the formula $L_{\rm bol}/L_{\rm Edd}$, with the Eddington luminosity $L_{\rm Edd}$ estimated as follows:

$$L_{\rm Edd} = 1.5 \times 10^{38}\rm erg\ s^{-1}\frac{M_{\rm BH}}{M_\odot}. \tag{1.10}$$

The bolometric luminosity of the AGN ($L_{\rm bol}$) is estimated for this calculation using the relation

$$L_{\rm bol} = L(5100\text{Å})k_{\rm bol}. \tag{1.11}$$

The bolometric correction factor $k_{\rm bol}$ is calculated using the formula from Netzer (2019):

$$k_{\rm bol} = 40 \times \left(\frac{L(5100\text{Å})}{10^{42}\ \text{erg s}^{-1}}\right)^{-0.2}. \tag{1.12}$$

Using these quantities, the properties of AGNs can be better understood and related to each other.

1.6 Towards a unified accretion scenario

Since the discovery of the MS of Quasars, the central question has revolved around whether populations A and B represent two extremes of the MS connected by some transitional mechanism or distinct Quasar populations. This inquiry arises from the direct dependence of emission line profiles and continuum strength on the central engine, particularly the black hole mass and accretion rate, as well as additional factors such as black hole spin and inclination (Czerny et al., 2017; Marziani et al., 2018; Panda et al., 2019; Panda & Marziani, 2023).

In Figure 1.6 from D'Onofrio et al. (2021), depicting the BH mass vs. luminosity diagram, Type-I AGNs in optically selected surveys seem to occupy a relatively narrow strip in parameter space as a function of the Eddington ratio. Within this strip, the Eddington ratio varies with $0.01 \lesssim L/L_{\rm Edd} \lesssim 1$. For $L/L_{\rm Edd} \lesssim 0.01$, accretion is expected to enter a radiatively inefficient regime, and selection effects may hinder the detection of the lowest accretors due to small $M_{\rm BH}$. This regime is believed to be primarily populated by sources such as Lineless AGNs and LINERs (Laor, 2004). Furthermore, sources radiating at $L/L_{\rm Edd} \gg 1$ likely do not exist, reaching an asymptotic Eddington ratio close to 2 or 3 (Sadowski et al., 2014; D'Onofrio et al., 2021). This limitation is attributed to an advection-dominated accretion flow, shielding the low-ionization emitting region from the luminous continuum visible to an observer at a small angle with respect to the disk (Giustini & Proga, 2019; Panda & Marziani, 2023).

In the context of the Quasar MS, it becomes evident that Population A is associated with increasing values of the Eddington ratio, reaching extreme values with xA sources. In contrast, Population B objects are linked to more modest accretion rates (Panda & Marziani, 2023).

Within this intricate framework, the role of the metallicity remains a topic that requires further exploration. Indeed, works such as Xu et al. (2018) have presented compelling evidence of chemically enriched BLRs in comparison to their host galaxies, making use of very large samples of high-redshift Quasars. In this work, it is evident that the BLRs of Quasars are significantly more chemically enriched than their hosts, raising questions on the origins of these metals. While in-situ star-formation seems a plausible explanation, a definitive answer has not yet been formulated due to lacking observational evidence (Xu et al., 2018).

While Xu et al. (2018) explored the relationship between metallicity and $M_{\rm BH}$, a MS representation of metallicity is yet to be established. Such a representation could effec-

tively address questions pertaining to the interplay between metallicity and the optical properties of Quasars, as well as their accretion parameters.

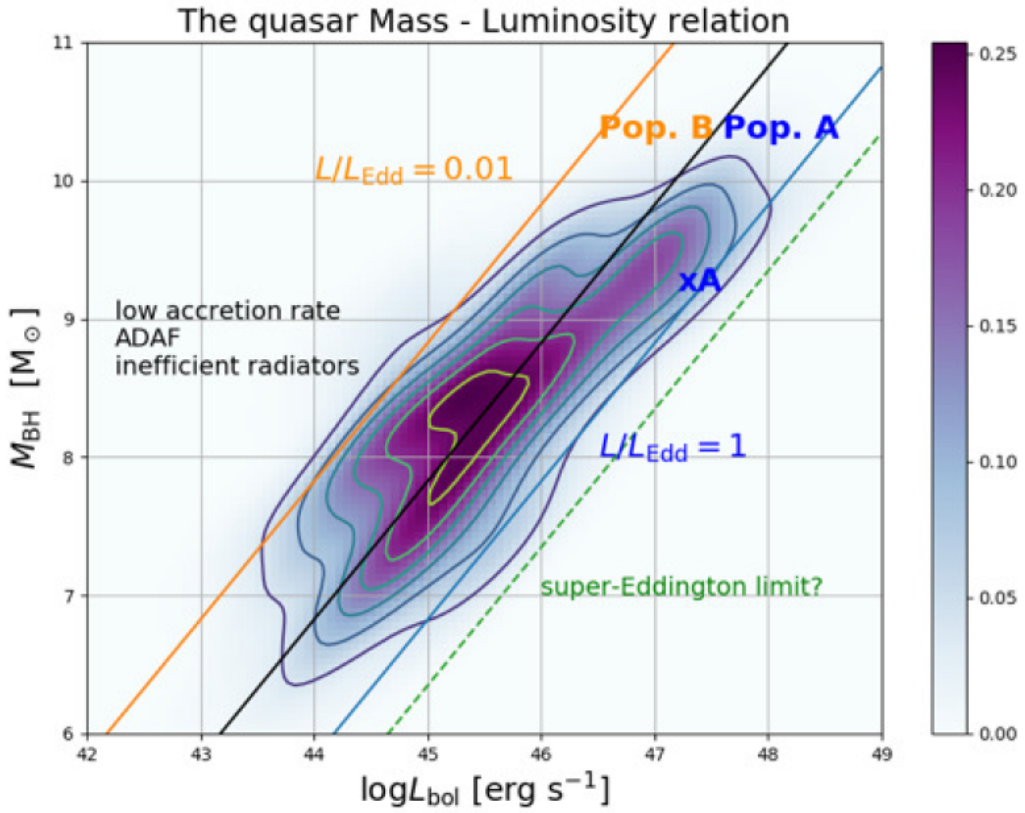

Figure 1.6: Mass-luminosity relation for a sample of $\approx$ 330 AGNs. The diagonal lines trace the values $\approx 0.01 L/L_{\rm Edd}$ and $\approx 1 L/L_{\rm Edd}$. It is evident that the wide majority of AGNs is included within this region, with Population A and B Quasars being shown with their characteristic Eddington ratio values. Figure from D'Onofrio et al. (2021).

1.7 Motivation and scheme of this work

The aim of this thesis is to determine a trend in the metallicity of the BLR along the MS of Quasars. Determining a metallicity trend in the BLR of Quasars is extremely important in order to understand the extent to which AGNs contribute to the chemical enrichment of their host galaxies, and to possibly constrain the mechanisms that allow this enrichment.

The thesis is organized as follows:

- **Chapter 1.** In this chapter, we presented a comprehensive overview of the properties of AGNs and introduced the Quasar MS. Section 1.1 provided a brief historical account of AGNs and explored their fundamental properties. Section 1.2 described

the Unification model of AGNs. Section 1.3 delineated how the Eigenvector 1 parameter space defines the Quasar MS, together with the Quasar populations that characterize it. In Section 1.4 the BLR of AGNs was described, explaining how the spectral lines employed in this study serve as valuable diagnostics of its properties. In Section 1.5 the scaling relations used to define the accretion parameters were defined. In Section 1.6 the accretion parameters were explored as additional tools to disentangle the intricate properties of AGNs. In Section 1.7 the motivations and the aims of this work were articulated.

- **Chapter 2.** In this chapter we describe in detail the sample of objects and the scientific techniques employed in this work. In Section 2.1 the sample is defined, briefly describing the peculiar properties of each object along with the observations with which its spectra were obtained. Section 2.2 describes the multi-component fitting technique, presenting its results. Section 2.3 defines the error estimation process. In Section 2.4 are explored the `CLOUDY` photoionization simulations employed in this work. Section 2.5 details the diagnostic ratios used for the estimation of properties in the BLR.

- **Chapter 3.** In this chapter the findings derived from our measurements are presented. Section 3.1 exhibits tables containing line measurements and diagnostic ratios, providing an overview of observational data. In Section 3.2 the methods and the results for the estimation of metallicity are discussed. Section 3.3 details the results related to the physical parameters that characterize the conditions within the BLR. Section 3.4 showcases the appearance of the sample objects in the Eigenvector 1 optical plane, as well as the correlations among the parameters that describe each object.

- **Chapter 4.** In this chapter the results of our measurements are discussed, contextualizing them with related studies. In Section 4.1 are evidenced the properties of the metal poor gas that characterizes the BLR of Population B objects. Section 4.2 delves into the presence of highly enriched gas in the BLR of xA Quasars. Section 4.3 examines the implications of our findings on feedback and galaxy evolution.

- **Chapter 5.** In this chapter the conclusions of this thesis work are reported. In Section 5.1 the conclusions from this work are drawn. In Section 5.2 further improvements that can be brought to the employed techniques are explored, and future projects are described.

Chapter 2

Sample and methodology

In this chapter we describe in detail the sample of objects and the scientific techniques employed in this work. In Section 2.1 the sample is defined, briefly describing the peculiar properties of each object along with the observations with which its spectra were obtained. Section 2.2 describes the multi-component fitting technique, presenting its results. Section 2.3 defines the error estimation process. In Section 2.4 are explored the `CLOUDY` photoionization simulations employed in this work. Section 2.5 details the diagnostic ratios used for the estimation of properties in the BLR.

2.1 Sample definition

The sample of objects used in this work was selected from a pool of 215 objects part of the same sample of Marziani et al. (2003). The following criteria were applied to select these objects:

1. Observations in the optical wavelength range, within a redshift of 0.8, where Hβ can be observed with ground-based telescopes.
2. Availability of archival UV data from HST covering the λ1300-2100 Å rest-frame range of the object
3. Requirement of radio quietness for all but one object, in order to study the properties of the BLR without the influence of a collimated jet (Baker et al., 1994; Punsly et al., 2018; Gaur et al., 2019).

After applying these selection criteria, the sample contained 12 objects. Two objects, PHL 1092 (Marinello et al., 2020) and TXS 0042+101 (Jackson & Browne, 1991), which are found in more extreme regions of the MS, were subsequently added to the sample. Although they were not originally part of the sample from Marziani et al. (2003), they were provided by Marinello et al. (2020) and digitized from Jackson & Browne (1991), respectively, bringing the total number of objects in the sample to 14.

In Table 2.1 the fundamental properties considered for the selection of the sample were summarized. Table 2.2 shows the derived properties considered for the selection of the sample, with the FWHM of Hβ measured from the line profile of the Hβ emission. R_{FeII} is calculated as described in Equation 1.4. The bolometric luminosity L_{bol}, the mass

of the SMBH and the Eddington ratio are estimated using Equations 1.11, 1.9 and 1.10, respectively. The applied procedure is extensively described in Section 1.5. The Kellerman Ratio, necessary to distinguish RQ from RL objects, is defined in Equation 1.2 using data from the NED database. However, when the NED data was not available, the flux density used in the calculation was obtained from other works. This is the case for Mrk 110, with the adopted flux density obtained from Wang et al. (2023a), while for Ark 564 it was taken from Järvelä et al. (2022). For Ton 28, LB 2522 and LEDA 51016 the Kellerman Ratio was adopted from the works Capetti et al. (2021), Baldi et al. (2022) and Kellermann et al. (1994), respectively.

Here follows a brief description of each object that constitutes the sample.

- **Mrk 335 - ST A1** Markarian 335 is a Population A Seyfert 1, spectral type A1. It is located in the nearby universe with a redshift of 0.0256, slightly changed from the original redshift in Marziani et al. (2003) of 0.025 because of inconsistencies with the UV spectral lines. This AGN exhibits characteristics typical of an RQ A1 AGN, with lower-than-average FeII emissions, positioning it in the lower-left corner of the MS. Emission lines in the UV and optical ranges exhibit little to no blueshifts in their profiles. The only exception to this typical behavior is the positive slope of its optical continuum, which is likely due to galactic extinction.

- **Mrk 110 - ST A1** Markarian 110 is a Population A Seyfert 1, spectral type A1. It is located at a redshift of 0.036. This object is peculiar with respect to a typical A1 AGN, due to the presence of a significant redshifted component in the line profile of CIVλ1549. This asymmetric component is, however, not present or unnoticed, in the line profiles of Hβ and SiIV+OIV]λ1400. The region associated to the CIII] blend was, however, not available and thus impossible to probe. It is nonetheless an object that has a spectrum remarkably similar to Mrk 335, with which shares the spectral type.

- **Mrk 509 - ST A1** Markarian 509 is a Population A Seyfert 1, spectral type A1. It is located at a redshift of 0.035. This object is a typical RQ A1 AGN. It exhibits low FeII emission, with lines with higher FWHM than other objects of the same spectral type.

- **Mrk 478 - ST A2** Markarian 478 is a Population A Seyfert 1, spectral type A2 Marziani et al. (2010), borderline A3. It is located at a redshift of 0.077. Although classified as A2, it exhibits characteristics that suggest it may be an extreme accretor. As a matter of fact, it displays a strong FeII emission and a pronounced outflowing component in its emission line profiles. Hence, it could be argued that Mrk 478 could be classified as an A3-type object.

- **Ark 564 - ST A2** Arakelian 564 is a Population A Seyfert 1, spectral type A2. It is located at redshift 0.025. This object exhibits the typical properties of A2 AGNs, with stronger-than-average FeII emission. Its UV spectrum is heavily absorbed, particularly underestimating the strength of its CIV line emission.

- **Ton 28 - ST A2** Tonantzintla 28 is a Population A Seyfert 1, spectral type A2. It is located at redshift 0.329. Ton 28, similarly to Mrk 478, is an object with some characteristics that might put into doubt its spectral type, placing it among the extreme-accreting objects, such as the presence of remarkable FeII and FeIII emissions. Due to the large distance of the object, however, its UV spectra, acquired with the Faint Object Spectrograph (FOS), have a lower Signal-to-Noise (S/N) ratio,

and are heavily absorbed. Thus, conclusively positioning it among A3 objects is not appropriate. Ton 28 should be regarded as spectral type A2, borderline A3.

- **I Zw 1 - ST A3** I Zwicky 1 is a Population A Seyfert 1, spectral type A3. It is located at redshift 0.061. The positioning of this object among extreme-accretors is clear as it has a very strong FeII and FeIII emission, with strong blueshifts in its HILs. As a matter of fact, the triangular profile of CIV is characteristic of xA objects due to the presence of strong outflows in the BLR of these objects (Kollatschny & Zetzl, 2013; Vietri et al., 2016). Templates used to model FeII and FeIII emission are based on spectra from this object, as referred in Section 2.2 (Vestergaard & Wilkes, 2001; Bruhweiler & Verner, 2008; Marziani et al., 2010).

- **LB 2522 - ST A3** Large Bright QSO Survey 2522, also known as PG 1259+593, is a Population A Seyfert 1, spectral type A3. It is located at redshift 0.472. This object is considered an extreme-accretor. Its strong FeII and FeIII emissions are coupled with the broadest lines among Population A objects of the sample, outlining a strong photoionizing continuum.

- **LEDA 51016 - ST A3** Lyon-Meudon Extragalactic Database 51016, also known as PG 1415+451, is a Population A Seyfert 1, spectral type A3. It is located at redshift 0.114. With a R_{FeII} of 0.97 it is considered a borderline A2-A3 object, leaning towards the xA population. As a matter of fact, its spectrum exhibits the peculiar CaII]λ1342 line, that seems to be present only in xA Quasars.

- **PHL 1092 - ST A4** Palomar Haro Luyten 1092 is a Population A Seyfert 1, spectral type A4. It is located at a redshift of 0.3965 (derived from the rest-frame position of the narrow component of [OIII]), this value slightly deviates from the less precise redshift of 0.394 reported in Marinello et al. (2020). Its spectrum is characterized by strong UV emissions, featuring a distinctively sloped SED. PHL 1092 is considered an extreme-accreting quasar, as it exhibits characteristics typical of that class. Notably, it exhibits a strong outflowing component in its emission line profiles, most notably its HILs, where the blueshifted emission casts a shadow on the virialized component. In the optical range, the Hβ emission is eclipsed by the FeII emission, mirroring the FeII profile of I Zw 1. This object stands as one of the most peculiar AGNs of the sample, being found at the extreme right of the MS.

- **Fairall 9 - ST B1** Fairall 9 is a Population B Seyfert 1, spectral type B1. It is located at redshift 0.046. It is a typical RQ B1 AGN, to the point that its spectrum almost coincides with the RQ B1 composite spectrum (Marziani et al., 2023).

- **Ark 120 - ST B1** Arakelian 120 is a Population B Seyfert 1 (Marziani et al., 1992), spectral type B1. It is located in the nearby Universe, at a redshift 0.033. It is a peculiar object with respect to a typical RQ Population B AGN because it presents a double-peaked profile, with two peaklets almost symmetrically displaced with respect to the rest frame by ~ 2000 km s^{-1}. The origin of the two peaks is not known at present. Ark 120 also presents a very strong FeII emission -peculiar for its kind- almost placing it among spectral-type B2 objects. Kuehn et al. (2008) evidenced that no reverberation lag was also present for the FeII component, suggesting an emitting region many times larger than the Hβ emitting region. However, Kuehn et al. (2008) admitted that no existing photoionization models can predict an emission as powerful as the one observed. In conclusion, although Ark 120 is a peculiar object, no conclusive explanation for its properties is possible at present time.

- **NGC 3783 - ST B1** New General Catalog 3783 is a Population B Seyfert 1, spectral type B1. It is the closest object of the sample, located at a redshift of 0.009. It is a well-known object, constantly monitored with reverberation mapping studies (Wang et al., 2022), and recently its BLR was spatially resolved (GRAVITY Collaboration et al., 2020).
- **TXS 0042+101 - ST B1$^+$** Texas Survey 0042+101 is a Population B Seyfert 1, spectral type B1$^+$. It is an object of uncertain redshift, with Jackson & Browne (1991) estimating a redshift of 0.583. A redshift of 0.587, consistent with Tang et al. (2012) was used in this work. The FWHM of its lines and absence of FeII emission clearly place TXS 0042+101 among B1$^+$ objects. As the only object in the sample with a $R_{\rm K} > 10$, it represents the RL population of Quasars.

Table 2.1: Fundamental properties of the sample

Object name	Spectral type	z	UV data source	Optical data source
(1)	(2)	(3)	(4)	(5)
Mrk 335	A1	0.0256	COS	M03
Mrk 110	A1	0.036	COS	M03
Mrk 509	A1	0.035	COS	M03
Mrk 478	A2	0.077	FOS	M03
Ark 564	A2	0.025	FOS, COS	M03
Ton 28	A2	0.329	FOS	M03
I Zw 1	A3	0.061	FOS, COS	M03
LB 2522	A3	0.472	FOS	M03
LEDA 51016	A3	0.114	FOS, COS	M03
PHL 1092	A4	0.3965	STIS	M20
Fairall 9	B1	0.046	FOS, COS	M03
Ark 120	B1	0.033	FOS	M03
NGC 3783	B1	0.009	FOS, COS	M03
TXS 0042+101	B1+	0.587	FOS	J91

Note. (1) Object common name. (2) Spectral type of the object. (3) Redshift of the object. (4) HST camera used for collecting UV spectra of the object. (5) Optical data source, using the abbreviations M03, M20 and J91 for the papers Marziani et al. (2003), Marinello et al. (2020), Jackson & Browne (1991), respectively.

2.1.1 Observations

Tables 2.3 and 2.4 describe the optical and UV observations, respectively. Optical observations for this sample were conducted between 1987 and 2014 (Jackson & Browne, 1991; Marziani et al., 2003; Marinello et al., 2020). Several ground telescopes from different locations were used:

- The ESO 1.52m telescope (ESO 1.52m) at La Silla, equipped with the Boller & Chivens (B&Ch) spectrograph;
- The Kitt Peak National Observatory 2.1m telescope (KPNO 2.1m) at Kitt Peak National Observatory, equipped with the Gold spectrograph;
- The Observatorio Astronómico Nacional 2.1m telescope (OAN 2.1m) at the Ob-

Table 2.2: Derived properties considered for the selection of the sample

Object Name	z	FWHM(Hβ) [km s^{-1}]	R_{FeII}	L_{bol} [10^{44} erg s^{-1}]	M_{BH} [$10^7 M_\odot$]	L/L_{Edd}	R_K
(1)	(2)	(3)	(4)	(5)	(6)	(7)	(8)
Mrk 335	0.0256	2175	0.34	7.42	2.45	0.20	0.42
Mrk 110	0.036	2048	0.19	2.73	1.17	0.16	2.18
Mrk 509	0.035	3309	0.02	18.60	10.20	0.12	0.35
Mrk 478	0.077	1322	1.04	20.00	1.76	0.76	0.20
Ark 564	0.025	1011	0.67	1.51	0.20	0.51	0.88
Ton 28	0.329	2402	1.04	198.00	30.10	0.44	< 0.40
I Zw 1	0.061	1012	1.74	36.00	1.47	1.63	0.40
LB 2522	0.472	3999	1.30	127.00	70.20	0.12	< 0.25
LEDA 51016	0.114	2959	0.97	17.60	8.45	0.14	0.17
PHL 1092	0.3965	2494	1.76	57.00	15.70	0.24	0.42
Fairall 9	0.046	5958	0.43	11.20	24.20	0.03	0.92
Ark 120	0.033	5863	0.49	24.20	37.50	0.04	0.30
NGC 3783	0.009	3514	0.20	2.40	3.10	0.05	0.30
TXS 0042+101	0.587	7279	0.04	39.20	120.00	0.02	197.37

Note. (1) Object common name. (2) Redshift of the object. (3) FWHM of Hβ. (4) FeII-to-Hβ ratio calculated in the λ4434-4684 Å range. (5) Bolometric luminosity. (6) Mass of the SMBH at the center of the galaxy, expressed in solar masses ($M_\odot$). (7) Eddington ratio associated with accretion onto the SMBH. (8) Kellerman ratio of the object.

servatorio Astronómico Nacional San Pedro Mártir, equipped with the Boller & Chivens (B&Ch) spectrograph;

- The 4.1m Southern Astrophysical Research Telescope (SOAR) at Cerro Tololo Observatory, equipped with the Goodman spectrograph;
- The Isaac Newton Telescope (INT) at Roque de Los Muchachos, equipped with the Intermediate Dispersion Spectrograph (IDS).

Observations in the UV wavelength range were performed using the Hubble Space Telescope in a period ranging from 1991 to 2022. Various instruments were employed: the Faint Object Spectrograph (FOS), the Cosmic Origins Spectrograph (COS) and the Space Telescope Imaging Spectrograph (STIS) were used for this endeavour, with spectra taken with various grisms, in order to cover the λ1320-2100 wavelength range.

The FOS was a spectrograph mounted on HST until February 1997, when it was decommissioned. It offered spectroscopic observations of objects from the near-UV to the near-infrared (Keyes & et al., 1995). Spectra taken with the FOS have a spectral resolution of 0.25 Å. The COS was mounted on HST in May 2009. It performs high-resolution spectroscopy of objects in the λ815-3200 Å range (Soderblom, 2023). Spectra taken with the COS have a spectral resolution of 0.1 Å. The STIS was mounted on HST in 1997. It performs spectroscopy of objects in the λ1150-10300 Å range (Medallon & Welty, 2023). UV spectra taken with the STIS used in this work have a spectral resolution of 0.5 Å for the SiIV range, while it has a spectral resolution of 1.5 Å for the CIV and CIII] ranges.

Because of the higher spectral resolution, when the full wavelength range was covered by both FOS and COS spectra, COS spectra were preferred in the fitting procedure. It is important to note that this does not affect the reliability of the measurements. However,

Table 2.3: Optical observations

Object name	Telescope	Instrument	Date of observation [dd mmm yyyy]	Observing time [s]
(1)	(2)	(3)	(4)	(5)
Mrk 335	ESO 1.52m	B&Ch	13 Oct 1996	3000
Mrk 110	KPNO 2.1m	Gold	15 Feb 1990	1800
Mrk 509	ESO 1.52m	B&Ch	12 Oct 1996	2400
Mrk 478	KPNO 2.1m	Gold	15 Feb 1990	1600
Ark 564	OAN 2.1m	B&Ch	24 Jun 2001	1800
Ton 28	ESO 1.52m	B&Ch	19 Dec 1993	3600
I Zw 1	ESO 1.52m	B&Ch	7 Oct 1994	3600
LB 2522	KPNO 2.1m	Gold	22 Apr 1991	3600
LEDA 51016	KPNO 2.1m	Gold	20 Feb 1990	3000
PHL 1092	SOAR	Goodman	12 Dec 2014	2700
Fairall 9	ESO 1.52m	B&Ch	20 Dec 1993	1800
Ark 120	ESO 1.52m	B&Ch	3 Apr 1990	1800
NGC 3783	ESO 1.52m	B&Ch	23 May 1993	3600
TXS 0042+101	INT	IDS	...	1000

Note. (1) Object common name. (2) Telescope used to carry out the observations. (3) Spectrograph used in the observations. (4) Date of observation. (5) Observing time through which the spectra were obtained, in seconds.

for two objects (I Zw 1 and LEDA 51016) the UV spectrum was not covered by coheval observations, leading to visible differences in the measured values of flux. This was corrected by scaling the flux in the affected spectral region making it coincide with the continuum of adjacent regions. An ulterior check of the objects' photometric variability over time using the Catalina Surveys Data Release 2 (Drake et al., 2022), confirming a variability that was compatible with experimental results.

Data reduction for these spectra was performed by the Space Telescope Science Institute (STScI), with manual wavelength corrections applied using the *Image Reduction and Analysis Facility* (`IRAF`) (Tody, 1993) task `dopcor` to account for redshift.

Table 2.4: Hubble Space Telescope Observations

Object name	Instrument	Grism	Date of observation [dd mmm yyyy]	Observing time [s]
(1)	(2)	(3)	(4)	(5)
Mrk 335	COS	G140L	04,07 Jan 2013	9221
Mrk 110	COS	G160M	03 Nov 2019	2448
Mrk 509	COS	G140L	03 Sep 2012, 11 Oct 2012	10080
Mrk 478	FOS	G130H, G190H	05 Dec 1996	3020
Ark 564	COS, FOS	G130M, G160M, G190H, G270H	23 Nov 2010, 23-24 May 1996	4060+2700
Ton 28	FOS	G190H, G270H	21 May 1992	3720
I Zw 1	COS, FOS	G160M, G190H, G270H	20-22 Jan 2015, 14 Sep 1994	11120+8130
LB 2522	FOS	G190H, G270H	27 Dec 1991	3277
LEDA 51016	COS, FOS	G160M, G190H, G270H	19 Feb 2022, 2 Jan 1997	7920+1507
PHL 1092	STIS	G230L	20 Aug 2003	5746
Fairall 9	COS, FOS	G130M, G160M, G190H, G270H	18 Jul 2012, 22 Jan 1993	11410+1260
Ark 120	FOS	G130H, G190H, G270H	19 Sep 1994, 29 Jul 1995	4610
NGC 3783	COS, FOS	G130M, G160M, G190H	27 Jul 1992, 12, 21 Dec 2016	2100
TXS 0042+101	FOS	G190H, G270H	04 Sep 1994	3204

Note. (1) Object common name. (2) Camera used in the observations. (3) Grism used in the observations. (4) Date of observation. (5) Observing time through which the spectra were obtained, in seconds.

```
# Mon 20:31:40 30-Jun-2008
begin   fixed_ciii_b
        task    specfit
components      9
                powerlaw
                usercont
                gaussian
                gaussian
                gaussian
                gaussian
                gaussian
                gaussian
                gaussian
                userline
                gaussian
                powerlaw1       2
                        32.27     0.        2000.   0.01 1.000000E-4  0
                        0.05    -5.0       12.     0.01 1.000000E-4  0
                usercont2   4  #Fe III] template
                        0.53       0.00     5.    0.001    1.00E-4    0
                        0.          -1.      1.   0.01     1.00E-4  0
                        0.       -0.001    0.001  0.001  1.00E-4  -1
                        16.58       0.00      30.0    0.001     1.00E-4  0
                gaussian3       4  #SiII
                        89.72      0.0      1000.         0.01     1.00E-4  0
                        1814.0   1810.00   1822.00   0.01     1.00E-4 0
                        5141.0    1000.0    7000.0   1.00     1.00E-4 0
                        1.00        0.     2.00      0.01     1.0E-4 -1
                gaussian4       4  #AlIII
                        72.       0.0       1000.0     0.01   1.00E-4   0
                        1855.   1850.00   1858.00  0.01   1.00E-4   0
                        4142.0   1000.0   7000.0   1.00   1.00E-4   0
                        1.00    0.        2.00     0.01    1.0E-4  -1
                   gaussian5       4  #AlIII
                        43.0    0.0       1000.0      0.8   1.00E-4   4
                        1862.0  1859.00   1870.00   1.004353 1.00E-4 4
                        4145.0   1000.0   7000.0    1.00 1.00E-4 4
                        1.00    0.        2.00      1. 1.0E-4 4
                    gaussian6       4  #SiIII]
                        383.     0.01      1000.0     0.01   1.00E-4 0
                        1887.0  1880.00   1895.00  1.02011 1.00E-4 4
```

Figure 2.1: Partial `Specfit` input file for the λ1900 blend fit of Ark 120.

2.2 Multi-component fitting technique

Our sample was analyzed using the `specfit` (Kriss, 1994) task from `IRAF`, inspecting the regions of our spectra centered on the SiIVλ1394, CIVλ1549, CIII]λ1909 and H$\beta\lambda$4861 lines. The wavelengths of these lines, as well as all other lines measured during the analysis, were obtained starting from the work of Vanden Berk et al. (2001). The `specfit` task runs on the *Space Telescope Science Data Analysis System* (`STSDAS`) `contrib` package of `IRAF`, which was developed by the *National Optical Astronomy Observatory* (NOAO) in Tucson, Arizona.

`Specfit` allows users to interactively fit a wide range of emission and absorption lines on the continuum model of the input spectrum. To achieve this, it employs input ASCII files created using the `dbcreate` task, containing the necessary functions to model various components of the spectrum. Gaussian and lorentzian functions, widely used in the multi-component fitting, are each described by values of line intensity, central wavelength, FWHM and asymmetry parameter. It is possible to see an example of the input file in Figure 2.1.

In addition to the standard functions provided, `specfit` allows the use of user-provided functions. In particular, we utilized the `usercont` and `userline` functions in order to model the complex FeIII (found in the UV range) and FeII (found also in optical ranges) emissions respectively.

The `specfit` multi-component fitting procedure is interactive, based on the input file described in the previous paragraphs. The initial parameter values in the input file serve as starting guesses for modelling the components. Each parameter can be refined by means of a minimization fit provided by the routine. This fitting is carried out by χ^2

minimization with one of five different algorithms:

- **Marquardt** is based on the Levenberg-Marquardt (LM) algorithm, which iteratively minimizes the χ^2 using the Jacobian matrix. This matrix contains the partial derivatives of the model function fitting the data with respect to each fit parameter. The algorithm combines a combination of gradient descent and Gauss-Newton methods, adjusting the step-size at each iteration. It takes larger steps when the fitting improves, and smaller steps when it does not. When the algorithm converges successfully, it provides the best-fit parameters that minimize the difference between the model and observed data, resulting in an optimal solution.

- **Simplex** utilizes an iterative method for fitting, adjusting values for user-provided components starting from initial guesses and constraints. It iteratively improves the solution, identifying "entering" and "leaving" variables, which are variables that can be increased or decreased to improve the solution, respectively. When an optimal solution is found or the number of iteration is reached, the algorithm returns the best fit.

- **Numrecipe** is based on the Marquardt-type algorithm described in Press et al. (1986), and is generally the most effective and fastest.

- **Gridfit** employs a grid-type fitting algorithm, starting from user-defined lower and upper limits. It increments the parameters within the specified limits and calls one of the other fitting algorithms at each step, recording the best combination of values in a log file. This algorithm, however, tends to be slow.

- **Alternate** which alternates between calling the Numrecipe and Simplex algorithms.

During this work, we only used the first three fitting algorithms. Upon completing the fitting, two files are generated:

- a "log" containing detailed information about the various components, including their final values after χ^2 minimization;

- a "plot" ASCII file suitable for plotting the input spectrum, the model spectrum obtained through χ^2 minimization, and the individual components.

The multi-component fitting process with `specfit` adheres to a methodology consistent with the current understanding of the BLR physics, as discussed in Section 1.4. We start by fitting the continuum emission in the selected wavelength range with a power-law function, carefully selecting regions of the spectrum unaffected by the presence of emission or absorption lines. The flux values of the continuum at various reference wavelengths are provided in Table 2.5.

In the optical wavelength range we incorporate a FeII template to correct for FeII contamination, which can act as a pseudo-continuum on the modeled spectrum, particularly problematic in objects with strong FeII emission. Our FeII template is derived from a European Southern Observatory (ESO) spectrum of I Zw 1 (Marziani et al., 2009, 2010). To address FeIII contamination, prevalent in the λ1700-2100 Å wavelength range, we utilize a template from Vestergaard & Wilkes (2001), based on the FeIII emission of I Zw 1. In cases where the FeIII feature at 1914 Å blends with CIII]λ1909 Å, we account for this effect by modeling the 1914 Å feature with a Gaussian profile. This step is typically necessary for xA objects.

When fitting emission lines, we allow them to vary while imposing the Narrow Component (NC) of lines to remain fixed at the rest-frame of the object. Additionally, we ensure that the FWHM of lines in the CIII] and SiIV ranges is similar to those measured for CIVλ1549 and Hβ (Marziani et al., 2010). This is because lines associated with the virialized components of Hβ, CIII], CIV and SiIV are produced in approximately the same regions. On the other hand, the BLUE and VBC lines are left free to vary since they are generated in regions with significantly different physical conditions.

Figures from 2.2 to 2.8 display the best-fit spectra of the sample.

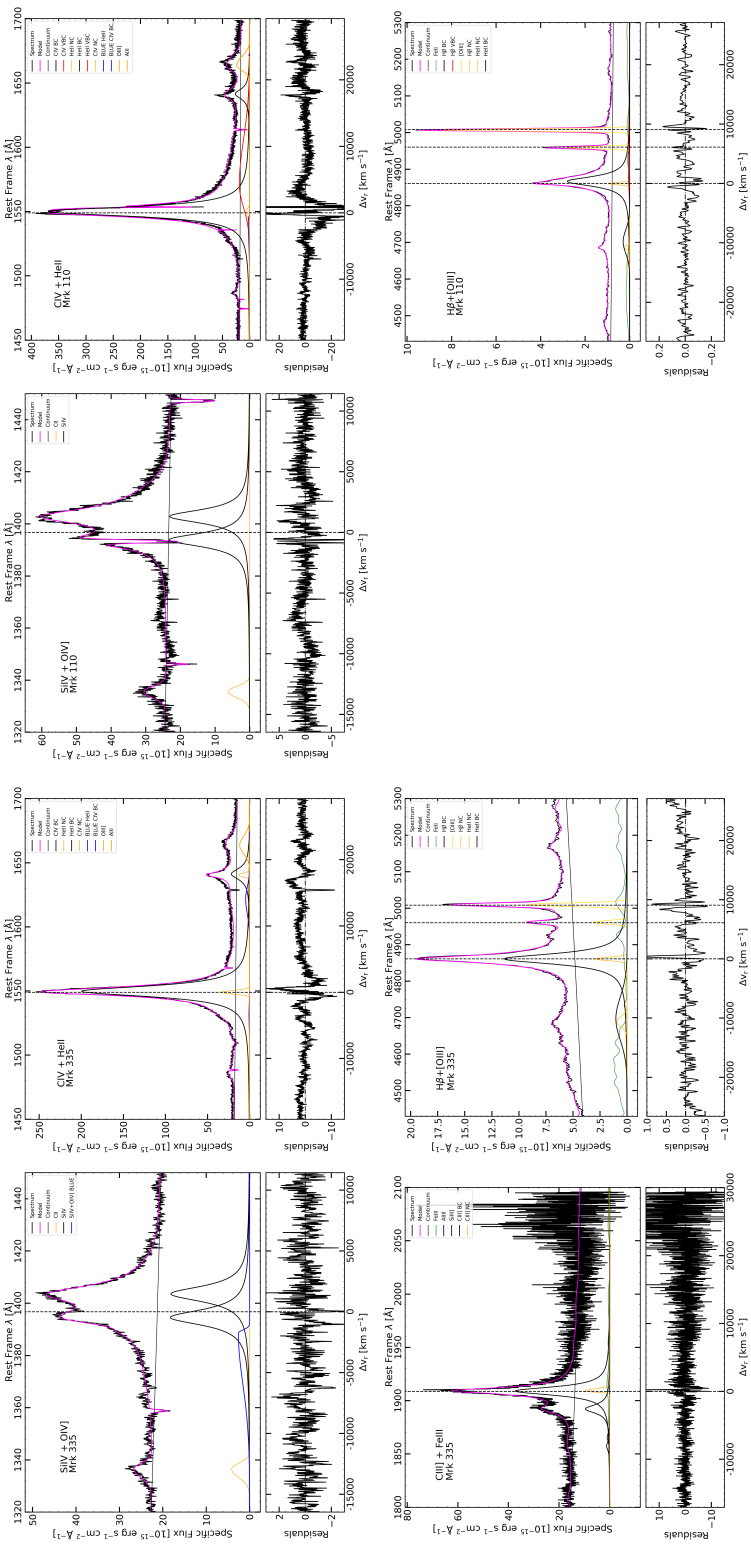

Figure 2.2: Spectral fits of Mrk 335 (left four images) and Mrk 110 (right three images) in the wavelength ranges considered, with specific fluxes measured in units of 10^{-15} erg s^{-1} cm^{-2} Å^{-1} and the wavelength measured in Å. A lower box is associated to each spectral fit, with wavelength expressed in units of radial velocities (km s^{-1}). The original spectrum is plotted with a black line and the modeled spectrum is plotted in magenta. Each additional line component is plotted with a different color, according to the legend. Dashed vertical lines represent the rest-frame wavelengths of the main lines of the selected spectral range. *Top left*: λ1320-1450 Å range. *Top right*: λ1450-1700 Å range. *Bottom left*: λ1800-2100 Å range. *Bottom right*: λ4430-5300 Å range.

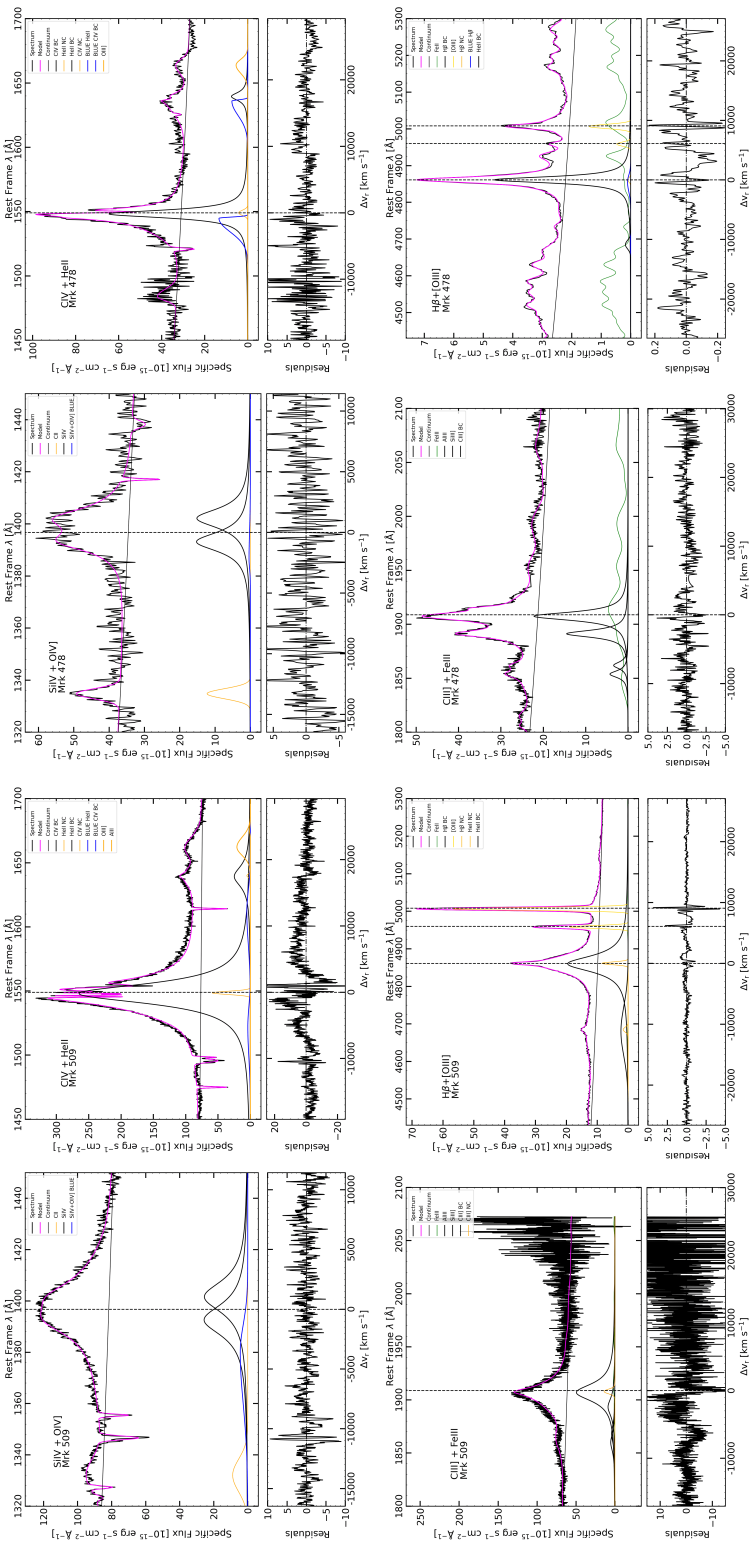

Figure 2.3: Same as in Figure 2.2, but for Mrk 509 (left four images) and Mrk 478 (right four images).

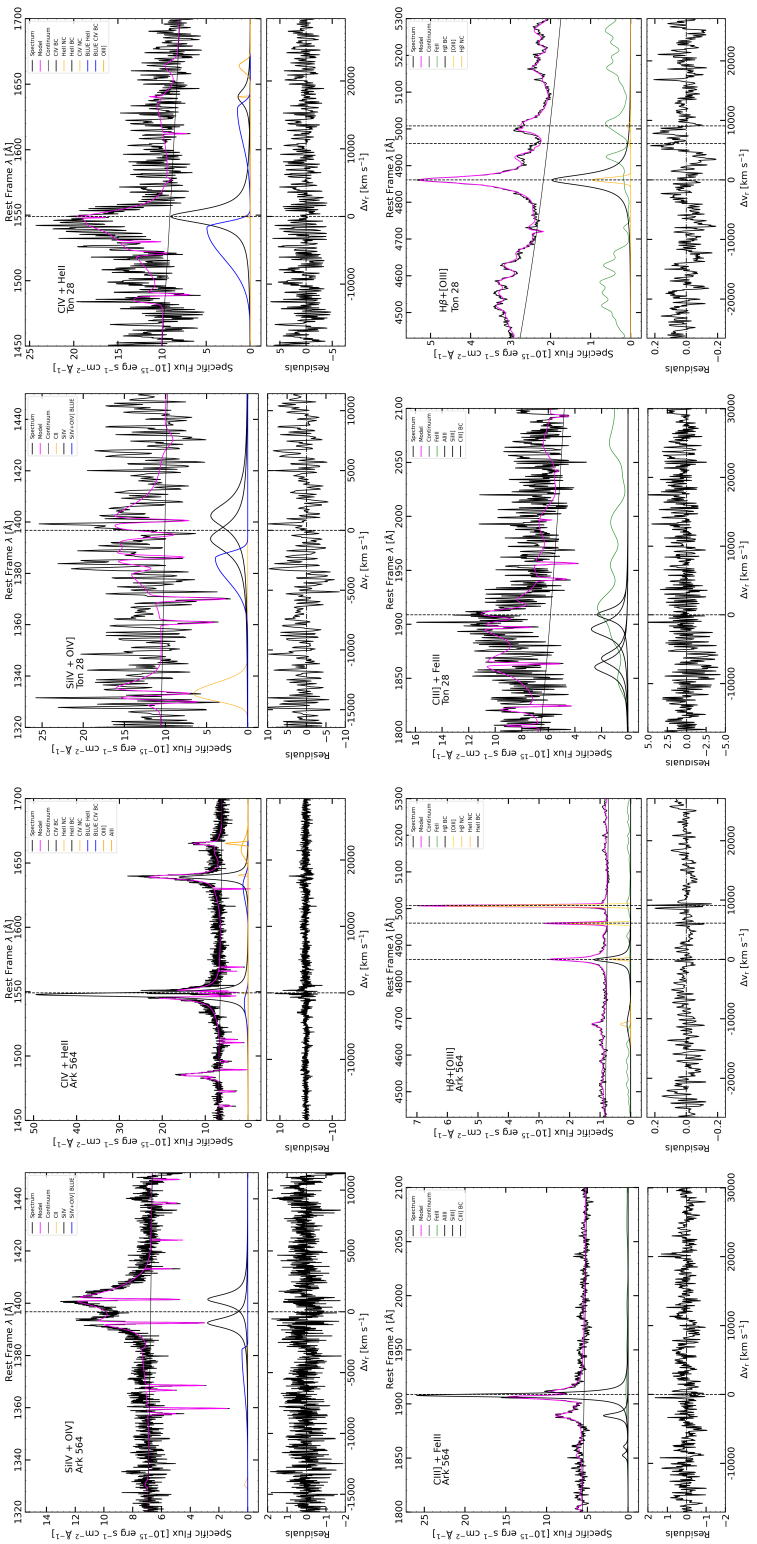

Figure 2.4: Same as in Figure 2.2, but for Ark 564 (left four images) and Ton 28 (right four images).

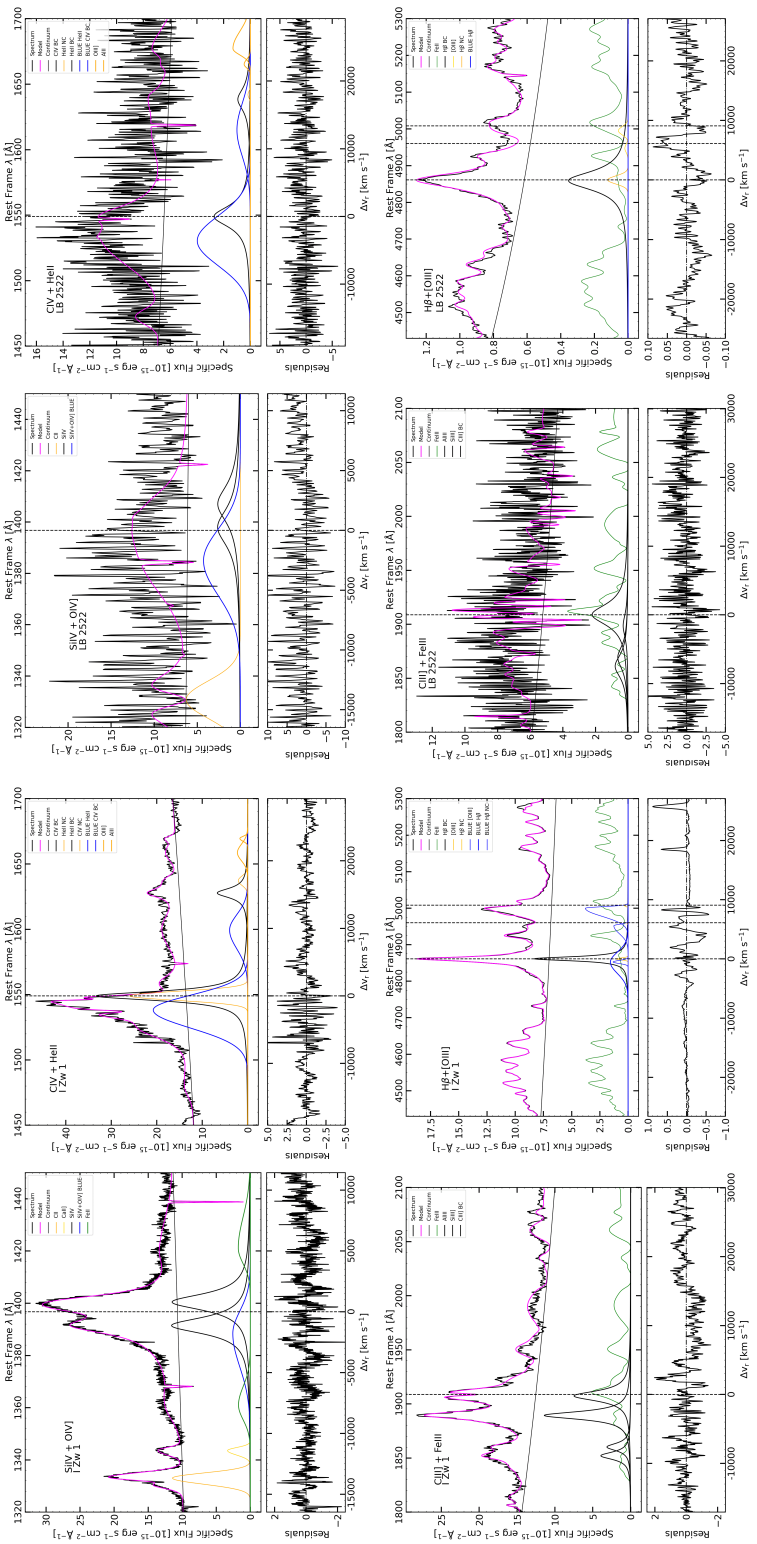

Figure 2.5: Same as in Figure 2.2, but for I Zw 1 (left four images) and LB 2522 (right four images).

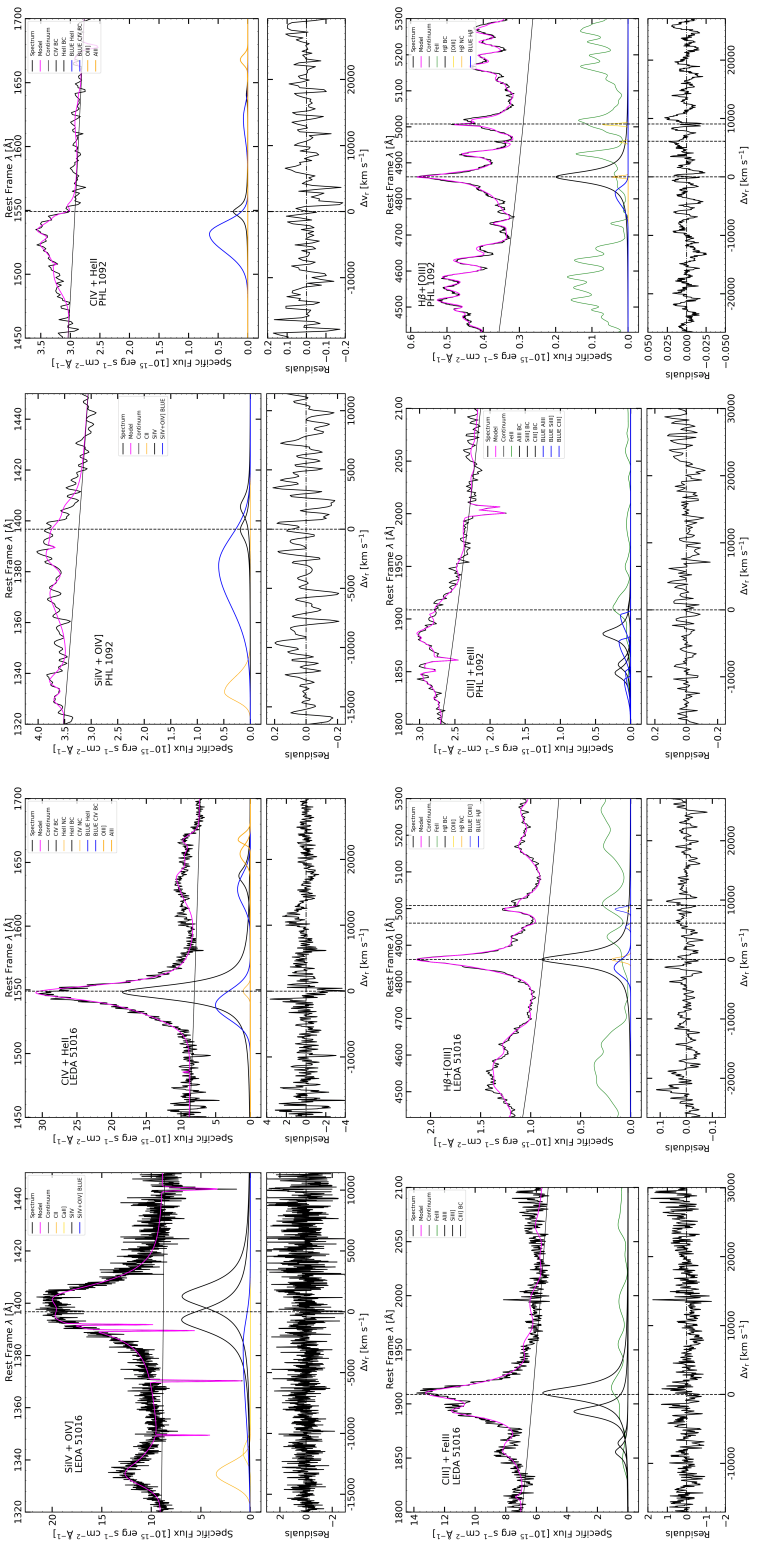

Figure 2.6: Same as in Figure 2.2, but for LEDA 51016 (left four images) and PHL 1092 (right four images).

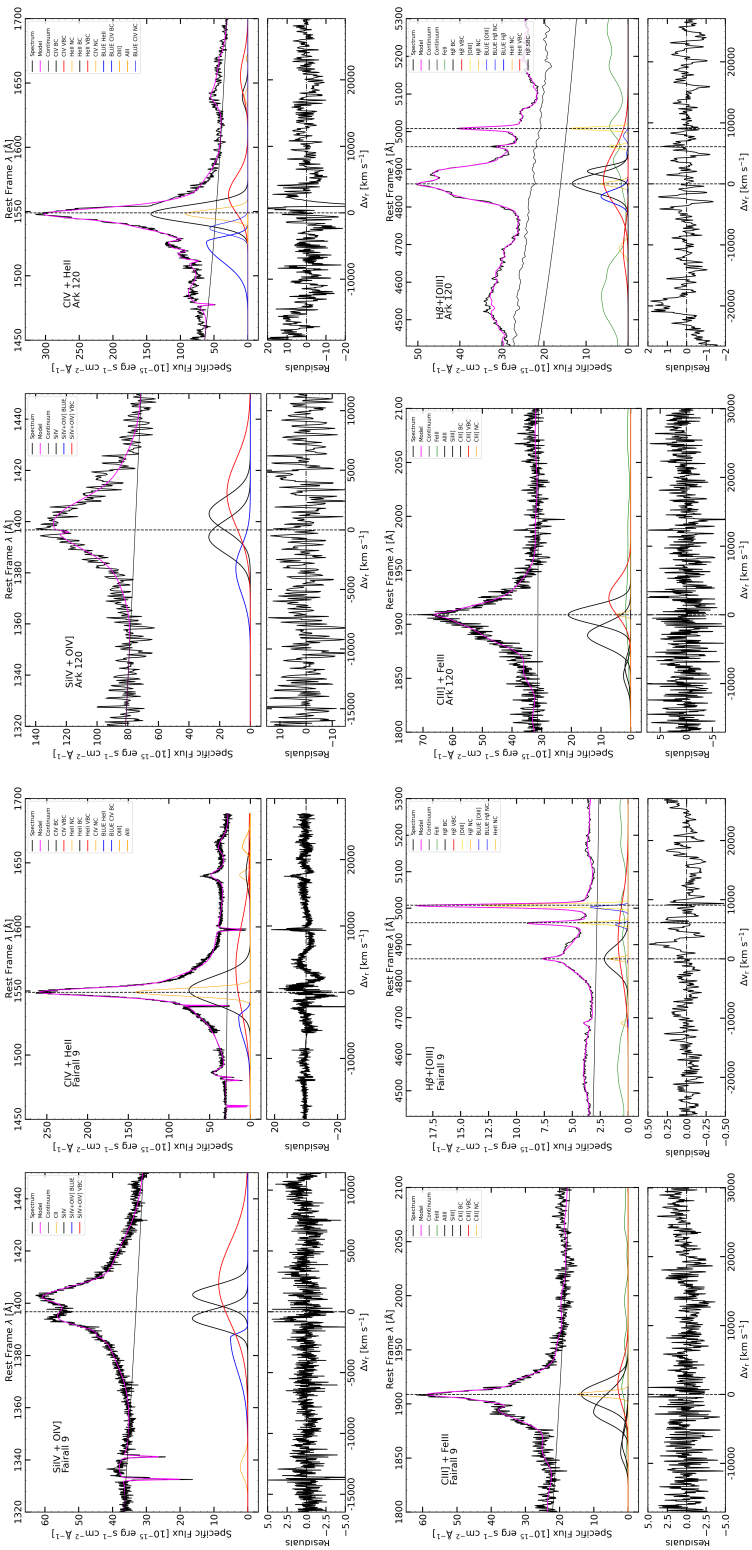

Figure 2.7: Same as in Figure 2.2, but for Fairall 9 (left four images) and Ark 120 (right four images).

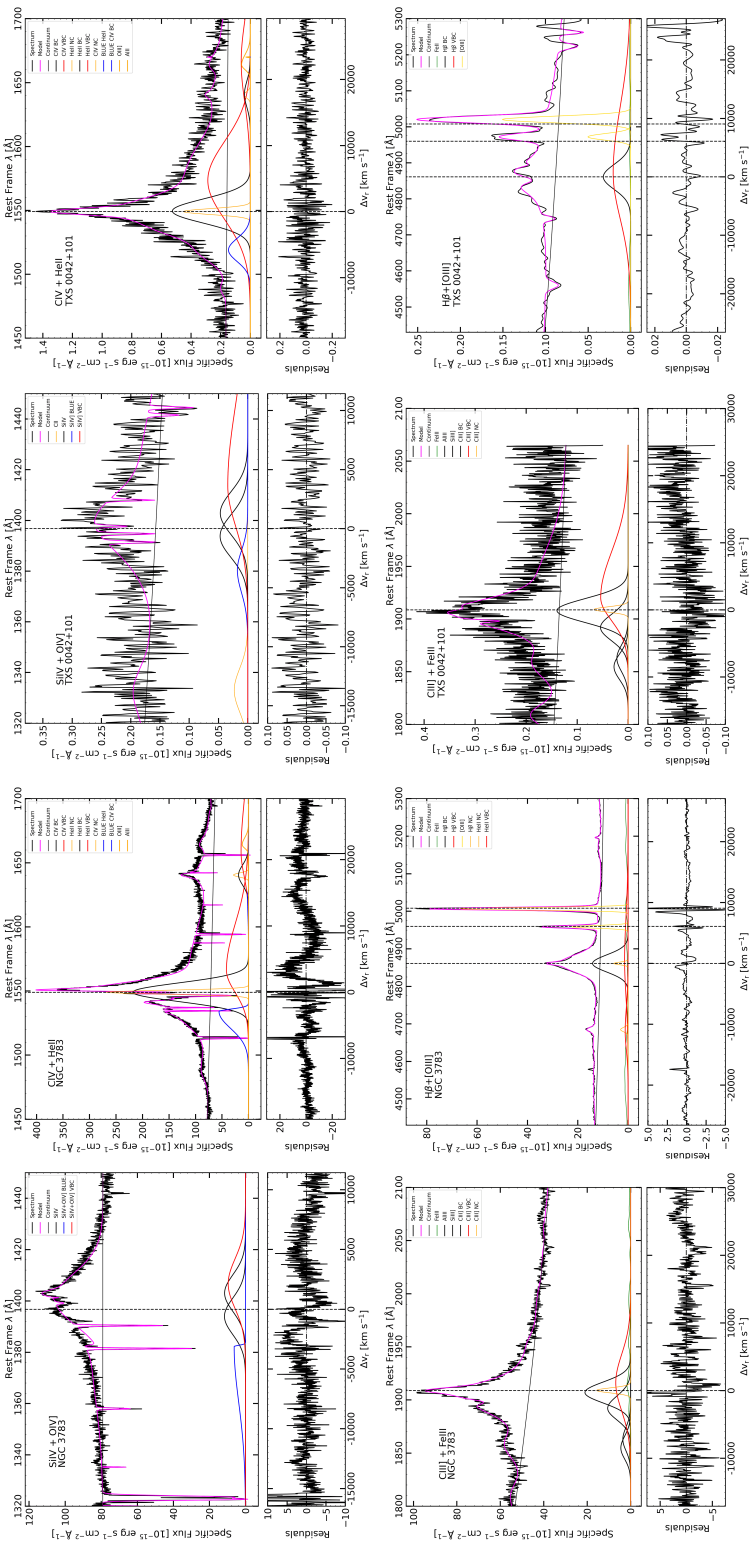

Figure 2.8: Same as in Figure 2.2, but for NGC 3783 (left four images) and TXS 0042+101 (right four images).

2.3 Estimation of uncertainties

Using `Specfit`, the placement of the continuum is the main source of uncertainty in measuring emission-line intensities. Additionally, it is evident from the fits in Figures from 2.2 to 2.8 that, in the majority of cases, the FWHM of AlIII and SiIII] (assumed to be equal) closely matches the FWHM of $\mathrm{CIV}_{\mathrm{BC}}$, $\mathrm{SiIV}_{\mathrm{BC}}$, $\mathrm{CIII}]_{\mathrm{BC}}$ and $\mathrm{H}\beta_{\mathrm{BC}}$.

In particular, the continuum placement strongly influences extended features such as the FeIII and HeIIλ1640 emissions in the UV range, and the FeII emission in the Hβ range. It is thus of the utmost importance to set boundaries within which the continuum can affect the intensity of emission lines.

This was accomplished as follows, mirroring the methodology in Śniegowska et al. (2021): initially, the intensity of the continuum was measured using `IRAF` in each range where the best fit was conducted, yielding the Root Mean Square (RMS) of the flux (measured in units of 10^{-15} erg s^{-1} cm^{-2} Å^{-1}), as shown in Table 2.5. Subsequently, the intensity of each line was measured by fixing the continuum's intensity at both maximum and minimum values, by adding or subtracting the RMS, to obtain the line's intensity at its minimum and maximum, respectively. As a matter of fact, when the continuum is higher (lower), the line intensity decreases (increases), compensating for the flux change, resulting in lower (upper) limits that are asymmetric and represent the range of emission line intensities.

In order to handle these uncertainties, we assume that the error distribution follows a triangular distribution (D'Agostini, 2003). This simplifies error computation and is the preferred method for dealing with asymmetric uncertainties. For each line measurement, the variance ($\sigma^2(X)$) is calculated using the formula for the triangular distribution:

$$\sigma^2(X) = \frac{\Delta^2 x_+ + \Delta^2 x_- + \Delta x_+ + \Delta x_-}{18} \tag{2.1}$$

where Δx_+ and Δx_- represent the differences between measurements with maximum and best continuum, and with best and minimum continuum, respectively. Finally, errors on spectral diagnostic ratios were calculated using standard error propagation formulas.

2.4 CLOUDY photoionization simulations

In order to constrain the properties of the gas in the BLR, we conducted photoionization simulations using the `CLOUDY` algorithm (Ferland et al., 2017). `CLOUDY` is a `C++` code that models the ionization, chemical, and thermal state of the material that may be exposed to an external radiation field or other sources of heating. It predicts observables, including emission and absorption spectra, by solving the statistical equilibrium equation for many chemical species, including ions. The code accounts for collisional excitations, radiative processes, and treats radiation transfer through a probability formalism.

The simulations employed in this work are similar to those used in Marziani et al. (2020). Photoionization simulations require input parameters that define ionization and level populations, along with electron temperature and optical thickness as a function of the geometrical depth within the emitting gas cloud. The assumed geometry is open and plane-parallel, representing a cloud of emitting gas as a slab exposed to a radiation field only on one side.

Table 2.5: RMS

Object name	Opt	SiIV	CIV	CIII]	$f_{\lambda 1350}$	$f_{\lambda 1700}$	$f_{\lambda 5100}$
(1)	(2)	(3)	(4)	(5)	(6)	(7)	(8)
Mrk 335	0.12	0.65	0.70	1.30	22.11	14.83	5.25
Mrk 110	0.03	1.57	1.74	...	24.01	16.02	0.76
Mrk 509	0.31	1.71	2.10	1.91	84.18	73.99	8.87
Mrk 478	0.02	2.06	0.93	0.52	36.23	26.93	2.00
Ark 564	0.04	0.52	0.84	0.27	6.86	6.06	0.75
Ton 28	0.04	3.11	1.38	1.25	10.36	7.98	1.93
I Zw 1	0.12	0.49	0.70	0.37	10.15	16.43	6.65
LB 2522	0.02	2.08	1.67	1.27	6.25	5.89	0.54
LEDA 51016	0.02	0.55	0.45	0.26	8.19	7.22	0.78
PHL 1092	0.01	0.08	0.06	0.07	3.40	2.77	0.28
Fairall 9	0.09	0.91	1.63	1.19	35.19	26.36	2.72
Ark 120	0.22	5.51	2.27	1.97	78.86	30.94	13.83
NGC 3783	0.20	2.05	2.84	2.09	79.16	63.26	10.36
TXS 0042+101	0.01	0.05	0.04	0.03	0.17	0.15	0.08

Note. (1) Object common name. (2), (3), (4), (5) Root Mean Square of the flux associated to the continuum emission, measured in units of 10^{-15} erg s^{-1} cm^{-2} Å^{-1}, in the ranges of the various lines inspected in this work. (6) Specific flux of the continuum emission measured at 1350 Å, measured in units of 10^{-15} erg s^{-1} cm^{-2} Å^{-1}. (7) Specific flux of the continuum emission measured at 1700 Å, measured in units of 10^{-15} erg s^{-1} cm^{-2} Å^{-1}. (8) Specific flux of the continuum emission measured at 5100 Å, measured in units of 10^{-15} erg s^{-1} cm^{-2} Å^{-1}.

The input parameters for a complete computation of the gas state, used to predict emission line intensities, include:

1. The ionization parameter U, defined by the equation:

$$U = \frac{\int_{\nu_0}^{\infty} \frac{L_\nu}{h\nu}\, d\nu}{4\pi r_{\rm BLR}^2 c n_{\rm H}} = \frac{Q({\rm H})}{4\pi r_{\rm BLR}^2 c n_{\rm H}}, \tag{2.2}$$

   where Q(H) is the number of ionizing photons, $r_{\rm BLR}$ is the distance between the continuum source and the line emitting gas. It provides the ratio between the Hydrogen-ionizing photons and the Hydrogen number density.

2. Gas Hydrogen density $n_{\rm H}$.

3. Metallicity Z, with respect to solar metallicity $Z_\odot$, defined as $\log Z = \log[\frac{Z}{H}] - \log[\frac{Z}{H}]_\odot$, where $[\frac{Z}{H}]$ and $[\frac{Z}{H}]_\odot$ are the ratio of the measured number density of metals with respect to Hydrogen, and the same quantity for the Sun, respectively.

4. SED of the Quasar.

5. Column density $N_{\rm c}$.

6. Micro-turbulence parameter (Panda et al., 2018).

Evidence indicates trends for various parameters along the Quasar MS. Specifically, in the case of Population B, there is observable evidence of a radial stratification of properties within the BLR (Baldwin et al., 1995; Korista et al., 1997). As previously mentioned, this region is modeled by distinguishing between a BC and a VBC.

While the assumption of constant physical parameters within the BLR is not entirely accurate for Population A, this complexity is addressed by modeling and separating the BLUE from the BC, especially in the context of extreme-accretors, as discussed more extensively in Negrete et al. (2012). This modeling approach allows for a deeper understanding of the characteristics within the BLR for different populations of Quasars.

This resulting six-dimensional parameter space is not typically fully explored, and in our case we examined trends using arrays of simulations that were organized as follows: 3 different SEDs, one for each of the following cases: Pop. B RQ, a SED for Population A sources (Mathews & Ferland, 1987) and one for xA Quasars (Ferland et al., 2020). Metallicity (Z) was assumed to scale as solar ($Z_{\odot}$), with 12 values ranging between 0.01 and 1000 $Z_{\odot}$ for Pop. A and 14 values between 0.001 and 20 $Z_{\odot}$ for Pop. B. The microturbulence parameter was set to 0 km s^{-1}. This has been shown to be negligible for resonance UV lines as outlined in (Śniegowska et al., 2021), but is expected to lead to an under-prediction of FeII emission (Sigut & Pradhan, 2003; Śniegowska et al., 2021). For each metallicity value, we considered an array of simulations covering the n_H and U parameter plane in the range $7 \leq \log n_{\rm H} \leq 14$ cm^{-3}, $-4.5 \leq \log U \leq 1$ for Pop. A (667 simulations), and $7 \leq \log n_{\rm H} \leq 13$ cm^{-3}, $-3 \leq \log U \leq 1$ for Pop. B (425 simulations).

2.5 Diagnostic ratios

Diagnostic ratios of lines provide constraints on the ionization, metallicity and density of the emitting gas in the BLR (Marziani et al., 2020). The fundamental diagnostic ratios used for computing the metallicity are described as follows:

1. **(SiIV+OIV])/CIV**: widely used as a metallicity indicator (Nagao et al., 2006; Shin et al., 2013). In photoionization equilibrium, as metallicity in the BLR increases, the electron temperature decreases as in HII regions Pagel et al. (1979). This leads to a decrease in the CIV line intensity. This effect resides in the competition between He^+ ions and C^{2+} ions, which have similar ionization potentials, making it a solid metallicity indicator (Huang et al., 2023).

2. **(SiIV+OIV])/HeII**: sensitive to metallicity, assuming that He abundance relative to Hydrogen is constant. The OIV] line has a critical density $n_{\rm c}\sim 10^{11}$ cm^{-3} (Marziani et al., 2020), making this diagnostic ratio also a powerful density indicator.

3. **CIV/HeII**: diagnostic ratio sensitive to metallicity and C abundance, assuming constant He abundance relative to Hydrogen. The ionization potentials of C^{2+} and He^+ are similar, however the main difference is that HeII is a recombination line, and the regions where CIV and HeII form are different (Śniegowska et al., 2021). This ratio has been used consistently in the past (Shin et al., 2013), however, with more and more precise measurements from FOS and COS, we are able to estimate accurately the line intensity of CIV and HeII, previously very difficult to assess.

4. **AlIII/CIV**: a diagnostic ratio sensitive to the ionization parameter. This is because it relates lines of elements with different ionization potentials. It is also extremely

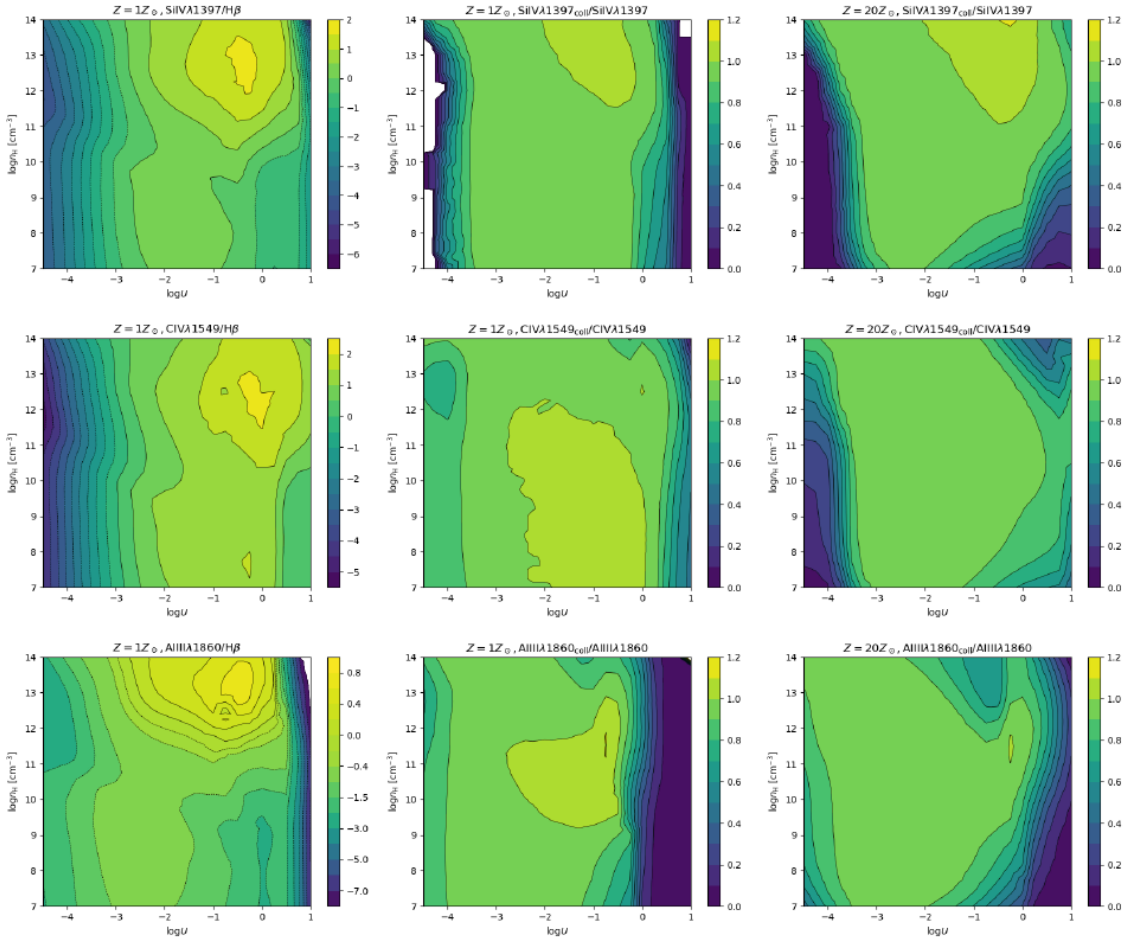

Figure 2.9: *Left*: Decimal logarithm of the ratio between resonance emission lines and Hβ as a function of ionization parameter and Hydrogen density, from arrays of 667 simulations from `CLOUDY` 17.02. From top to bottom: SiIV, CIV, AlIII. *Middle*: Ratio of collisional excitation emission to the total line emission as a function of U and $n_{\rm H}$, with $Z = 1Z_{\odot}$. *Right*: Ratio of collisional excitation emission to the total line emission as a function of U and $n_{\rm H}$, with $Z = 20Z_{\odot}$. Figure from Marziani et al. (2020).

useful in order to constrain the effect of feedback from Supernovae, since AlIII is a product of the explosion of massive stars (Śniegowska et al., 2021). It is thus likely that this diagnostic ratio tends to increase the resulting metallicity.

5. **AlIII/SiIII**]: a diagnostic ratio sensitive to density, since it involves an intercombination line with a well-defined critical density: $n_{\rm c} \sim 10^{11}$ cm^{-3} for SiIII] (Negrete et al., 2013). If the ratio AlIII/SiIII] is $\gg 1$, the resulting density will be much greater than the critical density. For these reasons, it is extremely useful as an estimator of the gas density. As the previous diagnostic ratio, since it involves Aluminium, it tends to increase the resulting metallicity. Historically, diagnostic ratios employing AlIII have rarely been used, since the measurement of the intensity of AlIII was quite uncertain, but with high quality COS and FOS spectra we have

been able to measure it accurately.

6. **SiIII]/CIII]**: a diagnostic ratio sensitive to density, similar to AlIII/SiIII], with $n_c \sim 10^{10}$ cm^{-3} for CIII] (Hamann et al., 2002). As the ratio described above, if SiIII]/CIII] is $\gg 1$, the resulting density will be much greater than the critical density of CIII] as well, and is a very powerful density estimator, constraining density very well.

7. **CIII]/CIV**: it is a diagnostic ratio sensitive to the ionization parameter as it compares the intensity of different ionization degrees of the same atomic species. However, since CIII] is an intercombination line, it is also sensitive to density. Unfortunately, for xA objects in particular, it is subject to higher uncertainties due to FeIII contamination, making it difficult to measure the intensity of CIII] accurately.

8. **FeII/Hβ**: it is a diagnostic ratio sensitive to metallicity, as it involves a metal and Hydrogen. However, this diagnostic ratio is also sensitive to density, ionization parameter and column density of the line-emitting gas. As a matter of fact, high FeII/Hβ is only possible if conditions of low ionization, large column density ($n_H \gtrsim 10^{11}$ cm^{-3}) and very high density ($n_C \gtrsim 10^{23}$ cm^{-2}) are satisfied (Panda et al., 2018, 2019).

9. **HeII$_{opt}$/Hβ**: it is a diagnostic ratio sensitive to the ionization parameter. Assuming the abundance of He relative to Hydrogen is constant, it is the ratio between two species with very different ionization potential: HeII requires ~ 50 eV to be ionized, while Hydrogen requires ~ 10 eV.

These diagnostic ratios are used differently depending on the Quasar population. As a matter of fact, Population A objects allow reliable estimation only of physical parameters associated with the BC. Population B Quasars allow for the estimation of physical parameters of gas located in the VBC and BC, while xA Quasars allow for the estimation of the properties of the BLUE and BC.

Notably, not all components are present in all objects, as can be seen in Tables from 3.1 to 3.4. Although most objects can be modeled assuming a BLUE component for HILs, it is not present for LILs, and thus this affects their reliability for the estimation of physical parameters. The same principle can be applied to the VBC, which appears only in Population B sources.

An uncertainty associated with this approach comes from the fact that photoionization computations are carried out under the assumption of single-zone emission. While this assumption seems a good one for extreme Population A, where density and ionization tend toward limiting values Panda et al. (2019), this might not be the case for Pop. B sources. Moreover, the non-simultaneity of the observations in the optical and UV leads to uncertainties as well. As we can see in Section 2.1.1, optical and UV observations are typically separated by years. In addition, problems associated to photometric intercalibration between optical and UV data might arise: while space-based observations are precise within about $\sim$ 5-10%, optical data are affected by uncontrolled light loss. As a result, the ratio CIV/Hβ was measured but considered for the estimation of metallicity in a case-by-case scenario, because of the intrinsic variability of the sources.

This variety of diagnostic ratios sensitive to different physical quantities is essential to reduce the number of degrees of freedom of the system and to better constrain the metallicity, density and ionization parameters.

Chapter 3

Results

In this chapter the findings derived from our measurements are presented. Section 3.1 exhibits tables containing line measurements and diagnostic ratios, providing an overview of observational data. In Section 3.2 the methods and the results for the estimation of metallicity are discussed. Section 3.3 details the results related to the physical parameters that characterize the conditions within the BLR. Section 3.4 showcases the appearance of the sample objects in the Eigenvector 1 optical plane, as well as the correlations among the parameters that describe each object.

3.1 Diagnostic ratios tables

In the Tables from 3.1 to 3.4 are displayed the line measurements with associated errors for the SiIV, CIV, λ1900 and Hβ blends, respectively. Line measurements are computed integrating the flux of each line component along the wavelength range in which the line extends from the best-fits of each object obtained using the `IRAF Specfit` task. Line intensities are then corrected for galactic extinction using the equations from Cardelli et al. (1989).

The following equation is used:

$$A(\lambda) = A(V)\,(a(x) + b(x)/R_V)\,, \tag{3.1}$$

where $A(V)$ is the object's absorption coefficient in the V band, R_V is the absorption parameter characteristic for our galaxy and fixed at 3.1, $a(x)$ and $b(x)$ are polynomial functions described in Cardelli et al. (1989), with x a parameter defined as

$$x = \frac{10000}{\lambda(1+z)} - 1.82, \tag{3.2}$$

where z is the redshift of the object and the wavelength λ is expressed in Å.

The values of $A(V)$ were obtained from the NED database for each object, while the redshift assumed was the one measured in this work.

Table 3.1: SiIV+OIV] blend line measurements.

Object name	SiIV+OIV]		
	BLUE	BC	VBC
(1)	(2)	(3)	(4)
Mrk 335	85.24 ± 25.37	634.85 ± 74.59	...
Mrk 110	...	706.30 ± 104.86	...
Mrk 509	251.73 ± 98.85	1858.56 ± 299.68	...
Mrk 478	6.88 ± 22.84	540.74 ± 121.78	...
Ark 564	11.50 ± 10.48	115.52 ± 24.45	...
Ton 28	63.52 ± 40.72	199.18 ± 139.16	...
I Zw 1	104.94 ± 22.77	480.98 ± 56.43	...
LB 2522	146.22 ± 66.85	76.92 ± 113.51	...
LEDA 51016	34.34 ± 12.19	304.85 ± 35.02	...
PHL 1092	20.55 ± 4.22	5.55 ± 2.69	...
Fairall 9	107.64 ± 26.10	362.78 ± 32.17	389.50 ± 69.99
Ark 120	220.37 ± 113.96	880.57 ± 154.66	500.72 ± 188.04
NGC 3783	403.76 ± 141.04	1013.02 ± 159.09	539.06 ± 145.03
TXS 0042+101	0.63 ± 1.10	3.40 ± 1.65	3.49 ± 3.31

Note. (1) Object common name. (2) Intensity of the line associated with the BLUE, with associated errors, measured in units of 10^{-15} erg s^{-1} cm^{-2} $Å^{-1}$. (3) Intensity of the line associated with the BC, with associated errors, measured in units of 10^{-15} erg s^{-1} cm^{-2} $Å^{-1}$. (4) Intensity of the line associated with the VBC, with associated errors, measured in units of 10^{-15} erg s^{-1} cm^{-2} $Å^{-1}$.

Table 3.2: CIV and HeII line measurements.

Object name		CIV			HeII	
	BLUE	BC	VBC	BLUE	BC	VBC
(1)	(2)	(3)	(4)	(5)	(6)	(7)
Mrk 335	24.88 ± 16.90	3942.84 ± 273.90	...	153.07 ± 33.22	453.63 ± 77.48	...
Mrk 110	68.24 ± 40.16	5526.12 ± 426.70	...	...	412.67 ± 99.00	...
Mrk 509	266.04 ± 130.47	11133.47 ± 993.72	...	394.09 ± 154.25	1096.06 ± 300.33	...
Mrk 478	212.57 ± 30.37	819.55 ± 100.13	...	124.03 ± 24.54	101.89 ± 35.06	...
Ark 564	29.46 ± 21.54	408.51 ± 53.91	...	42.14 ± 24.86	140.47 ± 30.34	...
Ton 28	203.13 ± 64.77	221.40 ± 87.62	...	63.95 ± 46.53	36.43 ± 62.66	...
I Zw 1	986.55 ± 96.97	678.23 ± 96.34	...	196.94 ± 47.21	143.27 ± 44.78	...
LB 2522	201.11 ± 83.38	87.57 ± 99.24	...	53.54 ± 59.76	31.84 ± 95.10	...
LEDA 51016	150.64 ± 24.71	446.39 ± 66.63	...	58.43 ± 17.11	42.50 ± 24.98	...
PHL 1092	18.93 ± 3.16	3.78 ± 2.06	...	2.29 ± 1.49	0.41 ± 1.61	...
Fairall 9	448.10 ± 84.16	2354.86 ± 185.25	1772.15 ± 294.60	14.67 ± 33.15	171.98 ± 58.79	127.32 ± 86.42
Ark 120	1499.94 ± 154.97	2500.38 ± 168.59	1002.33 ± 153.92	...	150.12 ± 47.74	400.80 ± 107.12
NGC 3783	2318.06 ± 281.97	8719.49 ± 533.94	6119.32 ± 866.88	85.56 ± 85.99	793.70 ± 174.59	2182.88 ± 569.74
TXS 0042+101	5.04 ± 1.58	18.68 ± 2.81	33.03 ± 6.93	...	1.49 ± 1.14	7.50 ± 4.19

Note. (1) Object common name. (2),(5) Intensity of the line associated with the BLUE, with associated errors, measured in units of 10^{-15} erg s^{-1} cm^{-2} Å^{-1}. (3),(6) Intensity of the line associated with the BC, with associated errors, measured in units of 10^{-15} erg s^{-1} cm^{-2} Å^{-1}. (4),(7) Intensity of the line associated with the VBC, with associated errors, measured in units of 10^{-15} erg s^{-1} cm^{-2} Å^{-1}.

Table 3.3: λ1900 blend line measurements.

Object name	AlIII		SiIII]		CIII]		
	BLUE	BC	BLUE	BC	BLUE	BC	VBC
(1)	(2)	(3)	(4)	(5)	(6)	(7)	(8)
Mrk 335	...	42.50 ± 45.93	...	186.12 ± 68.13	...	704.64 ± 124.94	...
Mrk 110	...	...	...	...	...	...	...
Mrk 509	...	460.00 ± 213.15	...	427.48 ± 211.70	...	2284.78 ± 414.81	...
Mrk 478	...	106.45 ± 26.09	...	205.03 ± 36.90	...	367.21 ± 54.57	...
Ark 564	...	14.63 ± 7.37	...	36.53 ± 10.45	...	231.33 ± 25.26	...
Ton 28	...	135.14 ± 80.57	...	84.83 ± 74.25	...	51.21 ± 51.80	...
I Zw 1	...	151.92 ± 32.59	...	250.21 ± 42.96	...	214.02 ± 44.65	...
LB 2522	...	60.23 ± 87.39	...	13.11 ± 89.42	...	85.74 ± 91.99	...
LEDA 51016	...	30.72 ± 13.22	...	74.79 ± 19.12	...	147.98 ± 29.83	...
PHL 1092	3.18 ± 1.33	7.79 ± 3.34	3.31 ± 1.37	7.87 ± 3.42	2.68 ± 1.22	1.00 ± 3.14	...
Fairall 9	...	156.17 ± 52.54	...	411.34 ± 78.67	...	448.15 ± 72.18	171.19 ± 68.13
Ark 120	...	115.90 ± 50.57	...	396.18 ± 81.82	...	456.50 ± 76.66	300.58 ± 93.15
NGC 3783	...	498.80 ± 150.70	...	661.48 ± 170.25	...	1159.87 ± 201.02	1023.66 ± 344.01
TXS 0042+101	...	2.07 ± 1.09	...	2.30 ± 1.15	...	5.39 ± 1.46	5.97 ± 3.00

Note. (1) Object common name. (2),(4),(6) Intensity of the line associated with the BLUE, with associated errors, measured in units of 10^{-15} erg s^{-1} cm^{-2} Å^{-1}. (3),(5),(7) Intensity of the line associated with the BC, with associated errors, measured in units of 10^{-15} erg s^{-1} cm^{-2} Å^{-1}. (8) Intensity of the line associated with the VBC, with associated errors, measured in units of 10^{-15} erg s^{-1} cm^{-2} Å^{-1}.

Table 3.4: Optical line measurements.

Object name	HeII$_{opt}$			Hβ		FeII
	BC	VBC	BLUE	BC	VBC	BC
(1)	(2)	(3)	(4)	(5)	(6)	(7)
Mrk 335	170.28 ± 32.16	...	...	680.45 ± 72.43	...	229.74 ± 31.04
Mrk 110	24.14 ± 4.26		...	146.54 ± 15.72	...	29.22 ± 5.64
Mrk 509	446.54 ± 91.51	...	...	1876.98 ± 229.78	...	38.62 ± 28.66
Mrk 478	5.35 ± 0.99	...	6.15 ± 1.53	157.27 ± 12.22	...	169.36 ± 10.02
Ark 564	10.18 ± 3.66	...	...	36.50 ± 6.39	...	24.28 ± 6.82
Ton 28	...	...	...	123.09 ± 17.10	...	128.38 ± 12.68
I Zw 1	...	...	137.23 ± 20.68	213.98 ± 26.44	...	610.66 ± 50.55
LB 2522	...	...	...	35.28 ± 7.79	...	45.74 ± 5.34
LEDA 51016	...	...	8.95 ± 1.73	59.89 ± 8.65	...	66.86 ± 6.38
PHL 1092	...	...	2.08 ± 0.66	11.71 ± 2.47	...	24.21 ± 2.72
Fairall 9	...	...	...	186.94 ± 20.68	239.11 ± 41.80	183.82 ± 23.58
Ark 120	...	153.93 ± 38.77	260.74 ± 25.80	809.21 ± 55.88	991.02 ± 102.97	1159.92 ± 86.17
NGC 3783	...	230.86 ± 54.88	...	1141.56 ± 72.82	521.23 ± 111.74	331.74 ± 56.27
TXS 0042+101	...	...	...	3.11 ± 1.06	8.81 ± 4.03	0.48 ± 0.73

Note. (1) Object common name. (2),(5),(7) Intensity of the line associated with the BC, with associated errors, measured in units of 10^{-15} erg s^{-1} cm^{-2} Å^{-1}. (3),(6) Intensity of the line associated with the VBC, with associated errors, measured in units of 10^{-15} erg s^{-1} cm^{-2} Å^{-1}. (4) Intensity of the line associated with the BLUE, with associated errors, measured in units of 10^{-15} erg s^{-1} cm^{-2} Å^{-1}.

The diagnostic ratios described in Section 2.5 have then been calculated with the associated errors, distinguishing between the different components of the BLUE, BC and VBC. A diagnostic ratio associated to all combined components (Total) is also reported.

Diagnostic ratios for all objects are reported in Tables from 3.5 to 3.18.

Table 3.5: Diagnostic ratios of Mrk 335.

Diagnostic ratio	BLUE	BC	VBC	Total
(1)	(2)	(3)	(4)	(5)
SiIV+OIV]/CIV	3.43 ± 2.54	0.16 ± 0.02	...	0.18 ± 0.02
SiIV+OIV]/HeII	0.56 ± 0.21	1.40 ± 0.29	...	1.19 ± 0.22
CIV/HeII	0.16 ± 0.12	8.69 ± 1.60	...	6.54 ± 1.07
CIV/Hβ	...	5.79 ± 0.74	...	5.83 ± 0.74
AlIII/CIV	...	0.01 ± 0.01	...	0.01 ± 0.01
AlIII/SiIII]	...	0.23 ± 0.26	...	0.23 ± 0.26
SiIII]/CIII]	...	0.26 ± 0.11	...	0.26 ± 0.11
CIII]/CIV	...	0.18 ± 0.03	...	0.18 ± 0.03
FeII/Hβ	...	0.34 ± 0.06	...	0.34 ± 0.06
$\mathrm{HeII_{opt}}$/Hβ	...	0.25 ± 0.05	...	0.25 ± 0.05

Note. (1) Diagnostic ratios used for the estimation of physical parameters. (2) Diagnostic ratio for the BLUE, with associated errors. (3) Diagnostic ratio for the BC, with associated errors. (4) Diagnostic ratio for the VBC, with associated errors. (5) Diagnostic ratio for the components combined, with associated errors.

Table 3.6: Diagnostic ratios of Mrk 110.

Diagnostic ratio	BLUE	BC	VBC	Total
(1)	(2)	(3)	(4)	(5)
SiIV+OIV]/CIV	...	0.13 ± 0.02	...	0.10 ± 0.02
SiIV+OIV]/HeII	...	1.71 ± 0.48	...	1.61 ± 0.46
CIV/HeII	...	13.39 ± 3.37	...	15.76 ± 4.07
CIV/Hβ	...	37.71 ± 4.98	...	44.56 ± 5.81
AlIII/CIV	...	...	...	...
AlIII/SiIII]	...	...	...	...
SiIII]/CIII]	...	...	...	...
CIII]/CIV	...	...	...	...
FeII/Hβ	...	0.20 ± 0.04	...	0.19 ± 0.04
$\mathrm{HeII_{opt}}$/Hβ	...	0.16 ± 0.03	...	0.16 ± 0.03

Note. (1) Diagnostic ratios used for the estimation of physical parameters. (2) Diagnostic ratio for the BLUE, with associated errors. (3) Diagnostic ratio for the BC, with associated errors. (4) Diagnostic ratio for the VBC, with associated errors. (5) Diagnostic ratio for the components combined, with associated errors.

Table 3.7: Diagnostic ratios of Mrk 509.

Diagnostic ratio	BLUE	BC	VBC	Total
(1)	(2)	(3)	(4)	(5)
SiIV+OIV]/CIV	0.95 ± 0.59	0.17 ± 0.03	...	0.19 ± 0.03
SiIV+OIV]/HeII	0.64 ± 0.35	1.70 ± 0.54	...	1.42 ± 0.39
CIV/HeII	0.68 ± 0.42	10.16 ± 2.93	...	7.65 ± 1.91
CIV/Hβ	...	5.05 ± 0.69	...	5.17 ± 0.71
AlIII/CIV	...	0.04 ± 0.02	...	0.04 ± 0.02
AlIII/SiIII]	...	1.08 ± 0.73	...	1.08 ± 0.73
SiIII]/CIII]	...	0.19 ± 0.10	...	0.19 ± 0.10
CIII]/CIV	...	0.21 ± 0.04	...	0.20 ± 0.04
FeII/Hβ	...	0.02 ± 0.02	...	0.02 ± 0.02
$\mathrm{HeII_{opt}}$/Hβ	...	0.24 ± 0.06	...	0.24 ± 0.06

Note. (1) Diagnostic ratios used for the estimation of physical parameters. (2) Diagnostic ratio for the BLUE, with associated errors. (3) Diagnostic ratio for the BC, with associated errors. (4) Diagnostic ratio for the VBC, with associated errors. (5) Diagnostic ratio for the components combined, with associated errors.

Table 3.8: Diagnostic ratios of Mrk 478.

Diagnostic ratio	BLUE	BC	VBC	Total
(1)	(2)	(3)	(4)	(5)
SiIV+OIV]/CIV	0.03 ± 0.11	0.66 ± 0.17	...	0.53 ± 0.13
SiIV+OIV]/HeII	0.06 ± 0.18	5.31 ± 2.18	...	2.42 ± 0.74
CIV/HeII	1.71 ± 0.42	8.04 ± 2.94	...	4.57 ± 1.06
CIV/Hβ	34.58 ± 9.93	5.21 ± 0.75	...	6.32 ± 0.83
AlIII/CIV	...	0.13 ± 0.04	...	0.10 ± 0.03
AlIII/SiIII]	...	0.52 ± 0.16	...	0.52 ± 0.16
SiIII]/CIII]	...	0.56 ± 0.13	...	0.56 ± 0.13
CIII]/CIV	...	0.45 ± 0.09	...	0.36 ± 0.07
FeII/Hβ	...	1.08 ± 0.11	...	1.04 ± 0.10
$\mathrm{HeII_{opt}}$/Hβ	...	0.03 ± 0.01	...	0.03 ± 0.01

Note. (1) Diagnostic ratios used for the estimation of physical parameters. (2) Diagnostic ratio for the BLUE, with associated errors. (3) Diagnostic ratio for the BC, with associated errors. (4) Diagnostic ratio for the VBC, with associated errors. (5) Diagnostic ratio for the components combined, with associated errors.

3.2 Estimation of metallicity

The metallicity is determined using a `SuperMongo` code (P. Marziani, private communication) that calculates the χ^2 using the diagnostic ratios obtained earlier for individual objects. For each object k and each component c, the χ^2 is computed with respect to the results of the `CLOUDY` simulations (expressed with the subscript "mod") as a function of

Table 3.9: Diagnostic ratios of Ark 564.

Diagnostic ratio	BLUE	BC	VBC	Total
(1)	(2)	(3)	(4)	(5)
SiIV+OIV]/CIV	0.39 ± 0.46	0.28 ± 0.07	...	0.29 ± 0.08
SiIV+OIV]/HeII	0.27 ± 0.30	0.82 ± 0.25	...	0.70 ± 0.23
CIV/HeII	0.70 ± 0.66	2.91 ± 0.74	...	2.40 ± 0.63
CIV/Hβ	...	9.42 ± 1.86	...	10.10 ± 2.03
AlIII/CIV	...	0.04 ± 0.02	...	0.03 ± 0.02
AlIII/SiIII]	...	0.40 ± 0.23	...	0.40 ± 0.23
SiIII]/CIII]	...	0.16 ± 0.05	...	0.16 ± 0.05
CIII]/CIV	...	0.57 ± 0.10	...	0.53 ± 0.09
FeII/Hβ	...	0.67 ± 0.22	...	0.67 ± 0.22
$\mathrm{HeII_{opt}}$/Hβ	...	0.28 ± 0.11	...	0.28 ± 0.11

Note. (1) Diagnostic ratios used for the estimation of physical parameters. (2) Diagnostic ratio for the BLUE, with associated errors. (3) Diagnostic ratio for the BC, with associated errors. (4) Diagnostic ratio for the VBC, with associated errors. (5) Diagnostic ratio for the components combined, with associated errors.

Table 3.10: Diagnostic ratios of Ton 28.

Diagnostic ratio	BLUE	BC	VBC	Total
(1)	(2)	(3)	(4)	(5)
SiIV+OIV]/CIV	0.31 ± 0.22	0.90 ± 0.72	...	0.62 ± 0.39
SiIV+OIV]/HeII	0.99 ± 0.96	5.47 ± 10.15	...	2.62 ± 2.45
CIV/HeII	3.18 ± 2.52	6.08 ± 10.72	...	4.23 ± 3.37
CIV/Hβ	...	1.80 ± 0.75	...	3.45 ± 1.08
AlIII/CIV	...	0.61 ± 0.44	...	0.32 ± 0.21
AlIII/SiIII]	...	1.59 ± 1.69	...	1.59 ± 1.69
SiIII]/CIII]	...	1.66 ± 2.22	...	1.66 ± 2.22
CIII]/CIV	...	0.23 ± 0.25	...	0.12 ± 0.13
FeII/Hβ	...	1.04 ± 0.18	...	1.04 ± 0.18
$\mathrm{HeII_{opt}}$/Hβ	...	...	...	...

Note. (1) Diagnostic ratios used for the estimation of physical parameters. (2) Diagnostic ratio for the BLUE, with associated errors. (3) Diagnostic ratio for the BC, with associated errors. (4) Diagnostic ratio for the VBC, with associated errors. (5) Diagnostic ratio for the components combined, with associated errors.

U, n_{H} and Z. This involves summing over the available diagnostic ratios, as expressed by the equation:

$$\chi^2_{\mathrm{kc}}(n_{\mathrm{H}}, U, Z) = \sum_{\mathrm{i}} w_{\mathrm{ci}} \left(\frac{R_{\mathrm{kci}} - R_{\mathrm{kci,mod}}(n_{\mathrm{H}}, U, Z)}{\delta R_{\mathrm{kci}}} \right)^2 . \tag{3.3}$$

Table 3.11: Diagnostic ratios of I Zw 1.

Diagnostic ratio	BLUE	BC	VBC	Total
(1)	(2)	(3)	(4)	(5)
SiIV+OIV]/CIV	0.11 ± 0.03	0.71 ± 0.13	...	0.35 ± 0.05
SiIV+OIV]/HeII	0.53 ± 0.17	3.36 ± 1.12	...	1.72 ± 0.42
CIV/HeII	5.01 ± 1.30	4.73 ± 1.63	...	4.89 ± 1.16
CIV/Hβ	7.19 ± 1.29	3.17 ± 0.60	...	4.74 ± 0.64
AlIII/CIV	...	0.22 ± 0.06	...	0.09 ± 0.02
AlIII/SiIII]	...	0.61 ± 0.17	...	0.61 ± 0.17
SiIII]/CIII]	...	1.17 ± 0.32	...	1.17 ± 0.32
CIII]/CIV	...	0.32 ± 0.08	...	0.13 ± 0.03
FeII/Hβ	...	2.85 ± 0.42	...	1.74 ± 0.23
$\mathrm{HeII_{opt}}$/Hβ	...	...	...	...

Note. (1) Diagnostic ratios used for the estimation of physical parameters. (2) Diagnostic ratio for the BLUE, with associated errors. (3) Diagnostic ratio for the BC, with associated errors. (4) Diagnostic ratio for the VBC, with associated errors. (5) Diagnostic ratio for the components combined, with associated errors.

Table 3.12: Diagnostic ratios of LB 2522.

Diagnostic ratio	BLUE	BC	VBC	Total
(1)	(2)	(3)	(4)	(5)
SiIV+OIV]/CIV	0.73 ± 0.45	1.78 ± 2.40	...	1.05 ± 0.59
SiIV+OIV]/HeII	2.73 ± 3.29	4.91 ± 15.08	...	3.54 ± 3.97
CIV/HeII	3.76 ± 4.47	2.75 ± 8.79	...	3.38 ± 3.76
CIV/Hβ	...	2.48 ± 2.87	...	8.18 ± 3.63
AlIII/CIV	...	0.69 ± 1.27	...	0.21 ± 0.31
AlIII/SiIII]	...	4.59 ± 32.04	...	4.59 ± 32.04
SiIII]/CIII]	...	0.15 ± 1.06	...	0.15 ± 1.06
CIII]/CIV	...	0.98 ± 1.53	...	0.30 ± 0.34
FeII/Hβ	...	1.30 ± 0.32	...	1.30 ± 0.32
$\mathrm{HeII_{opt}}$/Hβ	...	...	...	...

Note. (1) Diagnostic ratios used for the estimation of physical parameters. (2) Diagnostic ratio for the BLUE, with associated errors. (3) Diagnostic ratio for the BC, with associated errors. (4) Diagnostic ratio for the VBC, with associated errors. (5) Diagnostic ratio for the components combined, with associated errors.

Here, w_{ci} represents weights assigned to each diagnostic ratio to account for their importance and the degree of uncertainty in the computation. All weights in this computation have been set to 1. R_{kc} identifies the diagnostic ratio considered for the object and component and δR_{kc} identifies the error associated to each component.

The inclusion of more diagnostic ratios in the computation improves accuracy by increasing the number of degrees of freedom in the system. However, not all objects have the

Table 3.13: Diagnostic ratios of LEDA 51016.

Diagnostic ratio	BLUE	BC	VBC	Total
(1)	(2)	(3)	(4)	(5)
SiIV+OIV]/CIV	0.23 ± 0.09	0.68 ± 0.13	...	0.57 ± 0.10
SiIV+OIV]/HeII	0.59 ± 0.27	7.17 ± 4.30	...	3.36 ± 1.00
CIV/HeII	2.58 ± 0.87	10.50 ± 6.37	...	5.92 ± 1.78
CIV/Hβ	16.84 ± 4.27	7.45 ± 1.55	...	8.67 ± 1.57
AlIII/CIV	...	0.07 ± 0.03	...	0.05 ± 0.02
AlIII/SiIII]	...	0.41 ± 0.21	...	0.41 ± 0.21
SiIII]/CIII]	...	0.51 ± 0.16	...	0.51 ± 0.16
CIII]/CIV	...	0.33 ± 0.08	...	0.25 ± 0.06
FeII/Hβ	...	1.12 ± 0.19	...	0.97 ± 0.16
$\mathrm{HeII_{opt}}$/Hβ	...	...	...	...

Note. (1) Diagnostic ratios used for the estimation of physical parameters. (2) Diagnostic ratio for the BLUE, with associated errors. (3) Diagnostic ratio for the BC, with associated errors. (4) Diagnostic ratio for the VBC, with associated errors. (5) Diagnostic ratio for the components combined, with associated errors.

Table 3.14: Diagnostic ratios of PHL 1092.

Diagnostic ratio	BLUE	BC	VBC	Total
(1)	(2)	(3)	(4)	(5)
SiIV+OIV]/CIV	1.09 ± 0.29	1.47 ± 1.07	...	1.15 ± 0.30
SiIV+OIV]/HeII	8.96 ± 6.13	13.60 ± 54.11	...	9.67 ± 6.95
CIV/HeII	8.26 ± 5.56	9.27 ± 36.94	...	8.41 ± 6.00
CIV/Hβ	9.10 ± 3.27	0.32 ± 0.19	...	1.65 ± 0.43
AlIII/CIV	0.17 ± 0.08	2.06 ± 1.43	...	0.48 ± 0.19
AlIII/SiIII]	0.96 ± 0.56	0.99 ± 0.60	...	0.98 ± 0.48
SiIII]/CIII]	1.24 ± 0.76	7.84 ± 24.72	...	3.04 ± 2.03
CIII]/CIV	0.14 ± 0.07	0.27 ± 0.84	...	0.16 ± 0.10
FeII/Hβ	...	2.07 ± 0.49	...	1.76 ± 0.39
$\mathrm{HeII_{opt}}$/Hβ	...	...	...	...

Note. (1) Diagnostic ratios used for the estimation of physical parameters. (2) Diagnostic ratio for the BLUE, with associated errors. (3) Diagnostic ratio for the BC, with associated errors. (4) Diagnostic ratio for the VBC, with associated errors. (5) Diagnostic ratio for the components combined, with associated errors.

same number of measured line intensities and diagnostic ratios, either because they are not present or because their intensity measurements are highly uncertain. This is particularly true for the CIV/Hβ ratio, which is uncertain due to the non-contemporary nature of our spectra. To address this, the CIV/Hβ ratio was considered for the estimation of metallicity only when the intrinsic variability of the objects was deemed negligible, and it could be affirmed that the intensity of CIV and Hβ did not suffer contaminations from other line components.

Table 3.15: Diagnostic ratios of Fairall 9.

Diagnostic ratio	BLUE	BC	VBC	Total
(1)	(2)	(3)	(4)	(5)
SiIV+OIV]/CIV	0.24 ± 0.07	0.15 ± 0.02	0.17 ± 0.03	0.19 ± 0.03
SiIV+OIV]/HeII	7.34 ± 16.69	2.11 ± 0.75	3.06 ± 2.15	2.74 ± 0.98
CIV/HeII	30.55 ± 69.31	13.69 ± 4.80	13.92 ± 9.73	14.57 ± 5.11
CIV/Hβ	...	12.60 ± 1.71	7.41 ± 1.79	10.74 ± 1.64
AlIII/CIV	...	0.07 ± 0.02	...	0.03 ± 0.01
AlIII/SiIII]	...	0.38 ± 0.15	...	0.38 ± 0.15
SiIII]/CIII]	...	0.92 ± 0.23	...	0.66 ± 0.17
CIII]/CIV	...	0.19 ± 0.03	0.10 ± 0.04	0.14 ± 0.03
FeII/Hβ	...	0.98 ± 0.17	...	0.43 ± 0.08
$\mathrm{HeII_{opt}}$/Hβ	...	...	...	...

Note. (1) Diagnostic ratios used for the estimation of physical parameters. (2) Diagnostic ratio for the BLUE, with associated errors. (3) Diagnostic ratio for the BC, with associated errors. (4) Diagnostic ratio for the VBC, with associated errors. (5) Diagnostic ratio for the components combined, with associated errors.

Table 3.16: Diagnostic ratios of Ark 120.

Diagnostic ratio	BLUE	BC	VBC	Total
(1)	(2)	(3)	(4)	(5)
SiIV+OIV]/CIV	0.15 ± 0.08	0.35 ± 0.07	0.50 ± 0.20	0.32 ± 0.07
SiIV+OIV]/HeII	...	5.87 ± 2.13	1.25 ± 0.58	2.88 ± 0.87
CIV/HeII	...	16.66 ± 5.41	2.50 ± 0.77	9.00 ± 2.17
CIV/Hβ	5.75 ± 0.82	2.24 ± 0.20	1.01 ± 0.19	2.11 ± 0.21
AlIII/CIV	...	0.05 ± 0.02	...	0.02 ± 0.01
AlIII/SiIII]	...	0.29 ± 0.14	...	0.29 ± 0.14
SiIII]/CIII]	...	0.87 ± 0.23	...	0.52 ± 0.14
CIII]/CIV	...	0.18 ± 0.03	0.30 ± 0.10	0.15 ± 0.03
FeII/Hβ	...	1.04 ± 0.10	...	0.49 ± 0.04
$\mathrm{HeII_{opt}}$/Hβ	...	...	0.16 ± 0.04	0.07 ± 0.02

Note. (1) Diagnostic ratios used for the estimation of physical parameters. (2) Diagnostic ratio for the BLUE, with associated errors. (3) Diagnostic ratio for the BC, with associated errors. (4) Diagnostic ratio for the VBC, with associated errors. (5) Diagnostic ratio for the components combined, with associated errors.

The computation is carried out for the BC of all objects in the sample, for the VBC of Population B quasars, and for the BLUE of PHL 1092 alone among xA Quasars. Indeed PHL 1092, being the most extreme xA Quasar in the sample, displays blueshifted components in its lines that allowed for more effective intensity measurement compared to other xA Quasars, thereby increasing the number of diagnostic ratios available for the estimation of metallicity in the BLUE.

Table 3.17: Diagnostic ratios of NGC 3783.

Diagnostic ratio	BLUE	BC	VBC	Total
(1)	(2)	(3)	(4)	(5)
SiIV+OIV]/CIV	0.17 ± 0.06	0.12 ± 0.02	0.06 ± 0.02	0.11 ± 0.02
SiIV+OIV]/HeII	4.72 ± 5.02	1.28 ± 0.34	0.25 ± 0.09	0.64 ± 0.18
CIV/HeII	27.09 ± 27.43	10.99 ± 2.51	2.80 ± 0.83	5.60 ± 1.28
CIV/Hβ	...	7.64 ± 0.68	11.74 ± 3.02	10.32 ± 1.33
AlIII/CIV	...	0.06 ± 0.02	...	0.03 ± 0.01
AlIII/SiIII]	...	0.75 ± 0.30	...	0.75 ± 0.30
SiIII]/CIII]	...	0.57 ± 0.18	...	0.30 ± 0.10
CIII]/CIV	...	0.13 ± 0.02	0.12 ± 0.04	0.13 ± 0.03
FeII/Hβ	...	0.29 ± 0.05	...	0.20 ± 0.04
HeII$_{\rm opt}$/Hβ	...	...	0.44 ± 0.14	0.14 ± 0.04

Note. (1) Diagnostic ratios used for the estimation of physical parameters. (2) Diagnostic ratio for the BLUE, with associated errors. (3) Diagnostic ratio for the BC, with associated errors. (4) Diagnostic ratio for the VBC, with associated errors. (5) Diagnostic ratio for the components combined, with associated errors.

Table 3.18: Diagnostic ratios of TXS 0042+101.

Diagnostic ratio	BLUE	BC	VBC	Total
(1)	(2)	(3)	(4)	(5)
SiIV+OIV]/CIV	0.12 ± 0.22	0.18 ± 0.09	0.19 ± 0.18	0.13 ± 0.07
SiIV+OIV]/HeII	...	2.29 ± 2.07	0.46 ± 0.51	0.84 ± 0.61
CIV/HeII	...	12.56 ± 9.78	4.40 ± 2.63	6.31 ± 3.16
CIV/Hβ	...	6.01 ± 2.24	3.75 ± 1.89	4.76 ± 1.80
AlIII/CIV	...	0.11 ± 0.06	...	0.04 ± 0.02
AlIII/SiIII]	...	0.90 ± 0.66	...	0.90 ± 0.66
SiIII]/CIII]	...	0.43 ± 0.24	...	0.20 ± 0.12
CIII]/CIV	...	0.29 ± 0.09	0.32 ± 0.17	0.20 ± 0.07
FeII/Hβ	...	0.16 ± 0.24	...	0.04 ± 0.06
HeII$_{\rm opt}$/Hβ	...	...	...	...

Note. (1) Diagnostic ratios used for the estimation of physical parameters. (2) Diagnostic ratio for the BLUE, with associated errors. (3) Diagnostic ratio for the BC, with associated errors. (4) Diagnostic ratio for the VBC, with associated errors. (5) Diagnostic ratio for the components combined, with associated errors.

The results of the computation for each object are shown in Table 3.19, displaying the metallicity, density and ionization parameter associated with the minimum χ^2, along with the parameter ranges within which it varies with 1σ accuracy.

Table 3.19: Metallicity and physical parameter estimates along the Quasar MS

Object	Component	Minimum χ^2	$\log U$	$\Delta \log U$	$\log Z$ $[Z_\odot]$	$\Delta \log Z$ $[Z_\odot]$	$\log n_\mathrm{H}$ $[\mathrm{cm}^{-3}]$	$\Delta \log n_\mathrm{H}$ $[\mathrm{cm}^{-3}]$
(1)	(2)	(3)	(4)	(5)	(6)	(7)	(8)	(9)
Mrk 335	BC	7.20	−1.50	−1.50 - −1.50	0.00	0.00 - 0.00	7.00	7.00 - 7.00
Mrk 110	BC	11.62	−1.00	−1.50 - −0.25	0.00	0.00 - 0.30	8.75	7.50 - 9.25
Mrk 509	BC	6.99	−0.50	−0.75 - −0.50	0.00	0.00 - 0.00	9.75	9.75 - 10.00
Mrk 478	BC	25.75	−1.00	−1.25 - −0.75	1.30	1.00 - 1.30	11.00	10.50 - 11.25
Ark 564	BC	29.92	−1.25	−1.75 - −0.25	0.70	0.30 - 1.00	7.00	7.00 - 10.00
Ton 28	BC	1.05	−0.75	−1.75 - −0.75	1.30	1.30 - 1.30	11.25	11.25 - 13.50
I Zw 1	BC	74.78	−2.25	−2.75 - −0.50	1.30	−2.00 - 2.00	10.25	7.00 - 11.00
LB 2522	BC	3.79	−0.50	−2.50 - −0.25	1.30	1.00 - 2.30	7.00	7.00 - 9.75
LEDA 51016	BC	23.78	−1.00	−1.50 - −0.75	1.30	0.70 - 1.70	10.25	10.00 - 10.50
PHL 1092	BC	2.93	−0.75	−2.25 - 0.00	1.70	1.30 - 2.30	11.25	11.00 - 12.75
PHL 1092	BLUE	1.78	−1.00	−1.50 - −0.75	1.30	1.00 - 1.70	11.50	11.25 - 12.00
Fairall 9	BC	37.30	−1.75	−2.00 - −0.75	0.30	−1.00 - 1.00	9.75	7.75 - 10.75
Fairall 9	VBC	0.51	−2.00	−2.00 - −2.00	0.00	0.00 - 0.30	10.50	10.00 - 10.75
Ark 120	BC	29.76	−1.50	−1.75 - −1.00	1.00	0.00 - 1.00	11.25	8.50 - 11.50
Ark 120	VBC	3.30	−2.75	−3.00 - −2.00	0.70	−1.30 - 1.30	12.00	7.75 - 13.00
NGC 3783	BC	27.05	−2.00	−2.00 - −1.50	−0.30	−1.30 - 0.30	9.50	7.50 - 10.00
NGC 3783	VBC	2.04	0.00	−1.75 - 0.00	−0.30	−1.30 - 0.00	9.50	9.00 - 11.50
TXS 0042+101	BC	4.99	−2.00	−2.25 - −1.00	−0.30	−1.30 - 0.70	9.75	7.50 - 10.00
TXS 0042+101	VBC	0.39	−2.00	−2.00 - −1.75	−1.30	−1.30 - −1.00	9.00	7.50 - 9.50

Note. (1) Object common name. (2) Component measured. (3) Minimum χ^2 associated with the object and the component. (4) Decimal logarithm of the ionization parameter U associated to the minimum χ^2. (5) Logarithmic interval associated to the variation of the ionization parameter U. (6) Decimal logarithm of the metallicity Z associated to the minimum χ^2. (7) Logarithmic interval associated to the variation of the metallicity Z. (8) Decimal logarithm of the Hydrogen density n_H associated to the minimum χ^2. (9) Logarithmic interval associated to the variation of the Hydrogen density n_H.

The computed metallicity varies widely among the objects of the sample, spanning from 0.5 $Z_\odot$ for TXS 0042+101 to 50 $Z_\odot$ associated to the minimum χ^2 of the BC of PHL 1092. Remarkably, these two objects are located at opposite ends of the MS, suggesting to the possibility of a gradient of metallicity along the Quasar MS: RL Population B objects with the lowest metallicity, and extreme-accreting Quasars exhibiting the highest.

Two-dimensional projections of the n_H - U, n_H - Z and U - Z planes are illustrated in Figures from 3.1 to 3.14.

From the 2D projections and the minimum χ^2 values presented in Table 3.19 it is evident that while the results for the physical parameters are well determined for some objects, for others they are not. The primary reason for this lies in the uncertainties tied to the measurement of the line intensities, as discussed before for the case of CIV/Hβ. However, this uncertainty extends to other lines as well.

Spectral type A1 and A2 objects exhibit solar metallicities, compatible with their weak AlIII and FeII emissions. At 1σ accuracy, the metallicity of most Population A objects is well constrained, with the exception of Mrk 110, I Zw 1 and PHL 1092.

Mrk 110 is poorly constrained due to the absence of its CIII] spectrum, depriving us of important diagnostic ratios such as CIII]/CIV, SiIII]/CIII] and AlIII/SiIII], crucial for metallicity and density determinations. Nevertheless, the metallicity and physical parameters obtained for Mrk 110, coupled with its spectral similarity to Mrk 335, show that the two objects position themselves in a similar manner in the parameter space, both showing solar metallicity.

Uncertainties in the measurement of the intensity of CIII] are likely the reason for the completely unconstrained metallicity of I Zw 1, too. The CIII] emission of I Zw 1 is affected by a strong absorption feature, making it challenging to precisely determine the line's intensity. Moreover, CIII], especially in the case of xA Quasars, blends with the FeIII]λ1914 feature, further complicating the precise determination of the intensity of CIII]. Such a high CIII]/CIV ratio is not compatible with the photoionization simulations at present, imposing density conditions that are non-physical, and rendering almost any value of Z and U feasible.

PHL 1092 encounters a similar challenge, coupled with the fact that its CIV emission is affected by absorption, and the differentiation between the BLUE and the BC of lines is not clear-cut. This results in large errors in the measurement, amplifying the degree of uncertainty in the physical parameters following the computation. Consequently, the metallicity of the BC of PHL 1092 is unconstrained. Conversely, the physical parameters associated to the BLUE are well-constrained, displaying a very low χ^2, resulting in a narrow range of variability at 1σ. The results for the BLUE are consistent with a region characterized by outflows and with similar metallicity to that of the BC.

Other objects show a growing trend in metallicity along the MS, with RL Population B objects exhibiting sub-solar metallicity, and extreme-accreting objects displaying super-solar metallicity. The sole exception to this trend is Ark 120. Ark 120, as previously discussed in Section 2.1, is a peculiar object with interesting properties, including the double peak of the Hβ emission. The metallicity associated with its BC is relatively constrained, reaching solar values. This aligns with its measured diagnostic ratios, as its strong FeII emission is peculiar for a Population B object. However, such intense FeII emission can only be linked with higher metallicity than the usual for Population B objects. Due to the limited number of diagnostic ratios associated with the VBC, the

VBC of Ark 120 occupies a large portion of the parameter space. Although unconstrained, the metallicity values obtained for the VBC are compatible with those for the BC, even though its ionization parameter is anomalous. Indeed, the VBC, closer to the black hole, should have much higher values of the ionization parameter U. This aspect requires further investigation, potentially using more diagnostic ratios or excluding some that might have been inaccurately measured.

Fairall 9, NGC 3783 and TXS 0042+101 exhibit lower metallicities, albeit with significant variations. Indeed, as we said before, there are substantial uncertainties in the measurement of the line intensities, particularly for TXS 0042+101, due to the low quality of the optical spectrum. The metallicity of the VBC is compatible with the metallicity found in the BC of these objects; however, no further assumptions could be made regarding the other physical parameters due to the low number of diagnostic ratios involved.

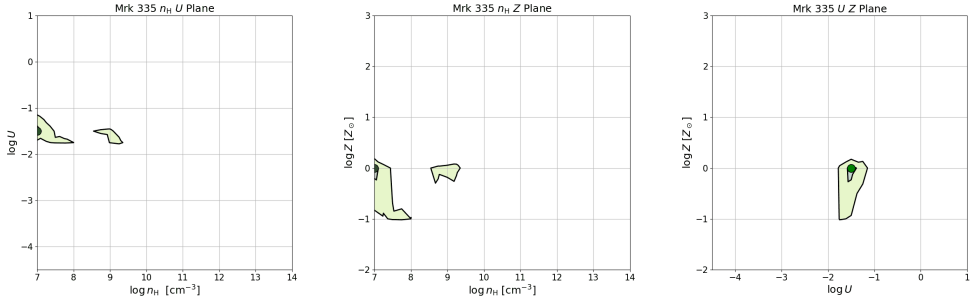

Figure 3.1: Two-dimensional parameter spaces illustrating the physical conditions of the gas surrounding Mrk 335. Each plot represents the BC with a green dot indicating the minimum χ^2 computed between measured diagnostic ratios and `CLOUDY` simulations. The darker green region corresponds to 1σ accuracy, while a lighter green shade indicates the 90% accuracy. Blue and red dots and shades represent the minimum χ^2 and associated regions for the BLUE and VBC, respectively. *Left*: Logarithmic plane of density and ionization parameter. *Middle*: Logarithmic plane of density and metallicity. *Right*: Logarithmic plane of ionization parameter and metallicity.

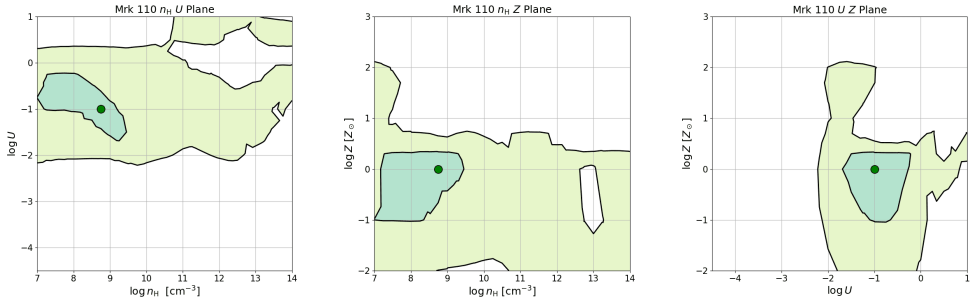

Figure 3.2: Same as in Figure 3.1, but for Mrk 110.

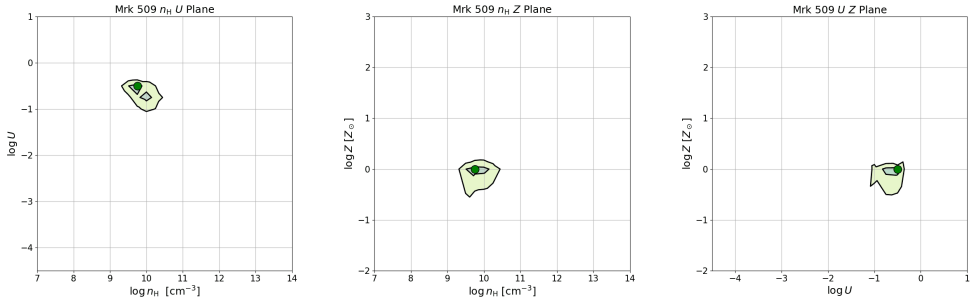

Figure 3.3: Same as in Figure 3.1, but for Mrk 509.

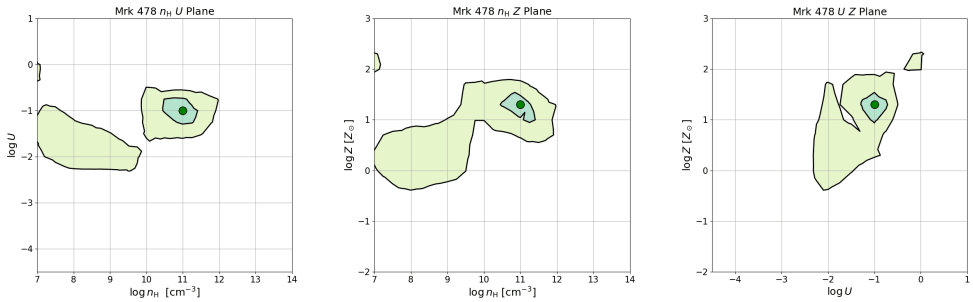

Figure 3.4: Same as in Figure 3.1, but for Mrk 478.

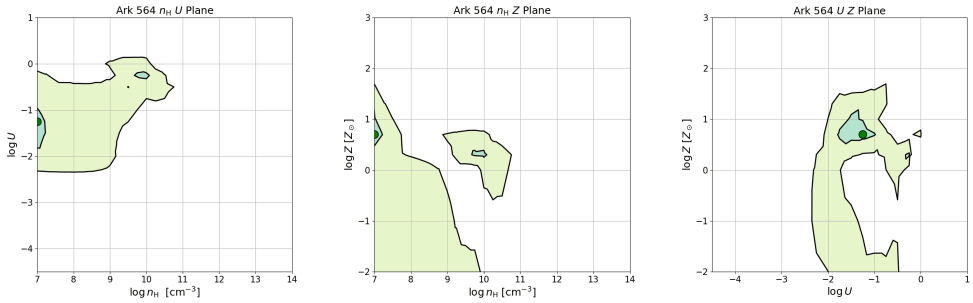

Figure 3.5: Same as in Figure 3.1, but for Ark 564.

3.3 Inferences on physical parameters

The physical parameters U and n_{H} are typically more constrained than metallicity because of our choice of diagnostic ratios, sensitive to density and ionization parameter.

However, in general, the objects that have a well-constrained metallicity follow in the trend of having well-constrained physical parameters. This is indeed because the determination of the physical conditions relies on precise measurements of the line intensities, and if a diagnostic ratio is not compatible with the others, the results require extreme physical conditions that may not be compatible with appropriate values of metallicity

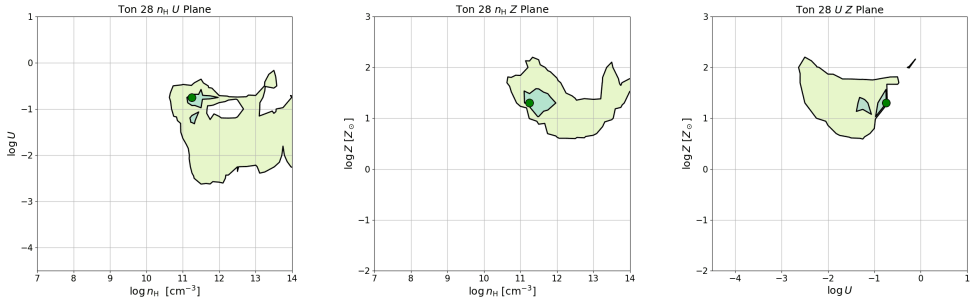

Figure 3.6: Same as in Figure 3.1, but for Ton 28.

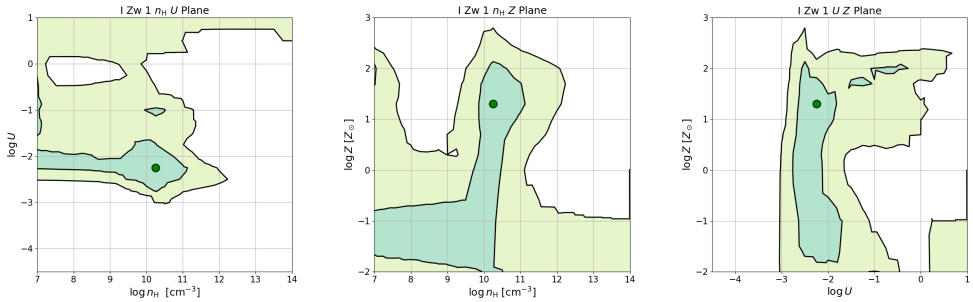

Figure 3.7: Same as in Figure 3.1, but for I Zw 1.

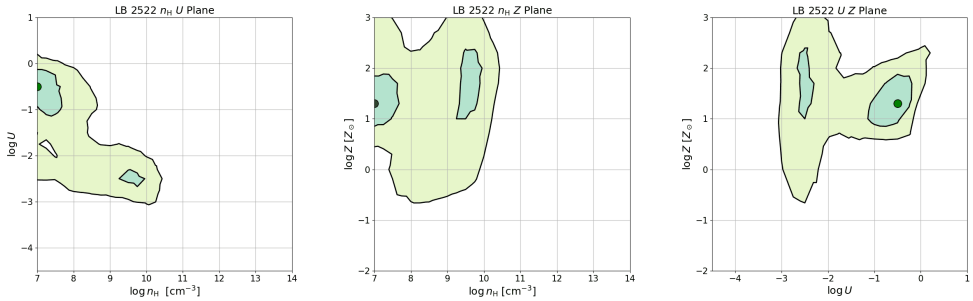

Figure 3.8: Same as in Figure 3.1, but for LB 2522.

and physical parameters.

As mentioned before, even though the properties of the VBC are not very well constrained for Population B Quasars, the case of NGC 3783 is of note. Indeed, the VBC is well-constrained, and in particular the ionization parameter, that is higher with respect to the one associated with the BC. In general, it is expected that the VBC of Population B objects, being in closer proximity to the ionizing source, would exhibit higher degrees of ionization, while the BLUE, situated further away from the ionizing source, is expected to be coupled with a lower ionization degree.

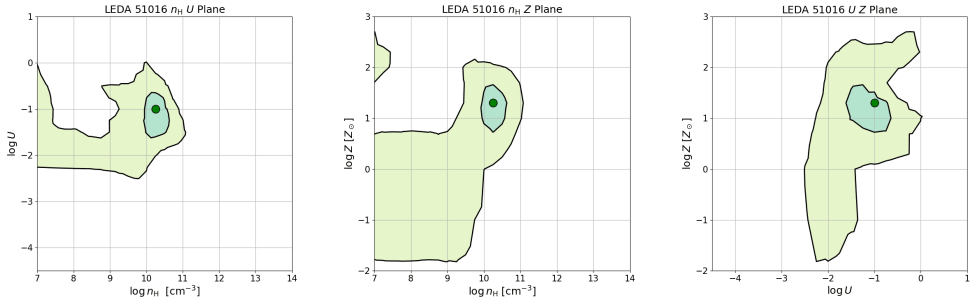

Figure 3.9: Same as in Figure 3.1, but for LEDA 51016.

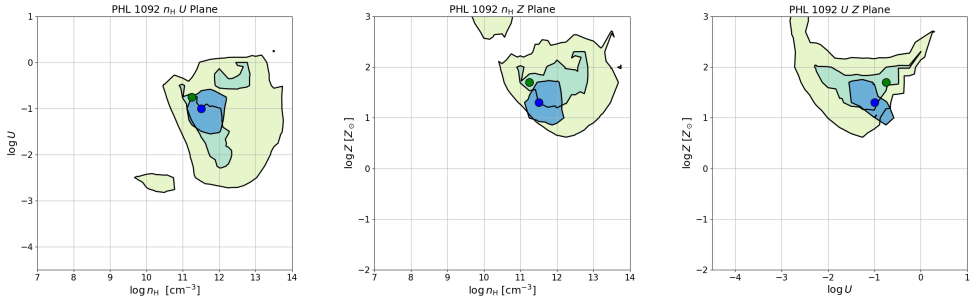

Figure 3.10: Same as in Figure 3.1, but for PHL 1092.

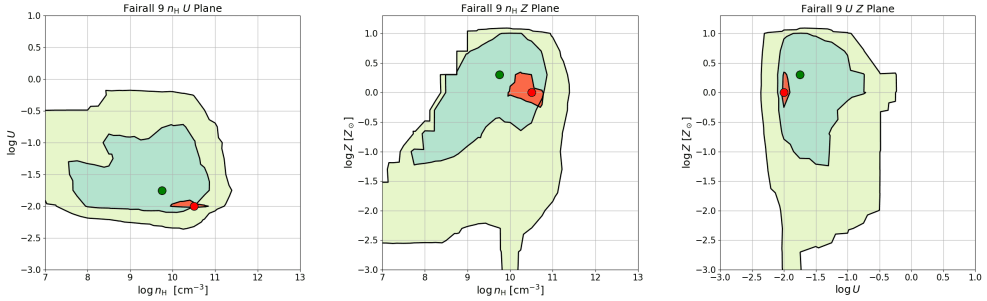

Figure 3.11: Same as in Figure 3.1, but for Fairall 9.

3.4 Chemical enrichment along the Eigenvector 1

In Figure 3.15 the position of the objects of our sample in the Eigenvector 1 parameter space is displayed, with the size of the markers displaying the minimum χ^2 metallicity of the objects. From this figure it is indeed clear that the metallicity is sub-solar for two of the Population B objects, is solar for spectral type A1 and A2 objects, and is super-solar for extreme-accretors, reaching extreme values up to 50 $Z_\odot$.

Correlations among physical parameters provide valuable insights into the relationships between different physical processes. The plots in Figure 3.16 employ linear regression to

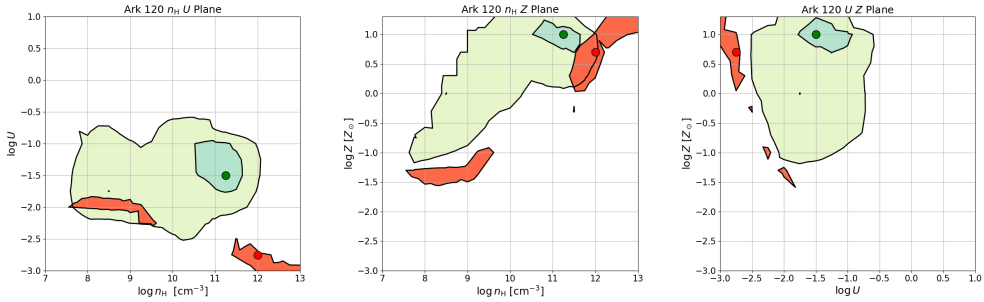

Figure 3.12: Same as in Figure 3.1, but for Ark 120.

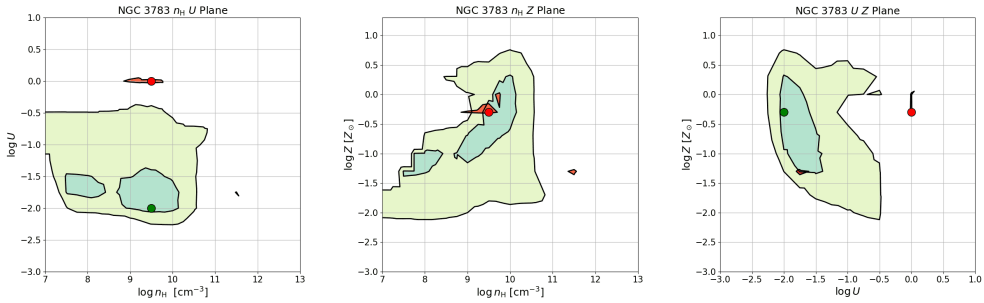

Figure 3.13: Same as in Figure 3.1, but for NGC 3783.

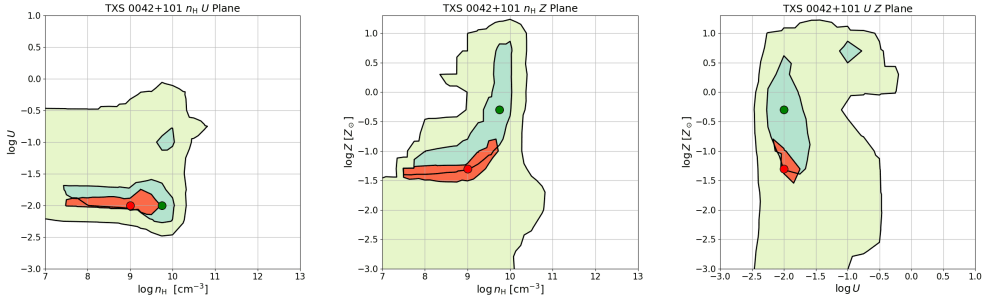

Figure 3.14: Same as in Figure 3.1, but for TXS 0042+101.

study the correlations among R_{FeII}, $\log Z$, $\log L/L_{Edd}$, $\log M_{BH}$ and $\log L_{bol}$. The slopes of the linear regression lines are computed using the `Fortran` code described in Feigelson & Babu (1992). In Table 3.20 are described the results of these correlations, as well as their statistical significance.

Notably, R_{FeII} exhibits a robust correlation with metallicity. This correlation is expected, given that the FeII/Hβ diagnostic ratio, used in determining the physical properties of the BLR gas, introduces a dependency between these parameters. To address potential bias, further investigation could involve examining changes in metallicity without considering this diagnostic ratio. Nevertheless, this result underscores the fact that the Quasar

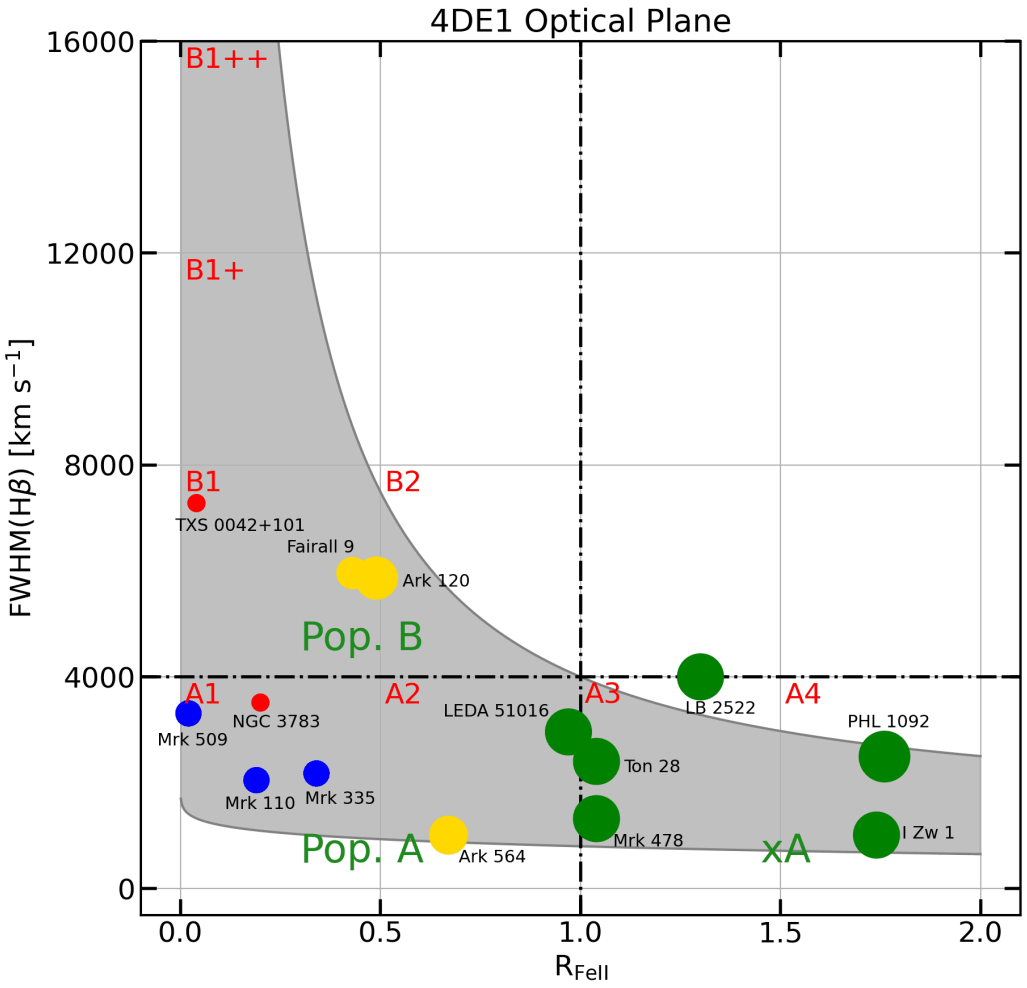

Figure 3.15: 4DE1 parameter space representation of our sample. Every object is placed according to its R_{FeII} and FWHM(Hβ). The size of each marker is proportional to the metallicity Z of the object it represents associated to the minimum χ^2 of our results. Objects with sub-solar metallicity are marked in red, objects with solar metallicity in blue, objects with metallicity $1Z_\odot < Z \leq 10Z_\odot$ are marked in gold, and objects with metallicity greater than 10 $Z_\odot$ are marked in green.

MS is a powerful tool capable of distinguishing various objects with diverse underlying characteristics using just two simple parameters.

Additionally, R_{FeII} demonstrates a significant correlation with the logarithm of the Eddington ratio, supporting the hypothesis that extreme accretors are associated with higher R_{FeII}. Despite only one xA object in the sample being assumed to be Super-Eddington,

the trend is apparent, with xA objects consistently showing a larger Eddington ratio. Once again, this result confirms the solidity of the Quasar MS, confirming the presence of these correlations observed in several other samples of Quasars.

The $\log L/L_{\rm Edd}$ is also found to correlate with $\log Z$, emphasizing the fact that extreme-accretors are characterized by the highest metallicities in the sample.

The logarithm of the bolometric luminosity $\log L_{\rm bol}$ is found to correlate, albeit less strongly than the previously discussed parameters, with $R_{\rm FeII}$ and $\log Z$. This weaker correlation evidences the fact that the bolometric luminosity is not a suitable parameter for estimating the metallicity in the surrounding regions of an AGN, as metallicity is more affected by accretion parameters.

Interestingly, black hole mass and metallicity are found to not correlate. Indeed, the objects span a wide range of masses, and their spectral types do not exhibit a clear trend in these correlations. This complexity highlights the diversity among objects in the sample and underscores the secondary role of the SMBH mass in defining the environment surrounding the black hole, with this role being relegated to the influence of stellar populations.

In summary, the first three correlations presented in Table 3.20 are very strong, reaching a significance exceeding 3σ with a sample size of just 14 objects. This indicates a robust and generally strong correlation. In contrast, the other correlations are found to be weaker, notably with the $\log M_{\rm BH}$ - $\log Z$ correlation falling below the 1σ confidence level.

Table 3.20: Parameter correlation

Correlation (1)	Correlation coefficient (2)	Significance (3)
$R_{\rm FeII}$ - $\log Z$	0.86	0.001
$R_{\rm FeII}$ - $\log L/L_{\rm Edd}$	0.65	0.015
$\log L/L_{\rm Edd}$ - $\log Z$	0.62	0.020
$\log M_{\rm BH}$ - $\log Z$	-0.08	0.766
$\log L_{\rm bol}$ - $\log Z$	0.43	0.107
$R_{\rm FeII}$ - $\log L_{\rm bol}$	0.54	0.043

Note. (1) Parameters between which the linear correlation is verified. (2) Correlation coefficient $c_{\rm corr}$ between the two parameters, obtained using the `Fortran` program described in Feigelson & Babu (1992). (3) Statistical significance defined as the complementary error function $erfc(x) = \frac{2}{\sqrt{\pi}} \int_x^\infty e^{-t^2}\, dt$ from Press et al. (1986), where x is defined as $x = \sqrt{\frac{N}{2}}|c_{\rm corr}|$ with N as the number of objects

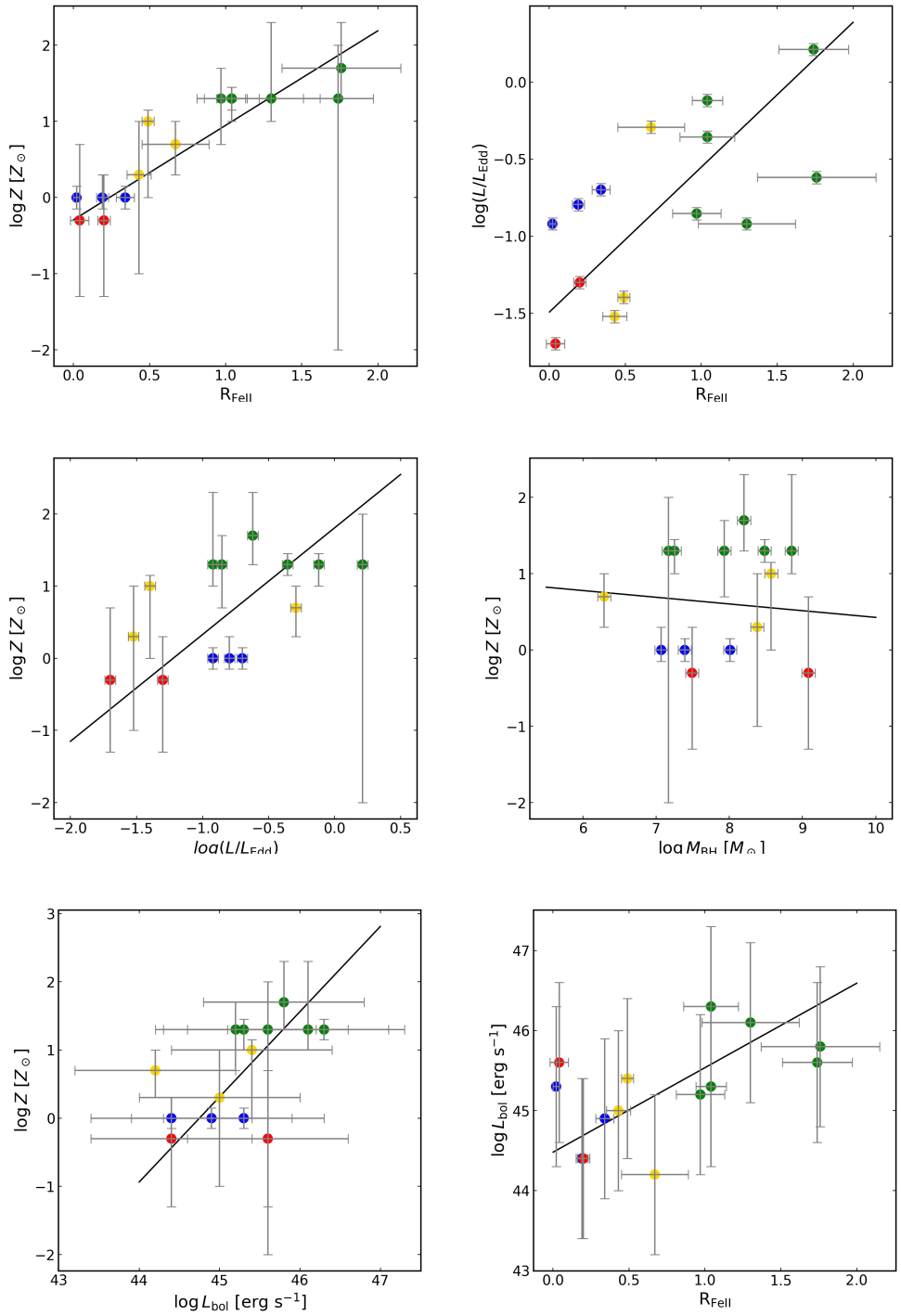

Figure 3.16: Plots describing the correlations of physical parameters in the selected sample. Each data point is depicted with the color that describes the metallicity of the object, as in Figure 3.15. Error bars are displayed in grey, while the linear regression line is shown in black. *Top left*: Correlation between R_{FeII} and $\log Z$. *Top right*: Correlation between R_{FeII} and the logarithm of the Eddington ratio. *Middle left*: Correlation between the logarithm of the Eddington ratio and $\log Z$. *Middle right*: Correlation between the logarithm of the black hole mass and $\log Z$. *Bottom left*: Correlation between the logarithm of the bolometric luminosity and $\log Z$. *Bottom right*: Correlation between R_{FeII} and the logarithm of the bolometric luminosity.

Chapter 4

Discussions

In this chapter the results of our measurements are discussed, contextualizing them with related studies. In Section 4.1 are evidenced the properties of the metal poor gas that characterizes the BLR of Population B objects. Section 4.2 delves into the presence of highly enriched gas in the BLR of xA Quasars. Section 4.3 examines the implications of our findings on feedback and galaxy evolution.

4.1 Metal poor BLR gas

Setting aside the peculiar case of Ark 120, the metallicity derived for the virialized component of Population B Quasars in the sample goes from 0.5 $Z_{\odot}$ to approximately solar metallicity. Population A Quasars which do not belong to the extreme-accreting class follow with about 1 $Z_{\odot}$.

These findings are consistent with results obtained in previous studies, including Punsly et al. (2018), Panda et al. (2019) and Marziani, Floris et al., (2023, submitted), for both individual objects and composite spectra representing different RL and RQ AGNs (Marziani et al., 2022).

Another notable distinction observed among these objects is the one between RL and RQ objects. Indeed, as it is shown, powerful Population B radio emitters also exhibit systematically lower metallicities with respect to their RQ counterparts. This was verified both in our sample, with TXS 0042+101 being the object with the lowest estimated metallicity of the sample, and in NGC 1275 in Punsly et al. (2018) and Marziani, Floris et al., (2023, submitted).

The gas present in the BLR of RL objects is found to be less enriched than the gas in the BLR of RQ Population B objects. It is noteworthy that both RL and RQ objects exhibit lower metallicity compared to xA objects.

4.2 Highly super-solar metallicity in xA Quasars

The derived Z values for the virialized component of xA Quasars of the sample indicate metallicities 10 to 50 times higher than solar values. These findings align with results

from previous studies on other samples of extreme-accreting Quasars, such as those by Śniegowska et al. (2021) and Garnica et al. (2022). The consistency in results can be attributed not only to the similarity in techniques but also to the similar samples employed.

Despite the astrophysical consistency and the robustness of the employed technique, it is essential to acknowledge the fact that these metallicity values are extreme. Notably, the highest metallicity ever measured in a star-forming molecular cloud was around 5 $Z_{\odot}$ (Maiolino & Mannucci, 2019). Although the values for xA Quasars are extreme, they are in line with estimates for high-redshift Quasars in previous studies (Nagao et al., 2006; Shin et al., 2013; Xu et al., 2018). However, these prior studies report lower metallicity and lower line intensities of AlIII, aligning with the expectation of lower metallicity compared to our sample.

It is crucial to emphasize, however, that the accretion disks of AGNs do not resemble typical molecular clouds or normal interstellar environments. The passage of stars in the vicinity of the disk generates Accretion Modified Stars (AMS), objects that accrete material from the disk of the SMBH at high rates. Thanks to this rapid accretion they eventually reach high masses and explode as core collapse supernovae (Cheng & Wang, 1999; Collin & Zahn, 1999; Wang et al., 2023b). This process could give rise to a cascade of supernovae from the compact remnants of these events that would continue accreting material from the accretion disk (Lin, 1997). Stars that reach masses as high as $M \gtrsim 100\ M_{\odot}$ undergo core collapse and enrich the disk with heavy elements through the high metal content of their supernova ejecta (Cantiello et al., 2021). The metallicity produced from such a mechanism would possibly reach the most extreme predicted values of approximately 50 $Z_{\odot}$.

While it may seem impossible to measure metallicities of stars in galaxies greater than 2 $Z_{\odot}$, the results obtained in this thesis are specific to the metallicity of the BLR of Quasars, not their host galaxies. Moreover, the measurements of different metallicities for BC and BLUE in PHL 1092 suggests that selective enrichment of different components is theoretically possible. Radiation-driven winds, accelerated via resonant scattering of metal lines (Proga et al., 2000; Giustini & Proga, 2019), and interactions of compact objects crossing the disk and the disk itself (Wang et al., 2011) are likely mechanisms for this enrichment. Star formation associated to a similar mechanism can give rise to metallicity gradients in BLRs, with the innermost regions being the most metallic, where radiation-driven winds are expected to develop.

Certainly, the connection between metallicity and infrared excess (due to the heating of dust) in the photometry of extreme-accreting objects is a logical and well-supported proposition. The elevated metallicity observed in these objects is a consequence of intense star formation and evolution occurring in proximity to or within the accretion disk. As a result, extreme-accreting objects often exhibit strong episodes of star formation, and this is manifested in the form of infrared excess in their spectra.

Studies, such as those by Caccianiga et al. (2015) and Wang et al. (2023b), have provided evidence supporting this correlation. Therefore, the concurrent detection of metals and an infrared excess in the spectra of these objects not only substantiates their extreme-accreting nature but also offers insights into the intricate interplay between accretion processes, star formation, and metal enrichment in the vicinity of the accretion disk.

4.3 Implications for feedback and galaxy evolution

Figure 4.1 offers a comprehensive visualization of the 3D parameter space, highlighting the logarithms of U, n_{H}, and Z for the two most extreme objects in the sample: TXS 0042+101 representing Population B, and PHL 1092 representing extreme Population A objects. This representation provides a broader perspective on the relationship between Z and variations in U and n_{H}.

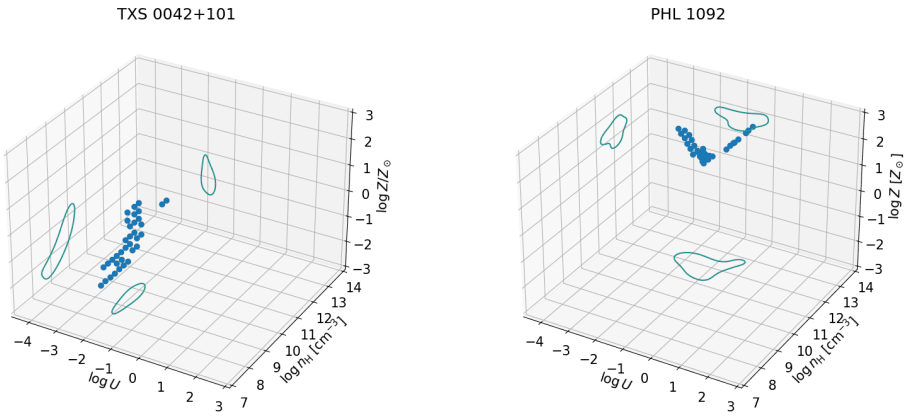

Figure 4.1: 3D plots describing the parameter space of $\log U$, $\log n_{\mathrm{H}}$ and $\log Z$. Each point in the 3D space corresponds to parameters derived from simulations within the 1σ accuracy range relative to the minimum χ^2 between measurements and photoionization simulations. Contours in each plane outline the associated 2D parameter ranges with 1σ accuracy. *Left*: 3D parameter space associated to the extreme Population B object TXS 0042+101. *Right*: 3D parameter space associated to the xA object PHL 1092.

The sketch in Figure 4.2 outlines a global evolutionary scenario for AGNs along the Quasar MS. On the right of the MS we encounter low-mass, high Eddington-ratio sources. These objects accrete at a high rate, possibly as a result of mergers or star formation, leading to the manifestation of an infrared excess. In the initial phases of AGN development, events like mergers and strong interactions result in the accumulation of gas in the central regions of the galaxy, triggering a burst of star formation (Sanders et al., 1988). Mass loss from stellar winds and supernovae subsequently provides accretion fuel for the SMBH. Radiation force and mechanical energy then clear away the dust surrounding the black hole, releasing radiative and mechanical energy into the Interstellar Medium (ISM) of the host galaxy (Fabian, 2012).

At high accretion rates, a nuclear starburst can occur in the region where the disk becomes self-gravitating (Collin & Zahn, 1999). The exceptionally high metallicity values calculated for the BLR in these objects, as discussed in Section 4.2, may be attributed to the formation of AMS. After accreting sufficient mass, these stars explode as core-collapse supernovae, chemically enriching the material in the disk.

At the other end of the MS we find very massive SMBHs, radiating at low Eddington ratios, and approaching conditions of "starvation", indicating the depletion of their ac-

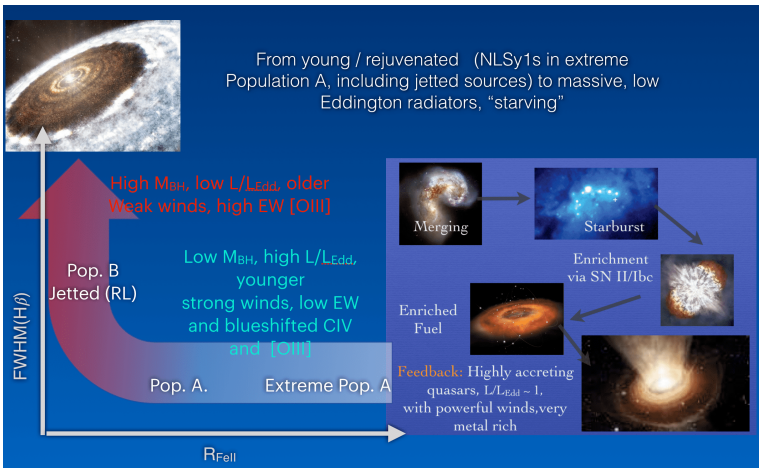

Figure 4.2: Sketch depicting the evolutionary interpretation of the Quasar MS. The inset on the right shows a possible evolutionary path leading to highly accreting quasar showing evidence of high metal enrichment in the BLR. Figure taken from Marziani P., Floris A. et al., 2023 (submitted).

creting gas reservoir. In these RL objects, accretion material comes from evolved star winds that are able to sustain modeled accretion rates (Padovani & Matteucci, 1993).

At this point, if we accept an evolutionary interpretation of the MS, with Population B AGNs being old and metal poor and xA Quasars being young and very metallic, two questions arise:

- Can more metallic gas become less metallic over time?
- If the answer to the previous question is yes, then how?

The answer to these questions was discussed in Fraix-Burnet et al. (2017), and indeed the results obtained in the mentioned article imply that we are looking at two different stages of the same phenomenon. Population A Quasars are likely a brief phase in the evolution of an AGN, typically following intense starbursts or mergers. These events that chemically enrich the gas in circumnuclear regions typically last a few million years, and extreme metallicities can be produced even by few objects in the adjacent regions. Then, for a few million years, the metallicity decreases as it is processed by stars in the circumnuclear regions. A cascade process enriches the surrounding regions, until the presence of metals becomes negligible, being diluted throughout the galaxy and the intergalactic medium. After this process ends, what remains is an AGN with a metal-poor BLR, resembling a Population B Quasar.

To sum up, the results of this work and recent developments (Marziani et al., 2022) suggest different evolutionary paths and environments for Population A and Population B Quasars. Indeed, estimations of metallicity for Population B Quasars point towards solar or sub-solar metallicities. At the other extreme, extreme Population A Quasars appear to be in highly star forming hosts, very metal rich, and likely chemically enriched by circumnuclear starbursts or nuclear AMS (D'Onofrio & Marziani, 2018; Wang et al., 2023b).

Chapter 5

Conclusions and future work

In this chapter the conclusions of this thesis work are reported. In Section 5.1 the conclusions from this work are drawn. In Section 5.2 further improvements that can be brought to the employed techniques are explored, and future projects are described.

5.1 Conclusions

In this thesis, we investigated a sample of 14 Quasars along the Quasar MS. Employing a multi-component fitting technique, we analyzed the UV and optical spectra of these Quasars. The analysis was aided by the use of diagnostic ratios, along with appropriate `CLOUDY` photoionization simulations.

A significant achievement was the determination of a discernible trend in metallicity along the Quasar MS. This finding underscores the intrinsic differences among various Quasar populations, as revealed by their distinct spectral features. Moreover, the visual representation of the sample in Figure 3.15 supports the distinct nature of the objects, highlighting the extreme values of metallicity reached for several objects.

The exploration of this trend supports systematic differences in metallicity between the following populations of Quasars:

- **Extreme Population A**: younger and more metal rich objects, with metallicity up to values of $Z \approx 50 Z_{\odot}$.
- **Population A**: intermediate objects, metal rich or with solar metallicity depending on the spectral type.
- **Population B**: older objects, with large SMBHs and starved of gas, exhibiting sub-solar metallicties of the order of $0.5 Z_{\odot}$ or lower.

Several correlations have been found in the sample, with the logarithm of the metallicity correlating strongly with the parameter R_{FeII} and the logarithm of the Eddington ratio. It is not trivial that we found a robust correlation between these parameters. They provide additional support to the interpretation of the Quasar MS as driven by the Eddington ratio.

Further correlations, as detailed in Section 3.4, underscore the strict connection that lies between accretion parameters and the Quasar MS. The metallicity correlations emphasize the necessity to disentangle the properties of the BLR of Quasars, the possibility of star formation in their proximity, and the impact of feedback on the ISM.

5.2 Future work

In future studies, refining the methodologies employed in this work can lead to more accurate and robust results by revisiting certain approximations. Several aspects warrant attention:

- **Relaxing the Approximation of the Single Cloud Model.** The "single cloud model" used in `CLOUDY` simulations simplifies the treatment of phenomena in the turbulent environment surrounding a SMBH. In reality, clumps of gas and dust may be more prevalent. Future improvements can involve moving away from the single cloud approximation to better capture the complexities of the surrounding environment.
- **VBC and BC distinction in Population B Quasars.** The distinction between VBC and BC in Population B Quasars is a simplification used in the multi-component fitting procedure, as we mentioned in Section 1.3.4. However, these distinctions may not exist, and the observed components might be manifestations of ionization stratification, that is instead gradual. Future work could involve refining the multi-component fitting technique and reconsidering the interpretation of physical conditions in the BC for Population B objects.
- **FeII emission.** The FeII emission might originate from the VBC and the BLUE. Determining an upper limit for FeII emission from these components and enhancing existing FeII templates can contribute to a more robust interpretation, providing additional diagnostic ratios for each of these components and more precise constraints on physical parameters.
- **Effects of Supernovae on specific chemical abundances.** The Z values obtained for extreme accretors may be artificially inflated due to diagnostic ratios connected to AlIII, which could be influenced by supernova events. Even though these values are likely to remain extreme, it is fundamental to verify to what extent the presence of diagnostic ratios dependent on Aluminium abundance changes our results.
- **Chemical abundance scaling.** The AGN environment differs significantly from that around a disk star like the Sun (Cantiello et al., 2021). Using metallicity values scaled on solar chemical abundances may introduce biases. Future analyses should consider more specific chemical abundances to address this issue.
- **Application to larger samples.** Expanding the application of this methodology to larger samples of Quasars in future studies can enhance the conclusiveness and precision of results. Applying the technique to high-redshift Quasars could simplify the analysis process by eliminating the need for space-based observations, as was the case with the current sample.

Bibliography

Antonucci, R. 1993, ARA&A, 31, 473

Bañados, E., Venemans, B. P., Decarli, R., et al. 2016, ApJS, 227, 11

Baker, J. C., Hunstead, R. W., Kapahi, V. K., & Subrahmanya, C. R. 1994, in Astronomical Society of the Pacific Conference Series, Vol. 54, The Physics of Active Galaxies, ed. G. V. Bicknell, M. A. Dopita, & P. J. Quinn, 195

Baldi, R. D., Laor, A., Behar, E., et al. 2022, MNRAS, 510, 1043

Baldwin, J., Ferland, G., Korista, K., & Verner, D. 1995, ApJ, 455, L119

Beckmann, V. & Shrader, C. 2012, in Proceedings of "An INTEGRAL view of the high-energy sky (the first 10 years)" - 9th INTEGRAL Workshop and celebration of the 10th anniversary of the launch (INTEGRAL 2012). 15-19 October 2012. Bibliotheque Nationale de France, 69

Bennett, A. S. 1962, MmRAS, 68, 163

Bentz, M. C., Peterson, B. M., Netzer, H., Pogge, R. W., & Vestergaard, M. 2009, ApJ, 697, 160

Boroson, T. A. & Green, R. F. 1992, ApJS, 80, 109

Bruhweiler, F. & Verner, E. 2008, ApJ, 675, 83

Caccianiga, A., Antón, S., Ballo, L., et al. 2015, MNRAS, 451, 1795

Cantiello, M., Jermyn, A. S., & Lin, D. N. C. 2021, ApJ, 910, 94

Capetti, A., Laor, A., Baldi, R. D., Robinson, A., & Marconi, A. 2021, MNRAS, 502, 5086

Cardelli, J. A., Clayton, G. C., & Mathis, J. S. 1989, ApJ, 345, 245

Cheng, K. S. & Wang, J.-M. 1999, ApJ, 521, 502

Collin, S. & Zahn, J.-P. 1999, Ap&SS, 265, 501

Czerny, B. & Elvis, M. 1987, ApJ, 321, 305

Czerny, B., Li, Y.-R., Hryniewicz, K., et al. 2017, ApJ, 846, 154

D'Agostini, G. 2003, Bayesian Reasoning in Data Analysis: A Critical Introduction (Singapore: World Scientific)

Diamond-Stanic, A. M., Fan, X., Brandt, W. N., et al. 2009, ApJ, 699, 782

D'Onofrio, M. & Marziani, P. 2018, Frontiers in Astronomy and Space Sciences, 5, 31

D'Onofrio, M., Marziani, P., & Chiosi, C. 2021, Frontiers in Astronomy and Space Sciences, 8, 157

Drake, A. J., Djorgovski, S. G., Graham, M. J., et al. 2022, VizieR Online Data Catalog, J/MNRAS/482/98

Du, P., Lu, K.-X., Hu, C., et al. 2016, ApJ, 820, 27

Edge, D. O., Shakeshaft, J. R., McAdam, W. B., Baldwin, J. E., & Archer, S. 1959, MmRAS, 68, 37

Event Horizon Telescope Collaboration, Akiyama, K., Alberdi, A., et al. 2022, ApJ, 930, L14

Event Horizon Telescope Collaboration, Akiyama, K., Alberdi, A., et al. 2019, ApJ, 875, L4

Fabian, A. C. 2012, ARA&A, 50, 455

Fanaroff, B. L. & Riley, J. M. 1974, MNRAS, 167, 31P

Feigelson, E. D. & Babu, G. J. 1992, ApJ, 397, 55

Ferland, G. J., Chatzikos, M., Guzmán, F., et al. 2017, Rev. Mexicana Astron. Astrofis., 53, 385

Ferland, G. J., Done, C., Jin, C., Landt, H., & Ward, M. J. 2020, MNRAS, 494, 5917

Fraix-Burnet, D., Marziani, P., D'Onofrio, M., & Dultzin, D. 2017, Frontiers in Astronomy and Space Sciences, 4, 1

Garnica, K., Negrete, C. A., Marziani, P., et al. 2022, A&A, 667, A105

Gaur, H., Gu, M., Ramya, S., & Guo, H. 2019, A&A, 631, A46

Giustini, M. & Proga, D. 2019, A&A, 630, A94

GRAVITY Collaboration, Dexter, J., Shangguan, J., et al. 2020, A&A, 635, A92

Hamann, F. & Ferland, G. 1999, ARA&A, 37, 487

Hamann, F., Korista, K. T., Ferland, G. J., Warner, C., & Baldwin, J. 2002, ApJ, 564, 592

Harrison, C. 2014, PhD thesis, Durham University, UK

Huang, J., Lin, D. N. C., & Shields, G. 2023, MNRAS, 525, 5702

Jackson, N. & Browne, I. W. A. 1991, MNRAS, 250, 414

Järvelä, E., Dahale, R., Crepaldi, L., et al. 2022, A&A, 658, A12

Kellermann, K. I., Sramek, R., Schmidt, M., Shaffer, D. B., & Green, R. 1989, AJ, 98, 1195

Kellermann, K. I., Sramek, R. A., Schmidt, M., Green, R. F., & Shaffer, D. B. 1994, AJ, 108, 1163

Kembhavi, A. K. & Narlikar, J. V. 1999, Quasars and active galactic nuclei : an introduction (Cambridge University Press)

Keyes, C. D. & et al. 1995, Faint Object Spectrograph Instrument Handbook v. 6.0 (Space Telescope Science Institute)

Kollatschny, W. & Zetzl, M. 2013, A&A, 549, A100

Korista, K., Ferland, G., & Baldwin, J. 1997, ApJ, 487, 555

Kormendy, J. & Richstone, D. 1995, ARA&A, 33, 581

Kriss, G. 1994, in Astronomical Society of the Pacific Conference Series, Vol. 61, Astronomical Data Analysis Software and Systems III, ed. D. R. Crabtree, R. J. Hanisch, & J. Barnes, 437

Kuehn, C. A., Baldwin, J. A., Peterson, B. M., & Korista, K. T. 2008, ApJ, 673, 69

Laor, A. 2004, in Astronomical Society of the Pacific Conference Series, Vol. 311, AGN Physics with the Sloan Digital Sky Survey, ed. G. T. Richards & P. B. Hall, 169

Lin, D. N. C. 1997, in Astronomical Society of the Pacific Conference Series, Vol. 113, IAU Colloq. 159: Emission Lines in Active Galaxies: New Methods and Techniques, ed. B. M. Peterson, F.-Z. Cheng, & A. S. Wilson, 64

Maiolino, R. & Mannucci, F. 2019, A&A Rev., 27, 3

Marinello, M., Rodríguez-Ardila, A., Garcia-Rissmann, A., Sigut, T. A. A., & Pradhan, A. K. 2016, ApJ, 820, 116

Marinello, M., Rodríguez-Ardila, A., Marziani, P., Sigut, A., & Pradhan, A. 2020, MNRAS, 494, 4187

Martínez-Aldama, M. L., Dultzin, D., Marziani, P., et al. 2015, ApJS, 217, 3

Marziani, P., Bon, E., Bon, N., et al. 2022, Astronomische Nachrichten, 343, e210082

Marziani, P., Calvani, M., & Sulentic, J. W. 1992, ApJ, 393, 658

Marziani, P., del Olmo, A., Perea, J., D'Onofrio, M., & Panda, S. 2020, Atoms, 8, 94

Marziani, P., Dultzin, D., Sulentic, J. W., et al. 2018, Frontiers in Astronomy and Space Sciences, 5, 6

Marziani, P., Panda, S., Deconto Machado, A., & Del Olmo, A. 2023, Galaxies, 11, 52

Marziani, P., Sulentic, J. W., Negrete, C. A., et al. 2010, MNRAS, 409, 1033

Marziani, P., Sulentic, J. W., Stirpe, G. M., Zamfir, S., & Calvani, M. 2009, A&A, 495, 83

Marziani, P., Sulentic, J. W., Zamanov, R., et al. 2003, ApJS, 145, 199

Marziani, P., Sulentic, J. W., Zwitter, T., Dultzin-Hacyan, D., & Calvani, M. 2001, ApJ, 558, 553

Mathews, W. G. & Ferland, G. J. 1987, ApJ, 323, 456

Medallon, S. & Welty, D. 2023, in STIS Instrument Handbook for Cycle 31 v. 22, Vol. 22 (Space Telescope Science Institute), 22

Nagao, T., Maiolino, R., & Marconi, A. 2006, A&A, 459, 85

Negrete, C. A., Dultzin, D., Marziani, P., & Sulentic, J. W. 2012, ApJ, 757, 62

Negrete, C. A., Dultzin, D., Marziani, P., & Sulentic, J. W. 2013, ApJ, 771, 31

Netzer, H. 2013, The Physics and Evolution of Active Galactic Nuclei (Cambridge University Press)

Netzer, H. 2019, MNRAS, 488, 5185

Osterbrock, D. E. 1989, Astrophysics of gaseous nebulae and active galactic nuclei (University Science Books)

Padovani, P. & Matteucci, F. 1993, ApJ, 416, 26

Pagel, B. E. J., Edmunds, M. G., Blackwell, D. E., Chun, M. S., & Smith, G. 1979, MNRAS, 189, 95

Panda, S., Czerny, B., Adhikari, T. P., et al. 2018, ApJ, 866, 115

Panda, S. & Marziani, P. 2023, Frontiers in Astronomy and Space Sciences, 10, 1130103

Panda, S., Marziani, P., & Czerny, B. 2019, ApJ, 882, 79

Peterson, B. M. 1993, PASP, 105, 247

Peterson, B. M. & Wandel, A. 1999, in American Astronomical Society Meeting Abstracts, Vol. 194, American Astronomical Society Meeting Abstracts #194, 49.12

Peterson, B. M. & Wandel, A. 2000, ApJ, 540, L13

Petrucci, P. O., Gronkiewicz, D., Rozanska, A., et al. 2020, A&A, 634, A85

Plotkin, R. M., Shemmer, O., Trakhtenbrot, B., et al. 2015, ApJ, 805, 123

Press, W. H., Flannery, B. P., & Teukolsky, S. A. 1986, Numerical recipes. The art of scientific computing (Cambridge University Press)

Proga, D., Stone, J. M., & Kallman, T. R. 2000, ApJ, 543, 686

Punsly, B., Marziani, P., Bennert, V. N., Nagai, H., & Gurwell, M. A. 2018, ApJ, 869, 143

Rees, M. J. 1984, ARA&A, 22, 471

Sadowski, A., Narayan, R., McKinney, J. C., & Tchekhovskoy, A. 2014, MNRAS, 439, 503

Salpeter, E. E. 1964, ApJ, 140, 796

Sanders, D. B., Soifer, B. T., Elias, J. H., et al. 1988, ApJ, 325, 74

Sarkar, A., Ferland, G. J., Chatzikos, M., et al. 2021, ApJ, 907, 12

Schmidt, M. 1963, Nature, 197, 1040

Seyfert, C. K. 1943, ApJ, 97, 28

Shen, Y. & Ho, L. C. 2014, Nature, 513, 210

Shen, Y. & Liu, X. 2012, ApJ, 753, 125

Shin, J., Woo, J.-H., Nagao, T., & Kim, S. C. 2013, ApJ, 763, 58

Sigut, T. A. A. & Pradhan, A. K. 2003, ApJS, 145, 15

Śniegowska, M., Marziani, P., Czerny, B., et al. 2021, ApJ, 910, 115

Soderblom, D. R. 2023, in COS Instrument Handbook v. 15.0, Vol. 15 (Space Telescope Science Institute), 15

Sulentic, J. W., Marziani, P., Zwitter, T., Dultzin-Hacyan, D., & Calvani, M. 2000, ApJL, 545, L15

Tang, B., Shang, Z., Gu, Q., Brotherton, M. S., & Runnoe, J. C. 2012, ApJS, 201, 38

Tody, D. 1993, in Astronomical Society of the Pacific Conference Series, Vol. 52, Astronomical Data Analysis Software and Systems II, ed. R. J. Hanisch, R. J. V. Brissenden, & J. Barnes, 173

Urry, C. M. & Padovani, P. 1996, in Extragalactic Radio Sources, ed. R. D. Ekers, C. Fanti, & L. Padrielli, Vol. 175, 379

Vanden Berk, D. E., Richards, G. T., Bauer, A., et al. 2001, AJ, 122, 549

Vestergaard, M. & Peterson, B. M. 2006, ApJ, 641, 689

Vestergaard, M. & Wilkes, B. J. 2001, ApJS, 134, 1

Vietri, G., Piconcelli, E., Fiore, F., et al. 2016, in Active Galactic Nuclei 12: A Multi-Messenger Perspective (AGN12), 22

Wang, A., An, T., Cheng, X., et al. 2023a, MNRAS, 518, 39

Wang, J.-M., Du, P., Songsheng, Y.-Y., & Li, Y.-R. 2022, A&A, 666, A86

Wang, J.-M., Ge, J.-Q., Hu, C., et al. 2011, ApJ, 739, 3

Wang, J.-M., Zhai, S., Li, Y.-R., et al. 2023b, ApJ, 954, 84

Xu, F., Bian, F., Shen, Y., et al. 2018, MNRAS, 480, 345

Zamfir, S., Sulentic, J. W., & Marziani, P. 2008, MNRAS, 387, 856

Zamfir, S., Sulentic, J. W., Marziani, P., & Dultzin, D. 2010, MNRAS, 403, 1759

Zdziarski, A. A., Ghisellini, G., George, I. M., et al. 1990, ApJ, 363, L1